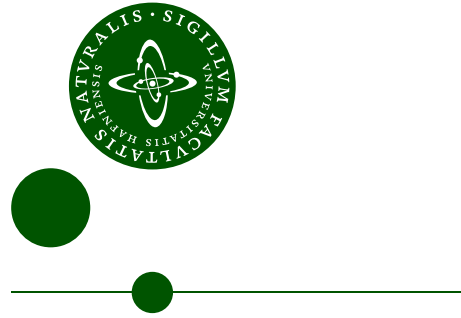NIELS BOHR INSTITUTET
KØBENHAVNS UNIVERSITET

Positive ions, collective modes and Anderson localization in ultracold gases

Pietro Alberto Massignan
Ph.D. thesis

Academic supervisors: Prof. Henrik Smith
Prof. Christopher J. Pethick

January 2006

Preface

The experiments on ultracold gases provided in the last decade striking confirmations of the quantum nature of matter. As examples, we may mention the direct imaging of interference of matter waves, of quantized vortices or of the different effects of bosonic and fermionic statistics. Continuous technical improvements unveiled unexpected possibilities, and at present parameters such as dimensionality, interaction strength and temperature can be tuned in the experiments with incredible flexibility. Moreover, the modeling of ultracold gases is particularly simple since, due to the extremely low densities involved, interactions can generally be satisfactorily described in terms of two-body collisions. Experiments on ultracold gases are contributing to a deeper understanding of collision processes in atomic physics and of fascinating and complex theories such as the BEC-BCS crossover. In addition, ultracold gases appear by now as promising simulators for many puzzling quantum problems.

This thesis collects my research done under the supervision of Profs. Henrik Smith and Christopher J. Pethick on a set of topics in the theory of ultracold gases. In the first chapter, I present an introduction to ultracold gases followed by a detailed description of the problems addressed in the course of my studies. The second chapter reviews the theory of two-body collisions, presenting both its elementary and its more advanced features. In the following three chapters I report the results of my work.

The third and fourth chapters contain material that have been published as:

- P. Massignan, C. J. Pethick, and H. Smith, "Static properties of positive ions in atomic Bose-Einstein condensates", Phys. Rev. A **71**, 023606 (2005).

- P. Massignan, G. M. Bruun, and H. Smith, "Viscous relaxation and collective oscillations in a trapped Fermi gas near the unitarity limit", Phys. Rev. A **71**, 033607 (2005).

The fifth chapter covers the results obtained in collaboration with Dr. Yvan Castin (LKB-ENS, Paris). This material will be submitted for publication as:

- P. Massignan and Y. Castin, "3D Anderson localization of matter waves by scattering off atoms in a lattice with a confinement-induced resonance".

Acknowledgments

I am sincerely grateful to my supervisors Henrik Smith and Chris Pethick for all what I have learned from them in these years: their continuous curiosity for science, their experience and pedagogical skills, and their exceptional kindness deeply impressed me and constantly inspired me during these intense years. The friendly and elegant atmosphere that one breathes entering their offices or their group meetings is clear evidence for their wonderful ability to make everybody feel at ease.

My gratitude also goes to all the other members of the *BEC and cold atomic gases group* at NORDITA and NBI. A special acknowledgement to Georg Bruun, for his brilliant scientific skills, his determination, his tolerance towards my endless questions and the sincere attitude of his answers.

I thank the Niels Bohr Institutet, the NORDITA and the Københavns Universitet for having made possible this experience, important for my education on both the scientific and the human sides.

Part of the work presented in this thesis has been worked out during my stay in the *groupe atomes froids* at Laboratoire Kastler-Brossel (École Normale Supérieure de Paris), whom I thank for the hospitality. I am particularly grateful to Yvan Castin for his kind willingness to host me, and for the patience demonstrated in the many physics lectures he has given me.

I am profoundly indebted to my family that keeps supporting me and my ambitions, and to all my friends and to Janna that keep sharing with me my daily worries, my discontinuous moods and my euphoric moments.

Copenhagen, January 2006

Pietro Massignan

Contents

Chapter 1

Introduction

One of the most active areas of contemporary physics is the study of atomic gases under conditions when quantum effects become important. As the particles get so cold and dense that the associated thermal de Broglie wavelength becomes comparable to the interparticle separation, a classical description breaks down and quantum mechanics predicts that the two separate classes of atoms, namely bosons and fermions, behave in strikingly different ways. The progress made by cooling techniques in the last 20 years opened enormous experimental possibilities to explore the quantum regime, and a major breakthrough was announced in the summer of 1995 when almost simultaneously three groups at JILA, MIT and Rice University reported Bose-Einstein condensation in a gas of bosonic alkali atoms (respectively, ^{87}Rb [1], ^{23}Na [2] and ^{7}Li [3]). Since then, an amazing wealth of beautiful experiments and theoretical papers have appeared, and the field has never stopped growing[1]. A concise introduction to the research on ultracold gases is given in the following few pages. The reader interested in a more historical, complete description and in an exhaustive list of references can refer to two recent monographs dedicated to this subject [4, 5].

A first generation of experiments investigated static and dynamic properties of bosonic gases. Among the former, we might include the effects of interactions on the critical temperature for condensation and on the shape of a trapped cloud. Among the latter, intensive studies have been performed to show the formation of beautiful interference fringes, to characterize collective modes of oscillation, to study the cloud expansion and the propagation of sound waves, to investigate non-linear phenomena such as soliton propagation and matter-wave amplification. Many groups successfully imparted a controlled amount of angular momentum to the clouds, and large triangular arrays of quantized vortices were imaged and studied in depth.

In current experiments, laser cooling techniques make it possible to refrigerate the atomic gases to strikingly low temperatures, but these are still insufficient to enter the quantum degenerate regime. A second stage, which allows to reach the critical temperature at about $\sim 0.1\mu$K, always consists of a sort of evaporation, during which the most energetic atoms are allowed to leave the trap and the remaining particles thermalize at a lower temperature through elastic two-body collisions. This cooling procedure however does not work efficiently

---

[1]Up to now, quantum degeneracy has been observed in dilute atomic and/or molecular gases of H, He*, Li, Na, K, Cr, Rb, Cs and Yb.

for identical fermions, since low-energy scattering is forbidden by the antisymmetrization principle (see Chap. 2, where the theory of low-energy two-body scattering is analyzed in detail), and a more complex path had to be developed. Degenerate fermions have nonetheless been obtained, about five years later than their bosonic counterparts, employing either two different hyperfine states of the same fermionic element, which are simultaneously evaporated, or sympathetic cooling of fermions by collisions with an evaporatively cooled gas of bosons. Early results from this new generation of experiments on fermions showed the effects of the different quantum statistics governing particles with either integer or half-integer spin. While in the degenerate regime bosons tend to gather or "condense" in the lowest energy state available (the ground state of the trap), fermions occupy all possible momentum states in the Fermi sphere up to the Fermi energy ϵ_F, irrespective of the geometry of the trap. This is seen very clearly upon free expansion of the gas from cigar- or pancake-shaped harmonic traps: fermionic clouds expand isotropically, while bosons maintain "memory" of the geometry of the trap in their density profile during expansion.

Atomic gases have the uncommon property of being extremely flexible systems, since interactions, dimensionality and thermodynamic variables such as density and temperature can be tuned almost at will. Quite remarkably, theory and experiments progress at the same pace, constantly challenging each other, and beautiful results have been obtained (see Fig. 1.1).

Some of the most common **THEORETICAL CONCEPTS** employed in this field are presented here below.

- *Two-body, low energy scattering theory* deserves a special mention. Indeed, when dealing with quantum degenerate gases, the densities involved are much smaller than the ones encountered in solid state physics. Typical values coming here into play are $n \approx 10^{13}$–10^{15}particles/cm^3, 8 orders of magnitude smaller than the corresponding figure for electrons in a metal, liquid helium or common solids. Such small densities are necessary to avoid inelastic three-body scattering events, that would lead to losses and molecule formation. Neutral alkaline atoms interact with (induced dipole-dipole) van der Waals forces, for which the characteristic quantum-mechanical length scale is typically $R \approx 0.1$–10nm. In the experiments of interest here, the gases are therefore very dilute in the sense that the interparticle distance $n^{-1/3}$ is much larger than the characteristic length of the force between the atoms,

$$nR^3 \ll 1. \tag{1.1}$$

Collisions involving more than two particles are then extremely rare and *two-body* scattering theory provides an excellent description of the microscopic dynamics. When the density is so low, one expects that the transition to the quantum regime will happen at incredibly low temperatures: equating the thermal de Broglie wavelength

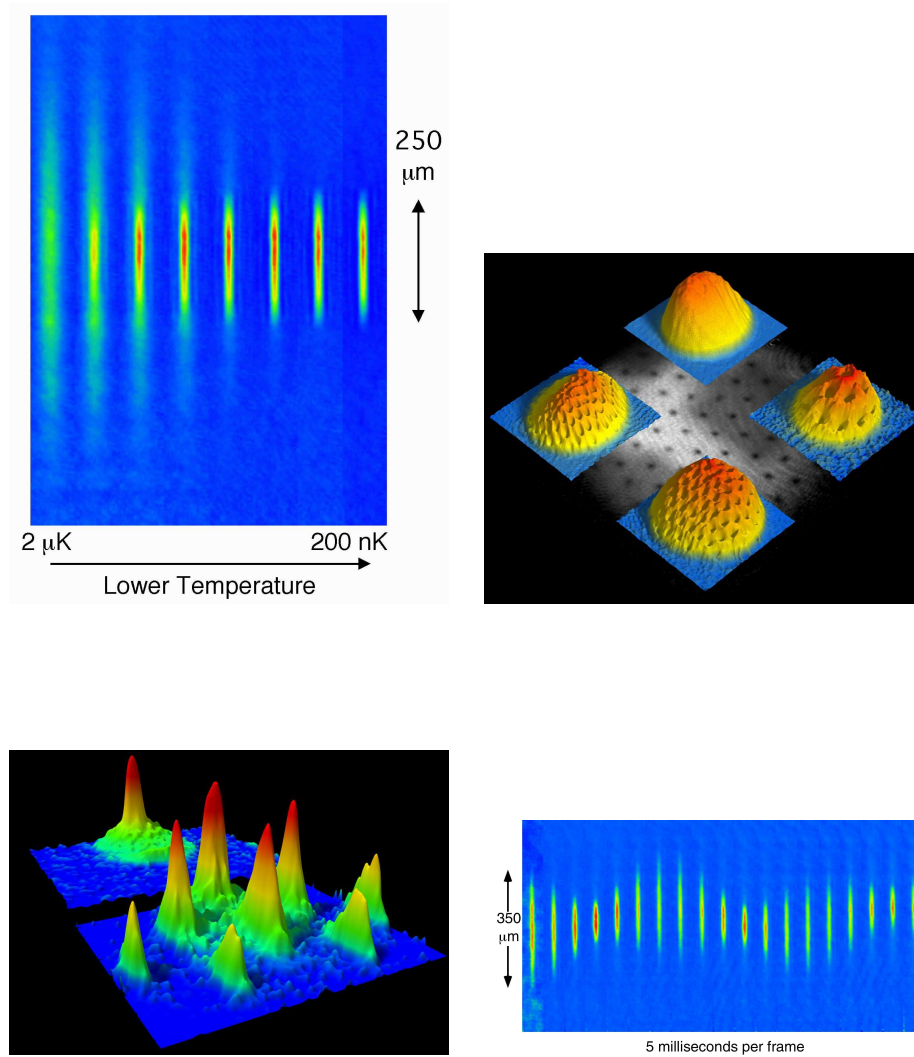$$\lambda_T = \sqrt{\frac{2\pi\hbar^2}{mkT}} \tag{1.2}$$

Figure 1.1: Gallery of ultracold memorabilia: (from left to right and top to bottom) the birth of a condensate, array of vortices, formation of superradiant peaks and a cloud performing quadrupole oscillations. Images from the website of Wolfgang Ketterle's group at MIT (http://cua.mit.edu/ketterle_group).

to the interparticle distance $n^{-1/3}$, one indeed finds $T_C \approx 10^{-7}\text{--}10^{-6}\text{K}$ (for a comparison, the critical temperature for the superfluid transition in liquid helium is $T_C = 2.2\text{K}$, and the Fermi temperature for electrons in a solid is $T_F \approx 10^4\text{--}10^5\text{K}$). To reach degeneracy, the atoms in the gas are then cooled from room temperature, where particles move at velocities of a few hundred meters per second (the speed of an airplane), all the way down below T_C where they have typical velocities of order centimeters per second. As we will see in detail in Chap. 2, at such *low-energies* collisions can be appropriately modelled by a contact potential, isotropic in space and whose strength is governed by a single observable, the *s*-wave scattering length a, that can be accurately determined from a variety of independent experiments.

- Static and dynamic properties of dilute gases of bosons at $T \ll T_C$ can be successfully extracted from a relatively simple differential equation, that has the form of a Schrödinger equation with a non-linear mean field term:

$$i\hbar\frac{\partial\psi}{\partial t} = \left[-\frac{\hbar^2\nabla^2}{2m} + V(\mathbf{r},t) + U_0\left|\psi\right|^2\right]\psi. \qquad (1.3)$$

This is known as the *Gross-Pitaevskii (GP) equation* and describes the dynamics of a complex order parameter $\psi(\mathbf{r},t)$ whose modulus squared is interpreted as the density of condensed particles, $n(\mathbf{r},t) = \left|\psi(\mathbf{r},t)\right|^2$, all occupying the same quantum state. The strength of the mean field interaction is parameterized by the constant U_0, that contains all the informations about low-energy scattering, while $V(\mathbf{r},t)$ takes into account the external potential.

- Writing the order parameter as $\psi = \sqrt{n}\exp(i\phi)$, the GP equation can be separated into real and imaginary part to obtain the equations of *quantum hydrodynamics,* that have been applied in investigating sound waves and collective modes of oscillation of condensed clouds, as well as the static properties of trapped condensates.

- *Kinetic theory* has been intensively used to describe non-condensed systems (bosonic gases above or close to the critical temperature, or fermions in their normal state) in a vast collection of problems, including studies of cooling processes, relaxation of temperature anisotropies, and characterization of collective modes.

- Many of the model potentials "dreamed" of by theorists such as double wells and periodic lattices can nowadays be realized experimentally (see below). When the potential is sufficiently deep to ensure weak site-to-site coupling (tight-binding regime), *discrete models* prove to be very useful in capturing the main physical features of these realizations.

- Recent technical developments allowed to enter the regime of strong interactions, where the diluteness condition (1.1) is violated: in this case, *quantum many-body theory* is the natural framework to employ, and systematic diagrammatic expansions can be performed to study e.g. shifts of critical temperature and mean field energies, or superfluidity effects in fermionic clouds. Powerful *numerical methods* such as Monte Carlo calculations are also often employed in this regime.

Atoms are strongly influenced by both electric and magnetic fields, and during these years of rapid evolution a combination of clever ideas and careful tailoring has made it possible to develop an amazing EXPERIMENTAL TOOL-BOX for flexible manipulation of ultracold gases. Here below a list of some of these tools is given.

- The energy of an atom in a magnetic field depends to a good approximation linearly on the external field, and inhomogeneous fields are widely used to realize *magnetic traps* for cold clouds. Only configurations with local minima can exist in the absence of electric currents, and therefore only states with negative magnetic moment (so-called low-field seekers, since $\Delta E = -\mu B$) may be trapped magnetically. Many configurations have been explored, and by now very smooth harmonic traps can be realized with large control over the depth of the potential and the relative strength of the confinement in the three orthogonal spatial directions.

- A laser whose frequency is slightly detuned with respect to an atomic transition constitutes a strong potential for the atoms. In particular, particles are attracted towards regions of intense red-detuned light and repelled from blue-detuned ones. Based on this principle, tightly focused red-detuned lasers are currently used as *optical traps* which are insensitive to the magnetic state of the cloud, and in particular can trap together many different hyperfine states of the same atom. Similarly, blue-detuned sheets of laser light have been employed as "knives" to neatly split a cloud into two spatially separated components which interfere upon release from the trap, as well as to create localized disturbances and study the propagation of sound waves in the cloud.

- The optical and magnetic traps used to confine the atoms can be deformed all the way from isotropic to elongated in either one or two spatial dimensions, giving respectively spherical, cigar- or pancake-shaped clouds. When the anisotropy is so extreme that both the chemical potential μ and the thermal energy kT are smaller than the spacing between the discrete levels of the transverse (axial) confining potential, the atoms are confined to the ground state of the trap in the radial (axial) direction and the dynamics of the system is effectively reduced to one dimension (two dimensions). *Reduced dimensionalities* have attracted a lot of interest recently, and many experimental and theoretical efforts concentrate on the realization and characterization of strong interactions in one dimension, the so called Tonks-Girardeau regime, and of the Kosterlitz-Thouless transition describing the formation of vortex-antivortex pairs in two dimensions.

- Standing waves obtained by retroreflected laser beams generate potentials, often referred to as *optical lattices*, which are constant in time, sinusoidally modulated in space, and exempt of any defect. One-, two- and three-dimensional configurations can be realized, allowing one to split a cold cloud into ordered arrays of hundreds of identical pancakes, tubes, or point-like smaller clouds. The strength of the periodic potential is proportional to the intensity of the laser, and as the latter is gradually increased one can explore the interesting crossover regime between a conductor and

an insulator, i.e. the transition between coherent well-to-well tunneling
and isolated, incoherent wave functions localized at each lattice site.

- The effective interactions between the atoms can be accurately tuned with
  the aid of an external (magnetic or electric) field. This technique takes
  advantage of so-called *Fano-Feshbach resonances*, that occur whenever a
  bound molecular level is shifted by the external field to resonance with the
  total energy of two scattering particles. Sweeping the external field, the ef-
  fective interaction may be tuned to explore regions of attractive, repulsive
  or vanishing interaction. In particular, one can enter the appealing regime
  of strong interactions, that opens up when the magnitude of the scattering
  length becomes larger than the mean distance between particles. Under
  these conditions bosons undergo frequent inelastic three-body collisions
  and are very quickly lost from the trap, but very long lifetimes have been
  measured for mixtures of two hyperfine states of fermionic atoms[2].

In the investigations that constitute the content of the present thesis, a wide
range of the experimental tools and theoretical methods presented above has
been combined to attack a set of open problems in the theory of ultracold gases.

1.1 Problems addressed in the thesis

Motivated by new ideas and unexplained experiments, during the course of my
Ph.D. studies I have had the pleasure of investigating various problems in the
field of ultracold atoms which, as detailed in the previous Section, appears today
extremely rich and rapidly developing.

A basic tool forming a common ground for all these topics is the theory of
two-body, low-energy scattering: it is presented in detail in Chap. 2, covering
the basic zero-energy limit, the derivation of the effective contact interaction,
and the more advanced treatment describing the extensions of the theory needed
when stronger interactions or sizeable energies come into play.

In the following pages, I will introduce the reader to the three main subjects
on which my studies have focused. Each of the topics is then analyzed in detail
in Chaps. 3, 4 and 5, respectively.

Ions in a Bose-Einstein condensed gas

In the helium liquids, the measurement of properties of ions has been a valuable
probe for understanding the behavior of the liquid. Charged particles have been
employed extensively to put in evidence vortex lattices in rotating ^{4}He and to
elucidate scattering processes in ^{3}He. The interaction of a positively charged
ion with the neutral liquid is so strong that helium solidifies around each ion,
forming composite structures known as *snowballs.* Intense studies focused as
well on *electron bubbles*, i.e. the large depletions that appear around single
electrons in the liquid.

The first experiments on ions in an ultracold atomic gas (^{87}Rb) have been
reported by the cold atoms group in Pisa [6], and more experiments are planned

---

[2]The Pauli principle stabilizes two-species fermionic gases against three-body losses, since
a collision between three particles would necessarily bring in a very limited spatial region two
fermions with the same set of quantum numbers.

in the near future [7], but to date there is little theory concerning ions in such gases [8].

The interaction between an atom and an ion at large distances is due to the polarization of the neutral atom by the ion. We are interested in the properties of a positively charged alkali ion immersed in an otherwise uniform Bose-Einstein condensate. The atom-ion interaction is strong, in that it can support many two-body bound states, and the typical energy scale associated with it ($\sim 1\mu\mathrm{K}$) is comparable to the chemical potential under common experimental conditions: a single ion can substantially perturb the density profile of the condensate in its surroundings. To answer the question of how big this effect is, we will first demonstrate by a thermodynamic argument that in the limit of low bulk condensate density the number of atoms associated with each ion is given by the ratio of the atom-ion and atom-atom scattering lengths. This approach indicates that ΔN is of order 10–100, either positive or negative.

For higher gas densities, we extract the asymptotic behavior of the solutions of the Gross-Pitaevskii equation (1.3), and solve it numerically with a potential that closely resembles the ionic one. We will find that, with increasing mean field interaction, pairs of solutions merge and disappear, which leads to discontinuous changes in ΔN. To clarify this point we analyze the simpler problem of an interacting gas in a 3D spherical square well and show that, in the dilute limit, there exist $2\nu_S + 1$ solutions that connect to a constant density at infinity (where ν_S is the number of bound states of the Schrödinger equation for the same potential). As the asymptotic density increases, pairs of solution with the same number of nodes become degenerate and disappear, until at very high density there exists only a node-less solution. In Appendix A we present the analytic solution of a related problem, an interacting gas in a square well potential in one dimension, and show that it behaves qualitatively differently from the ionic potential, in the sense that solutions continue to exist for arbitrary high external density. For the case of the ionic potential, the disappearance of states implies a discontinuous behavior that shows up at bulk densities in the current experimental range and should therefore be observable.

Our results have previously been published in [9] and are here illustrated in Chap. 3.

Viscous relaxation and collective modes of interacting Fermi gases in the normal phase

Trapped ultracold clouds offer the exciting prospect of examining the effects of atomic interactions with unprecedented accuracy and flexibility. Particularly appealing is the study of two-component mixtures of fermions, since those are characterized by very long lifetimes even in the strongly-interacting regime. When the scattering length for the interspecies potential is small and positive so that $(k_F a)^{-1} \gg 1$, there exists a two-body bound state and theory predicts that at $T = 0$ fermions combine together to form a BEC of tightly-bound bosonic molecules. In the opposite limit of small and negative scattering length, $(k_F a)^{-1} \ll -1$, many-body effects provide an attractive potential and a BCS-superfluid of loosely bound pairs should emerge. The interactions between atoms can be varied almost at will, which allows one to study the intriguing problem of a two-component Fermi gas in the BEC-BCS crossover region where $-1 \lesssim (k_F a)^{-1} \lesssim 1$. Many experiments have been reported in all these regimes,

providing clear evidence for a molecular BEC on one side [10], and for conden-
sation of pairs [11] and the existence of a pairing gap [12] on the other side. In
a particularly recent and remarkable experiment [13] a vortex lattice has been
observed all across the resonance region, finally demonstrating the long-debated
superfluidity of the fermionic gas: the authors give also sound evidence that su-
perfluidity in the strongly-interacting regime is very stable against mismatch of
the Fermi surfaces (i.e. imbalance in the population of the two spin components)
and that a transition to the normal state is observed only when the difference
in chemical potentials between the two species becomes larger than the pair-
ing gap. The nature of the system in the cross-over regime has been object of
intense studies in the past decades [14] and is still very actively discussed.

The measurement of both the frequency and the damping of collective modes
provide an important spectroscopic tool probing the many-body dynamics of
atomic gases. As an example we recall that the frequency and the damping of the
oscillations give information on typical relaxation rates in the system, and allow
one to distinguish between collisionless and hydrodynamic regimes. Even though
the collective mode spectra of a normal gas in the hydrodynamic regime and
that of a bulk superfluid gas are identical [15, 16, 17], the damping of the modes
as a function of temperature should make it possible to distinguish between the
two regimes [18]. Recent papers from the experimental groups in Innsbruck
and at Duke University reported measurements on the collective modes of a
two-component Fermi gas (^{6}Li) close to the unitarity limit $(k_\mathrm{F}|a|)^{-1} \ll 1$ with
somewhat surprising and unexpected results [18, 19, 20, 21]. In particular, the
frequency measured for the transverse mode is close to the value predicted by
hydrodynamic theory.

In Chap. 4 we address the problem of characterizing the spectrum of collec-
tive modes of a two-component Fermi gas in its normal phase. Our starting point
is a Boltzmann equation with interaction effects included in both the streaming
terms and the collision integral, through a mean field added to the external
potential and an energy-dependent cross section in the collision integral. We
first find an expression for the viscosity of a classical uniform gas and show how
interactions modify its temperature dependence. The result is used to identify
a viscous relaxation rate that sets the scale of typical collision times in the gas.
We then consider a trapped gas, and extract the frequency and the damping
of the low-energy collective modes as a function of temperature and interaction
strength through a variational solution of the Boltzmann equation. Most of the
technical details of the derivation are given in Appendix B. We finally com-
pare our findings with the measurements reported in [18, 19, 20, 21], pointing
out that classical hydrodynamics cannot be applied to describe the transverse
oscillations measured in the above-mentioned experiments, and identifying the
high and low temperature regions where collisionless behavior is expected. Our
results have previously been published in [22].

3D Anderson localization of matter waves

The recent advances in the manipulation of ultracold gases have made it possi-
ble to employ these to accurately simulate many systems in condensed matter
physics. As examples, we may mention the exploration of the superfluid to
Mott-insulator transition [23] and the already cited BEC-BCS crossover. Disor-
der plays an important role in the theory of solid state, affecting in a substantial

way the transport properties of various systems. Special attention has in the past been dedicated to studies of flow of liquid helium in porous media, light propagation in strongly-scattering powders and electron transport in metals in the presence of impurities [24, 25, 26]. It looks therefore interesting to introduce a controlled disorder in the experiments with ultracold atoms, in order to provide a closer modelling of realistic systems of condensed matter physics.

Particularly appealing is the possibility of studying a non-interacting matter wave exposed to static disorder and looking for the presence of localized eigenstates, that is stationary states with a square integrable wave function at an energy where the classical motion is not bounded spatially. After the important work of Anderson [27], it is indeed expected that disordered potentials can generically lead in 3D to a quantum transition, a macroscopic number of localized states being present at low energy. Such a phase transition in 3D is difficult to observe, as it is sensitive to decoherence and wave absorption effects, and requires a mean free path of the wave smaller that the wavelength. Anderson localization of light has been long sought in semi-conductor powders [28], but no direct evidence was obtained in 3D for matter waves. Ultracold atoms are good candidates in this respect, due to their weak coupling to the environment and to the possibility of tuning their interactions virtually to zero with a Feshbach resonance. An open problem is however to know if strong enough disorder can be introduced in these gases to lead to 3D Anderson localization with reasonably short localization lengths.

A natural way to produce a disordered potential in atomic gases is to use the speckle pattern of a laser beam [29]. Many experiments on Bose-Einstein condensates (BECs) in 1D random optical potentials have very recently been reported [30, 31, 32, 33], and they provide evidence for disorder-related effects such as fragmentation of the condensate, suppression of diffusion, frequency shifts and damping of collective oscillations. Genuine Anderson localization in 1D, in the non-interacting regime, has not been reported yet in these experiments, and the implementation of the disordered optical potential in 3D remains to be done. Also the theoretical analysis of matter wave localization in a speckle pattern in 3D in the strong localization regime has not yet been performed in detail.

An alternative method to realize a disordered potential was proposed in [34]: a matter wave, made of atoms of a species A, scatters off a set of atoms of another species B that are randomly trapped at the sites of a deep optical lattice with a low filling factor (see Fig. 5.2). As we will choose the lattice to be very far detuned for the species A, the matter wave moves unaffected through the optical lattice, and interacts only with the B atoms: this excludes classical localization effects in local potential minima (that is a major drawback in the experiments with speckle potentials). The disorder can be made very strong, since (i) the correlation length of the disorder can be as small as 0.5μm (the spacing of the optical lattice), and (ii) the scattering cross section of the matter wave off a single atom can be made as high as allowed by quantum mechanics (the so-called unitarity limit) by use of a $A-B$ interspecies Feshbach resonance, which make it possible to dramatically reduce the mean free path of the matter wave. Furthermore, as we shall take advantage of, this model allows a straightforward exact numerical analysis even in 3D, when B atoms are modeled as fixed point-like scatterers, as is known for light waves [35, 36].

It is the 3D version of this scheme that we analyze in Chap. 5. After a

detailed presentation of our model and its practical implementation, we show
numerically that it leads to the appearance of a large number of localized states
for a range of parameters accessible in present experiments, provided that the ef-
fective coupling between the matter wave and a single scatterer is large enough.
One of the Sections is dedicated to the quantitative description of the scattering
between the matter wave and a single trapped scatterer, and to the discussion
of the confinement-induced resonances (CIRs) thereby arising: we show indeed
that arbitrarily large effective coupling constants can be obtained. Possible
strategies of observation of the presence of Anderson localization are also dis-
cussed. Details about the calculation of the Green's function of a particle in
a box and about an integral equation appearing in the text are reported in
Appendices C and D. The results presented here will soon be submitted for
publication [37].

Chapter 2

Cold two-body collisions

The purpose of this Chapter is to describe in a quantitative way how two particles deviate, or "scatter", from their original trajectory after a collision. We will consider only *elastic scattering*, i.e. energy-conserving processes that do not alter the internal state of the particles, and we will assume that two distinguishable particles interact through a central potential $U(r)$. The motion of the center-of-mass of the pair is described by a plane wave and can be taken out of the problem by switching to a reference system where the center-of-mass is at rest. The two-body problem is in this way reduced to the scattering of a single particle of mass $\mu = m_1 m_2 / (m_1 + m_2)$ by a stationary potential, and is described thoroughly in standard textbooks [38, 39, 4].

The wave function for the relative coordinate in a state of definite energy $E = \hbar^2 k^2 / 2\mu$ is the sum of an incoming plane wave and an outgoing scattered wave:

$$\psi(\mathbf{r}) = e^{i\mathbf{k}\cdot\mathbf{r}} + \psi_{\mathrm{sc}}(\mathbf{r}). \tag{2.1}$$

The plane wave is normalized so that the current density is equal to the plane wave velocity $\mathbf{v} = \hbar\mathbf{k}/m$. At large distances the outgoing scattered wave becomes spherical, and the wave function assumes the asymptotic form

$$\psi(\mathbf{r}) \simeq e^{i\mathbf{k}\cdot\mathbf{r}} + f_k \frac{e^{ikr}}{r}. \tag{2.2}$$

Due to the spherical symmetry of the potential, the solution has rotational symmetry with respect to the direction of the incident plane wave (which we take to be the z direction) and the scattering amplitude f_k depends only on the angle θ between the incoming and the outgoing relative momenta. The latter property allows to expand the wave function for the relative motion on the basis of Legendre polynomials $P_l(\cos\theta)$,

$$\psi(\mathbf{r}) = \sum_{l=0}^{\infty} A_l P_l(\cos\theta) R_{kl}(r). \tag{2.3}$$

The radial wave functions $R_{kl}(r)$ satisfy the equation

$$\frac{\mathrm{d}^2 R_{kl}(r)}{\mathrm{d}r^2} + \frac{2}{r}\frac{\mathrm{d}R_{kl}(r)}{\mathrm{d}r} + \left[k^2 - \frac{l(l+1)}{r^2} - \frac{2\mu}{\hbar^2}U(r) \right] R_{kl}(r) = 0, \tag{2.4}$$

and at large interparticle separations, where we can neglect both the centrifugal barrier and the potential, they have the asymptotic form

$$R_{kl}(r) \simeq \frac{1}{kr} \sin\left(kr - \frac{\pi}{2}l + \delta_l\right) \tag{2.5}$$

expressed for each angular momentum component in terms of an appropriate phase shift δ_l. The coefficients A_l are fixed by comparing (2.3) with (2.2). Using the asymptotic expansion for a plane wave (valid at large distances)

$$e^{ikz} \simeq \frac{1}{kr} \sum_{l=0}^{\infty} i^l (2l+1) P_l(\cos\theta) \sin\left(kr - \frac{\pi}{2}l\right) \tag{2.6}$$

and imposing that the solution contains only outgoing spherical components, one finds

$$A_l = i^l (2l+1) e^{i\delta_l}$$

and

$$f_k(\theta) = \frac{1}{2ik} \sum_{l=0}^{\infty} (2l+1) \left(e^{2i\delta_l} - 1\right) P_l(\cos\theta). \tag{2.7}$$

The probability per unit time that the scattered particle will pass through a surface element $\mathrm{d}S = r^2 \mathrm{d}\Omega$ is $\mathbf{v}\,\mathrm{d}S\,|f_k|^2/r^2$, and its ratio to the current density in the incoming wave and to the solid angle $\mathrm{d}\Omega$ is the *differential cross section*

$$\frac{\mathrm{d}\sigma}{\mathrm{d}\Omega} = |f_k(\theta)|^2. \tag{2.8}$$

The total scattering cross-section is obtained by integrating the former expression over the whole solid angle:

$$\sigma = 2\pi \int_{-1}^{+1} \mathrm{d}(\cos\theta)|f_k(\theta)|^2. \tag{2.9}$$

Using the explicit expression for the scattering amplitude (2.7) and the orthogonality relation for the Legendre polynomials

$$\int_{-1}^{+1} \mathrm{d}(\cos\theta) P_m(\cos\theta) P_n(\cos\theta) = \frac{2}{2m+1} \text{ if } m = n, \quad 0 \text{ otherwise}$$

the total scattering cross-section can be expressed in terms of the phase shifts:

$$\sigma = \frac{4\pi}{k^2} \sum_{l=0}^{\infty} (2l+1) \sin^2 \delta_l. \tag{2.10}$$

The phase shifts have a pronounced dependence on energy, and to describe atomic scattering at low energy it is often sufficient to include only the s-wave ($l = 0$) contribution. In fact, when dealing with collisions between identical bosons or between two fermions in an antisymmetric spin state, scattering in odd partial waves (p, f, etc.) is prohibited by parity requirements. In addition, for a potential decreasing in the far field with a power-law dependence, $U(r) \simeq r^{-n}$, it is shown that [38]

$$\delta_l \propto \begin{cases} k^{2l+1} & \text{if } l < (n-3)/2 \\ k^{n-2} & \text{else.} \end{cases} \tag{2.11}$$

As a consequence, in the limit $k \to 0$ and for any potential decreasing faster than $1/r^3$ we have $\delta_l \ll \delta_0$ for any $l > 0$.

Some algebra shows that the $l = 0$ term in (2.5) can be recast as

$$R_{k0}(r) \simeq \cos\delta_0 \frac{\sin kr}{kr} + \frac{\sin\delta_0}{k}\frac{\cos kr}{r},$$

and in the limit of zero energy we obtain the asymptotic form

$$\psi \simeq 1 - \frac{a}{r}. \tag{2.12}$$

In the latter equation, we have introduced the *scattering length a*, defined for small k in terms of the s-wave phase shift by

$$k \cot\delta_0 = -\frac{1}{a}. \tag{2.13}$$

When $ka \to 0$, comparing (2.2) with (2.12) we find that the scattering amplitude is simply related to the scattering length by

$$f_k = -a. \tag{2.14}$$

In the same limit we have $\delta_0/k \simeq -a$ and the total cross section for distinguishable particles is given by

$$\sigma = 4\pi a^2. \tag{2.15}$$

In case the particles are indistinguishable, their wave function must be symmetric or antisymmetric under interchange of their relative position depending on whether the particles are bosons or fermions. The two directions specified by the polar angles θ, φ and $\pi - \theta, \varphi + \pi$ must be identified, and the scattering cross section takes the form

$$\frac{d\sigma}{d\Omega} = |f_k(\theta) \pm f_k(\pi - \theta)|^2, \tag{2.16}$$

where the $+$ $(-)$ sign applies to bosons (fermions). The total s-wave cross section is obtained by integrating the latter expression over all distinct final states. To avoid double counting one has to take into account only half of the solid angle, i.e. $0 \le \varphi < 2\pi$ and $0 \le \theta < \pi/2$, and finally finds

$$\sigma = 8\pi a^2 \tag{2.17}$$

for the case of identical bosons, while the total s-wave cross section vanishes for identical fermions.

The scattering length a can be determined accurately from a variety of experiments, e.g. photoassociative spectroscopy or analysis of Feshbach resonances, and plays a central role in the theory of cold collisions. When only low energy states are involved in a collision process, we will see that the scattering length is the only parameter entering an effective interaction that can be substituted for the full two-body potential. This is very appealing, since the original potential is deep and has a complicated structure, that cannot generally be calculated analytically.

To derive the effective interaction, it is useful to analyze the problem in the momentum representation, where the Schrödinger equation becomes an integral equation for $\psi(\mathbf{k})$:

$$\frac{\hbar^2 k'^2}{2\mu}\psi(\mathbf{k}') + \int \frac{d\mathbf{k}''}{(2\pi)^3}U(\mathbf{k}'-\mathbf{k}'')\psi(\mathbf{k}'') = \frac{\hbar^2 k^2}{2\mu}\psi(\mathbf{k}'), \qquad (2.18)$$

$U(\mathbf{k})$ being the Fourier transform of the potential and $E = \hbar^2 k^2/2\mu$ the energy eigenvalue. The wave function (2.1) reads

$$\psi(\mathbf{k}') = (2\pi)^3\delta(\mathbf{k}'-\mathbf{k}) + \psi_{\text{sc}}(\mathbf{k}') \qquad (2.19)$$

and satisfies the integral equation[1]

$$\left(\frac{\hbar^2 k^2}{2\mu} - \frac{\hbar^2 k'^2}{2\mu}\right)\psi_{\text{sc}}(\mathbf{k}') = U(\mathbf{k}'-\mathbf{k}) + \int \frac{d\mathbf{k}''}{(2\pi)^3}U(\mathbf{k}'-\mathbf{k}'')\psi_{\text{sc}}(\mathbf{k}''). \quad (2.20)$$

The former expression can be recast in the alternative form

$$\psi_{\text{sc}}(\mathbf{k}') = \left(\frac{\hbar^2 k^2}{2\mu} - \frac{\hbar^2 k'^2}{2\mu} + i0^+\right)^{-1} T(\mathbf{k}',\mathbf{k}). \qquad (2.21)$$

The first term on the right hand side of (2.21) is the *two-particle retarded Green's function G*, and an infinitesimal imaginary part has been added to enforce the boundary conditions of outgoing waves. The second term, the *(on-shell) scattering matrix T*, satisfies the Lippmann-Schwinger equation

$$T(\mathbf{k}',\mathbf{k}) = U(\mathbf{k}'-\mathbf{k}) + \int \frac{d\mathbf{k}''}{(2\pi)^3}U(\mathbf{k}'-\mathbf{k}'')\left(\frac{\hbar^2 k^2}{2\mu} - \frac{\hbar^2 k''^2}{2\mu} + i0^+\right)^{-1}T(\mathbf{k}'',\mathbf{k}),$$
$$(2.22)$$

or, more formally,

$$T = U + UGT. \qquad (2.23)$$

The scattered wave can be extracted from (2.21). We are only interested in the far field region, and we will make the approximation $T(\mathbf{k}',\mathbf{k}) \simeq T(0,\mathbf{k})$ since the important Fourier components are those for which $\mathbf{k}' \lesssim 1/\mathbf{r}$. Using the Fourier transform of the Green's function

$$G(\mathbf{r}) = \frac{2\mu}{\hbar^2}\int \frac{d\mathbf{k}'}{(2\pi)^3}\frac{e^{i\mathbf{k}'\cdot\mathbf{r}}}{k^2 - k'^2 + i0^+} = -\frac{\mu}{2\pi\hbar^2}\frac{e^{ikr}}{r} \qquad (2.24)$$

we find

$$\psi_{\text{sc}}(r) \simeq -\frac{\mu}{2\pi\hbar^2}T(0,\mathbf{k})\frac{e^{ikr}}{r}. \qquad (2.25)$$

Comparing (2.1) and (2.2) with (2.25), we see that the scattering amplitude is related to the T matrix by

$$f_k = -\frac{\mu}{2\pi\hbar^2}T(0,\mathbf{k}). \qquad (2.26)$$

---

[1] We use $(k'^2 - k^2)\delta(\mathbf{k}'-\mathbf{k}) = 0$, where the equality is to be intended in the parlance of distribution theory, i.e. $\int d\mathbf{k}\,\phi(\mathbf{k})(k'^2 - k^2)\delta(\mathbf{k}'-\mathbf{k}) = 0$ for any test function $\phi(\mathbf{k})$ with bounded support not having a singularity in $\mathbf{k} = \mathbf{k}'$.

The Lippmann-Schwinger equation allows one to obtain an effective potential that can be used to describe low-energy collisions in a dilute gas. In order to see how, let us split the integral appearing in (2.22) into two parts, first summing over states with energy greater than $E_c = \hbar^2 k_c^2 / 2\mu$, and then summing over states with lower energy[2]. The first summation defines a quantity $\tilde{U}_{E_c}(\mathbf{k}', \mathbf{k})$ that satisfies

$$\tilde{U}_{E_c}(\mathbf{k}', \mathbf{k}) = U(\mathbf{k}' - \mathbf{k}) + \int_{k'' > k_c} \frac{d\mathbf{k}''}{(2\pi)^3} U(\mathbf{k}' - \mathbf{k}'') \left(\frac{\hbar^2 k^2}{2\mu} - \frac{\hbar^2 k''^2}{2\mu} + i0^+ \right)^{-1} \tilde{U}_{E_c}(\mathbf{k}'', \mathbf{k})$$

and depends explicitly on the specific energy cut-off E_c. The second step gives the T matrix in terms of the effective interaction $\tilde{U}$:

$$T(\mathbf{k}', \mathbf{k}) = \tilde{U}_{E_c}(\mathbf{k}', \mathbf{k}) + \int_{k'' < k_c} \frac{d\mathbf{k}''}{(2\pi)^3} \tilde{U}_{E_c}(\mathbf{k}', \mathbf{k}'') \left(\frac{\hbar^2 k^2}{2\mu} - \frac{\hbar^2 k''^2}{2\mu} + i0^+ \right)^{-1} T(\mathbf{k}'', \mathbf{k}).$$

This last equation shows that, if one replaces the bare interaction U by $\tilde{U}_{E_C}$, the full T matrix can be obtained including only a limited subset of low-energy states. If we let $E_c \to 0$, the effective interaction reduces to the T matrix, and comparing (2.14) to (2.26) we obtain

$$U_0 \equiv \lim_{k_c \to 0} \tilde{U}_{E_c}(0, 0) = T(0, 0) = \frac{2\pi \hbar^2 a}{\mu}. \tag{2.27}$$

In the zero energy, long wavelength limit, the effective s-wave interaction depends on a single parameter, the scattering length. If the typical length over which the two-body potential is appreciably different from zero is small compared to the interparticle distance, interactions in a cold gas can be accurately described by a s-wave contact interaction commonly referred to as the *Fermi pseudopotential*, whose strength is given precisely by the effective interaction U_0 calculated above:

$$U(r) = U_0 \left. \frac{\partial (r \dots)}{\partial r} \right|_{r=0} \delta(\mathbf{r}). \tag{2.28}$$

Wave functions with s-wave symmetry diverge in three dimensions at most like $1/r$ in $r = 0$, and the derivative term has been introduced to regularize the contact potential at the origin, i.e. to give a definite meaning to the combination $U(0)\psi(0)$. By introducing the pseudopotential (2.28), the whole effect of the interaction between the two particles is replaced by a vanishing potential supplemented by a boundary condition for the logarithmic derivative of $r\psi$ at the origin:

$$\frac{1}{r\psi} \left. \frac{\partial (r\psi)}{\partial r} \right|_{r=0} = -\frac{1}{a}. \tag{2.29}$$

---

[2]Using a formal notation, we write $G = G_> + G_<$, and define an effective interaction $\tilde{U}$ that satisfies

$$\tilde{U} = U + U G_> \tilde{U}.$$

Multiplying on the left by U^{-1} and on the right by $\tilde{U}^{-1}$, we get $U^{-1} = \tilde{U}^{-1} + G_>$. From (2.23) we have $U^{-1} = T^{-1} + G$, and equating the right hand sides of the two latter equations we find T as a function of $\tilde{U}$:

$$T = \tilde{U} + \tilde{U} G_< T.$$

2.1   Energy-dependent scattering

For strong interactions or small interparticle separations, energy plays an important role in determining scattering properties: consequently, the theory presented in the preceding Section must be improved. When the scattering length $|a|$ becomes larger than $1/k$ the simple relation $f_k = -a$ is no longer valid and the scattering amplitude becomes energy-dependent. At the same time, the introduction of a contact potential can be justified only in the low-density limit. In this Section we first find the lowest order energy corrections to the scattering amplitude and cross section, then show how energy shifts due to interparticle interactions are related to phase shifts, and finally present a modified GP equation that takes into account the non-zero range of the effective atom-atom interaction.

The energy-dependence of the s-wave cross-section is simply found keeping the only $l = 0$ term in Eq. (2.7), resulting in[3]

$$f_k = \frac{1}{k \cot \delta_0 - ik} = -\frac{1}{a^{-1} + ik}. \tag{2.30}$$

Alternatively, the Lippmann-Schwinger equation can be expanded in increasing powers of the interaction U and formally re-summed to find

$$T = U + UGU + UGUGU + \ldots = U\frac{1}{1 - GU}. \tag{2.31}$$

For the special case of the pseudopotential (2.28), the T matrix admits the analytic form

$$T(0, \mathbf{k}) = \frac{2\pi\hbar^2}{\mu} \frac{1}{a^{-1} + ik}, \tag{2.32}$$

and comparing with (2.26) we again find the scattering amplitude (2.30). The differential energy-dependent cross section for distinguishable particles is given by

$$\frac{d\sigma}{d\Omega}(k) = \frac{a^2}{1 + k^2 a^2}, \tag{2.33}$$

in accord with the *optical theorem*

$$\sigma = \frac{4\pi}{k} \text{Im } f_k, \tag{2.34}$$

that links the total cross section to the scattering amplitude[4]. As stated in Chap. 1, Feshbach resonances can be exploited to tune the scattering length to arbitrary values: the energy-dependence of the scattering cross-section must be taken into account whenever one enters the regime of strong interactions where $k|a| \gtrsim 1$, as is evident from Eq. (2.33). When $|a|$ becomes much bigger than k^{-1} the cross section saturates to the value $\sigma = 4\pi/k^2$ and is said to be "unitarity limited".

---

[3]We use

$$\cot \delta = i \left(\frac{e^{i\delta} + e^{-i\delta}}{e^{i\delta} - e^{-i\delta}} \right) = i \left(1 + \frac{2}{e^{2i\delta} - 1} \right).$$

[4]If higher partial waves are included, the theorem is still valid provided f_k is substituted by $f_k(0)$, the scattering amplitude in the forward direction.

At sufficiently high energies $k \cot \delta_0$ is no longer a constant, and the first correction to Eq. (2.13) is generally written as [39]

$$k \cot \delta_0 = -\frac{1}{a} + \frac{1}{2} r_e k^2 + o\left(k^2\right), \qquad (2.35)$$

that *defines* the effective range r_e. This formula is correct for short range potentials falling off at infinity faster than any power of $1/r$, and has been extensively used in nuclear theory. When the effective range is taken into account, the scattering amplitude becomes

$$f_k = \frac{1}{k \cot \delta_0 - ik} = -\frac{a}{1 + ika - a r_e k^2/2}. \qquad (2.36)$$

From the latter equation, we deduce that at non-zero energies a contact potential (for which $r_e = 0$) reproduces the correct scattering amplitude as long as

$$k \left| r_e \right| \ll 1. \qquad (2.37)$$

For alkali atoms typically $r_e \sim a$ and the latter requirement coincides with the low-energy condition $k|a| \ll 1$. As long as Eq. (2.37) is satisfied, the contact potential can be used to model interparticle interactions even in presence of a Feshbach resonance, since r_e is unaffected by the rapid divergence of a as a function of the external field.

The case $a \to 0$ deserves special mention: expanding (2.36) for small values of the scattering length, one finds

$$f_k = -a + ika^2 - \frac{1}{2} r_e a^2 k^2 + o\left(a^2\right). \qquad (2.38)$$

It has indeed been shown analytically for both an attractive square well [40] and a van der Waals interaction [41] that the effective range diverges as $a \to 0$ in such a way as to keep constant the quantity $r_e a^2$, the prefactor of k^2 in (2.38). The behavior of a and r_e are depicted in Fig. 2.1 for the square well potential. In Sec. 5.3 we will find a similar divergence of r_e when solving the problem of a free particle colliding with a trapped scatterer (see Fig. 5.11). For $a \to 0$ the condition (2.37) for the applicability of a contact potential should then be substituted by

$$k^2 \left| r_e a^2 \right| \ll |a| \qquad \text{(when } a \to 0\text{)}. \qquad (2.39)$$

We turn now to the possibility of including non-zero range effects in the GP equation. On general grounds, it is possible to show that mean field energy shifts are proportional to phase shifts (see e.g. [42]). To understand how energy shifts are related to interactions, a simple example can be useful. Let us consider two bosons enclosed in a spherical box of radius R (in the relative coordinate). The exact wave function for two non-interacting particles is of the form

$$\Psi_0 = A \frac{\sin(k_0 r)}{r}, \qquad (2.40)$$

where the boundary condition of infinite walls at $r = R$ implies that $k_0 R = n\pi$, and normalization to unity requires that $A^{-2} = 2\pi R$. If we now turn on any interaction (with the only condition that it vanishes at infinity faster than r^{-2}),
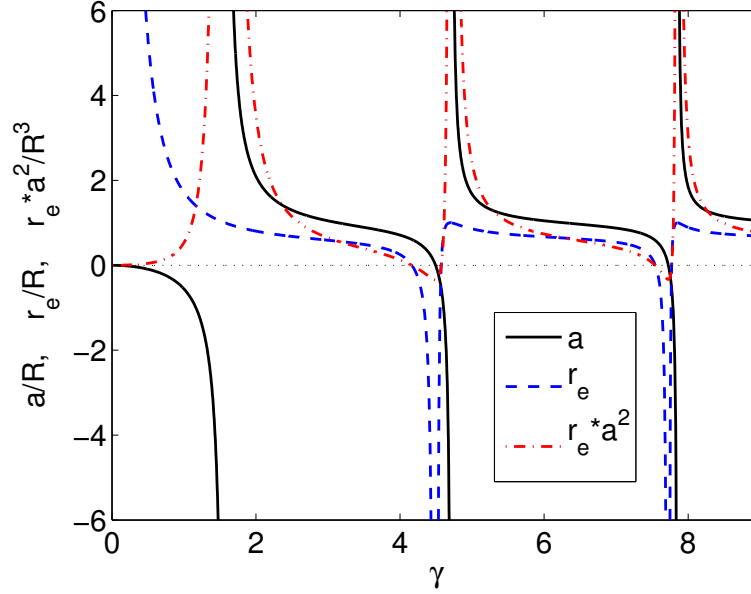
Figure 2.1: Scattering length a, effective range r_e and $r_e a^2$ for a 3D attractive square well of width R and depth $-V_0$, plotted as a function of the adimensional parameter $\gamma = \sqrt{-V_0 m R^2/\hbar^2}$.

the asymptotic wave function will have the same form, but will be phase shifted:

$$\Psi = A \frac{\sin(kr + \delta)}{r}. \tag{2.41}$$

The new boundary condition is $kR + \delta = n\pi$ and implies a wave vector shift $\Delta k = k - k_0 = -\delta/R$. The energy shift is then given by

$$\Delta E = \frac{\hbar^2}{\mu} k \cdot \Delta k = \frac{\hbar^2}{\mu} k \cdot \left(-\frac{\delta}{R}\right) = \frac{2\pi\hbar^2}{\mu} \left(-\frac{\delta}{k}\right) |\Psi_0(0)|^2. \tag{2.42}$$

This simple example shows the general feature that the energy shift due to interparticle interaction is proportional to the phase shift δ.

For small phase shifts $\delta \sim \tan\delta - \tan^3\delta/3$ and we find:

$$-\frac{\delta}{k} = a \cdot \left(1 - g_2 k^2\right) \tag{2.43}$$

where we have defined

$$g_2 \equiv \frac{1}{3}a^2 - \frac{1}{2}a r_e. \tag{2.44}$$

The energy shift is then given by

$$\Delta E = \frac{2\pi\hbar^2 a}{\mu} \left[1 - g_2 k^2\right] |\Psi_0(0)|^2. \tag{2.45}$$

As shown in [43, 44], the energy shift can be inserted in the energy functional to obtain a modified GP equation containing a derivative term:

$$i\hbar\frac{\partial}{\partial t}\Psi = \left[-\frac{\hbar^2}{2m}\nabla^2 + V(r) + U_0 \left\{ |\Psi|^2 + g_2\nabla^2\left(|\Psi|^2\right) \right\} \right]\Psi \qquad (2.46)$$

It is interesting to note that in the case of hard spheres of diameter a the boundary conditions on the surface of the sphere impose $\delta = -ka$ and $r_e = 2a/3$: as a result the g_2 coefficient vanishes, in accord with the fact that δ/k is manifestly independent from the energy. We note in passing that in Ref. [44] the authors started from the erroneous assumption of proportionality between forward scattering amplitudes and energy shifts, and consequently obtained the wrong result $g_2 = a^2 - ar_e/2$.

Starting from the ideas above, Roth and Feldmeier [43] have performed a detailed analysis of the problem of constructing an energy-dependent interaction. They expanded the phase shift corresponding to each angular component in increasing powers of k^2,

$$\delta_l(k) = k^{2l+1}\sum_{\nu=0}^{\infty}\frac{1}{\nu!}c_l^{(\nu)}k^{2\nu}, \qquad (2.47)$$

and developed a contact interaction that reproduces the correct two-body energy shifts taking into account all partial waves via derivative couplings.

Special care needs to be taken when employing an effective range expansion, since atomic potentials in general are not short-ranged: as shown in [45] the expansion given in Eq. (2.35) is strictly correct only for potentials that go to zero at least as fast as the Van der Waals one (r^{-6}). As an example, they find that for two particles interacting through a potential with a $1/r^4$ tail the expansion of the s-wave phase shift contains already a term linear in $k \propto \sqrt{E}$,

$$k\cot\delta = -\frac{1}{a} + \frac{\pi\beta_4^2}{3a^2}k + Ak^2\ln(k\beta_4) + Bk^2 + O\left(k^2\right), \qquad (2.48)$$

(where β_4, A and B are constants with dimensions of a length) and the definition of an effective range itself is meaningless for this potential.

Chapter 3

Static properties of ions in atomic BECs

The idea of studying properties of ions inside a Bose-Einstein condensate came to us thinking of what has been done in the 1960s in the context of liquid helium, where ions proved to be very useful tools to elucidate the nature of excitations inside the superfluid, and were essential to put in evidence the existence of vortex lattices in rotating liquid ^{4}He (for a review on early results, see [46]). The first experiments on ions in an ultracold gas of ^{87}Rb atoms were reported by Ciampini *et al.* [6], who produced ions by irradiating condensates and thermal ensembles with laser pulses which ionize atoms through one- and two-photon absorption processes. Upon ionization of about 10% of the cloud, large trap losses and important density profile modifications were measured and characterized as a function of the ionizing laser parameters.

Theoretically, the capture of atoms into weakly bound states of the atom-ion potential has been considered in Ref. [8]. In this Chapter we consider the structure of a positive alkali ion in a Bose-Einstein condensate when there is no capture of atoms into bound states, and in particular we calculate the excess number of atoms associated with an ion. We shall demonstrate that this number is typically of order 10–100, either positive or negative.

The interaction between an atom and a positively charged alkali-metal ion (charge e), which are separated by a distance r, is given at large distances by the polarization potential caused by the electrostatic field $\mathcal{E}_{\text{es}}$ due to the ion, $\mathcal{E}_{\text{es}} = e/4\pi\epsilon_0 r^2$. The change in the energy of the neutral atom amounts to

$$V = -\alpha \frac{\mathcal{E}_{\text{es}}^2}{2}, \tag{3.1}$$

α being the polarizability of the atom. Writing the polarizability as $\alpha = 4\pi\epsilon_0 \tilde{\alpha}$, where $\tilde{\alpha}$ has the dimension of volume, the energy shift of an atom due to the ion becomes

$$V(r) = -\tilde{\alpha} \frac{e_0^2}{2r^4}, \tag{3.2}$$

with $e_0^2 \equiv e^2/4\pi\epsilon_0$. At short distances ($r \lesssim 10a_0$) the potential has a repulsive core. An important characteristic length, which we denote by β_4, may be identified by equating the kinetic energy $\hbar^2/2m\beta_4^2$ to the potential energy $V(\beta_4)$,

and is given by

$$\beta_4 = \sqrt{\frac{\tilde{\alpha}}{a_0} \frac{m}{m_e}}.$$ (3.3)

Here m denotes the mass of a neutral atom, m_e is the electron mass and $a_0 = \hbar^2/m_e e_0^2 \sim 0.53\text{Å}$ is the Bohr radius. Using the measured values $\tilde{\alpha} = 320a_0^3$ for ^{87}Rb and $\tilde{\alpha} = 163a_0^3$ for ^{23}Na, one finds $\beta_4^{\text{Rb}} \approx 7150a_0$ and $\beta_4^{\text{Na}} \approx 2620a_0$. The quantity β_4 gives the distance from the ion beyond which the zero-energy atom-ion wave function ceases to oscillate, and it sets the scale of atom-ion scattering lengths, but their actual values depend on the details of the potential at short distances.

We begin by deriving from thermodynamics a general expression for the excess number of atoms around an ion and show that in dilute systems the excess number depends only on the ratio of the atom-ion and atom-atom scattering lengths. As we shall see, this approach suggests that the number of atoms associated with an ion is typically of order 10–100, but that it may be either positive or negative. In denser systems the excess number must be obtained from microscopic considerations, and we shall determine the structure of an ion immersed in a Bose-Einstein condensate at zero temperature, assuming that atom-atom interactions may be described within the framework of the Gross-Pitaevskii (GP) mean-field approach. We present solutions of the GP equation for a number of potentials which include a hard core repulsion, an attractive square well, and one which resembles the atom-ion interaction, a hard core with a $1/r^4$ attraction at larger distances.

For a given inner boundary condition, the Schrödinger equation has only one solution for a given value of the energy. By contrast, the GP equation is not linear and can have more than one solution for a given chemical potential. For potentials like the atom-ion one that can support two-body bound states, we shall find that at low densities there are $2\nu_S + 1$ solutions of the GP equation, where ν_S is the number of bound states of the Schrödinger equation for the same potential. With increasing density, pairs of solutions merge and disappear until there is only a single solution with no nodes. We shall illustrate this behavior for two potentials, an attractive square well and one with an attractive $1/r^4$ tail. An important question is which of these solutions is physically relevant. At low condensate densities, one expects the wave function close to the ion to resemble the zero-energy solution of the Schrödinger equation, and to have ν_S nodes. This will be the case unless inelastic processes can populate lower-lying states. We find that with increasing condensate density, this solution ceases to exist. This indicates that the evolution of the state with density cannot be continuous even in the absence of inelastic processes.

The plan of the Chapter is as follows. In Sec. 3.1 we derive the excess number of atoms in the dilute limit by means of thermodynamic considerations, and address the question of the validity of the Gross-Pitaevskii equation in the present context. Section 3.2 contains a description of the asymptotic behavior of the condensate wave function far from the ion. In Sec. 3.3 we consider two simple potentials to illustrate important general features of our results, and in Sec. 3.4 we analyze the case of a potential that, like the actual atom-ion potential, behaves as r^{-4} at large distances. We calculate the excess number of atoms from numerical solutions of the Gross-Pitaevskii equation for a given background condensate density. The concluding section, Sec. 3.5, discusses our

main results. The analytic solution of a related problem, an interacting gas in a one-dimensional square well, is deferred to Appendix A.

3.1   Thermodynamic considerations

We wish to calculate the excess number of particles associated with an ion. To define this quantity precisely, we imagine adding an ion to a condensate. This will generally change the density of atoms far from the ion by an amount that varies as $1/V$, where V is the volume of the system. A natural definition of the excess number of atoms ΔN associated with the ion is the number of particles that must be added to keep the atom chemical potential constant, since this will ensure that the properties of the condensate far from the ion are unaltered by the addition of the ion. In terms of the microscopic density of atoms $n(r)$ around the ion, the excess number is given by

$$\Delta N = 4\pi \int_0^\infty dr \; r^2 \left[n(r) - n_0 \right], \tag{3.4}$$

where n_0 is the density of atoms at large distances from the ion.

This is analogous to what has been done earlier to calculate the excess number of ^{4}He atoms associated with a ^{3}He impurity in liquid ^{4}He [47, 48]. We shall denote the energy per unit volume as $\mathcal{E}(n_a, n_i)$, where n_a and n_i are the number densities of atoms and ions, respectively. The chemical potential of the atoms is given by

$$\mu_a = \frac{\partial \mathcal{E}}{\partial n_a}, \tag{3.5}$$

and therefore the condition that this be unchanged by adding one ion and ΔN atoms is

$$\frac{\partial^2 \mathcal{E}}{\partial n_a \partial n_i} + \frac{\partial^2 \mathcal{E}}{\partial n_a^2} \Delta N = 0, \tag{3.6}$$

or

$$\Delta N = -\frac{\partial^2 \mathcal{E}}{\partial n_a \partial n_i} \bigg/ \frac{\partial^2 \mathcal{E}}{\partial n_a^2} \; . \tag{3.7}$$

One may also calculate ΔN from the change ΔF in the thermodynamic potential $F = E - \mu_a N$ when a single ion is added to the system at constant μ_a. Here E is the total energy and N the total number of atoms. Since the number of atoms is given by

$$N = -\frac{\partial F}{\partial \mu_a}, \tag{3.8}$$

it follows immediately that

$$\Delta N = -\frac{\partial \Delta F}{\partial \mu_a}. \tag{3.9}$$

Provided the volume considered is large compared with the scale of the atom excess around the ion, ΔF will be independent of the volume.

Let us begin by making estimates for a dilute gas. Provided the scattering of atoms by atoms and of atoms by ions may be treated as independent binary events, the energy density may be expressed in terms of the scattering lengths

associated with the atom-atom and atom-ion interactions. If ion-ion interactions are neglected, we may write

$$\mathcal{E}(n_\mathrm{a}, n_\mathrm{i}) = \frac{1}{2} U_\mathrm{aa} n_\mathrm{a}^2 + U_\mathrm{ai} n_\mathrm{a} n_\mathrm{i}, \tag{3.10}$$

and therefore from Eq. (3.7) we obtain

$$\Delta N = -\frac{U_\mathrm{ai}}{U_\mathrm{aa}}. \tag{3.11}$$

The mean-field interaction constant U_{jl} for species j and l, which may be either atoms (a) or ions (i), is related to the scattering length a_{jl} by

$$U_{jl} = \frac{2\pi\hbar^2 a_{jl}}{m_{jl}}, \tag{3.12}$$

where $m_{jl} = m_j m_l/(m_j + m_l)$ is the reduced mass of the two particles. Our result can therefore be expressed as

$$\Delta N = -\frac{m_\mathrm{aa}}{m_\mathrm{ai}} \frac{a_\mathrm{ai}}{a_\mathrm{aa}}. \tag{3.13}$$

If, as in Ref. [6], the ion is obtained by photoionization of the condensate itself, the latter expression reduces to

$$\Delta N = -a_\mathrm{ai}/a_\mathrm{aa}. \tag{3.14}$$

To obtain an order of magnitude estimate of the excess number of atoms associated with an ion, we note that the characteristic scale for the magnitudes of atom-ion scattering lengths $|a_\mathrm{ai}|$ is set by β_4, given in Eq. (3.3), while the scale for the magnitudes of atom–atom scattering lengths $|a_\mathrm{aa}|$ is set by

$$\beta_6 = \left(2\frac{m}{m_\mathrm{e}}C_6\right)^{1/4} a_0. \tag{3.15}$$

Here C_6 is the coefficient of r^{-6} in the van der Waals interaction, expressed in atomic units. Thus we arrive at the estimate

$$|\Delta N| \sim \frac{\beta_4}{\beta_6} \sim \left(\frac{\tilde{\alpha}^2}{2a_0^6 C_6}\frac{m}{m_\mathrm{e}}\right)^{1/4}, \tag{3.16}$$

which is of order 35 for Rb and 25 for Na.

The fact that the excess number of atoms is so large indicates that it may well be a poor approximation to regard the ion as a free particle, with mass equal to the bare ion mass. Rather, the recoil of the ion will be suppressed by the other atoms surrounding the ion, and if $\Delta N \gg 1$ it will be a better approximation to regard the ion as being stationary. In that case the excess number of atoms will be given by

$$\Delta N = -\frac{a_\mathrm{ai}(m)}{2a_\mathrm{aa}}, \tag{3.17}$$

where the argument of a_ai indicates that the scattering length is to be evaluated for a reduced mass equal to the atom mass. Expression (3.17) gives a value for

ΔN that is typically of the same order of magnitude as that given by Eq. (3.16). However, we stress the fact that the estimate for ΔN depends sensitively on the value of the effective mass of the ion, since the atom-ion potential has many bound states, and therefore relatively small changes in the reduced mass can result in large changes in the scattering length. Given that in the limit of low atom density the magnitude of the excess number of atoms is expected to be very much greater than unity, the result (3.14) will generally not give a realistic estimate even in that case.

3.1.1 Validity of approximations

The perturbation induced by the ionic potential is very strong. Therefore the question arises of whether the customary assumption of an essentially zero range for the atom-atom interaction is valid. We address this point in Appendix A, where we argue that the corrections to the GP result should not be large for the properties of interest here. Here we examine the conditions under which it is a good approximation to replace the effective atom-atom interaction by the standard expression (3.12). Later we shall estimate the density below which the dilute gas result (3.13) would be expected to hold. For nonzero wave numbers k, the quantity that enters the expression for the energy shift is $-\delta/k$, where δ is the s-wave phase shift, rather than a [42]. Since a typical energy scale for changes in δ/k is set by $\hbar^2/2m\beta_6^2$, while the potential depth is given by $\tilde{\alpha}e_0^2/2r^4$, we expect that the scattering length approximation will fail when

$$\frac{\tilde{\alpha}e_0^2}{2r^4} \gg \frac{\hbar^2}{2m\beta_6^2} \quad \text{or} \quad r^4 \ll \beta_4^2\beta_6^2. \qquad (3.18)$$

The Gross-Pitaevskii approach should therefore be valid if the phase shift due to the region where $r \ll \bar{r} = (\beta_4\beta_6)^{1/2}$ is negligible. To estimate this phase shift, we make a semiclassical approximation to the GP equation. This gives for the total accumulated phase out to a distance r

$$\Phi(r) \approx \int_0^r dr' \sqrt{\frac{2m}{\hbar^2}[\mu - V(r') - n(r')U_0]}. \qquad (3.19)$$

Deep in the ionic potential, the wave function is given to a good approximation by the semiclassical result, which has an amplitude

$$\psi \propto (rp_{\text{cl}}^{1/2})^{-1}, \qquad (3.20)$$

where $p_{\text{cl}}(r) = [2mV(r)]^{1/2}$ is the classical momentum of a particle of zero total energy in the presence of the potential. For the r^{-4} potential, the amplitude of the wave function is therefore independent of r, and therefore we may replace the mean-field energy to a first approximation by a constant $\tilde{n}U_0$, where $\tilde{n}$ is independent of r. Expanding expression (3.19) in the deviation $n_0 - \tilde{n}$ we find

$$\Phi(r) \approx \Phi_0(r) + (n_0 - \tilde{n})\frac{2mU_0}{\hbar^2}\int_0^r dr'\frac{1}{2\sqrt{-2mV(r')/\hbar^2}}. \qquad (3.21)$$

Due to the mean-field interaction, the accumulated phase out to a distance $r \sim \bar{r} = (\beta_4\beta_6)^{1/2}$ is therefore changed by an amount

$$\delta\Phi(\bar{r}) \approx (n_0 - \tilde{n})a_{\text{aa}}(\beta_4\beta_6^3)^{1/2}. \qquad (3.22)$$

If we take the interior density to be of the same order of magnitude as that far from the ion, one finds

$$\delta\Phi(\bar{r}) \sim \frac{\beta_4^{1/2}\beta_6^{3/2}}{\xi^2}, \tag{3.23}$$

where the healing length for the bulk condensate ξ is defined as

$$\xi = \frac{1}{\sqrt{8\pi a_{\mathrm{aa}}n_0}}. \tag{3.24}$$

Since under experimental conditions the healing length is typically comparable to β_4, while β_6 is two orders of magnitude smaller, this shows that the region close to the ion where the Gross-Pitaevskii equation fails is likely to be unimportant for the properties analyzed in this work.

On the basis of the above calculation, we may also estimate the density below which the low-density result (3.13) is valid. Using the approximations above, we find that the total accumulated phase out to a distance $\sim \beta_4$, where the semiclassical treatment fails, is of order

$$\delta\Phi(\beta_4) \sim \frac{\beta_4^2}{\xi^2}. \tag{3.25}$$

This indicates that changes to the accumulated phase can be significant under typical experimental conditions (to give an order of magnitude, $\xi \approx 5000a_o$ for ^{87}Rb at a density of $n_0 = 10^{14}$ atoms/cm^3). As we will see in Sec. 3.4, when the density is high enough that the interaction energy becomes comparable to the energy associated with the polarization potential (i.e. when $\delta\Phi(\beta_4) \approx 1$), the mean field repulsion between the atoms alters substantially the spectrum of the system, causing the merging and disappearance of pairs of states.

3.2   Microscopic theory

We now turn to microscopic considerations. Since, as we shall see, the distortion of the condensate wave function in the vicinity of an ion extends to large distances from the ion and involves many atoms, we expect that the effective mass of an ion and its dressing cloud will be much larger than that of an atom, and we may regard the ion as being static. To describe the structure of the condensate in the vicinity of an ion we must therefore calculate the structure of the condensate in a static external potential given by the atom-ion interaction. Provided the length scale on which the condensate wave function ψ varies in space is sufficiently large, we may do this by employing the Gross-Pitaevskii equation with the interaction of atoms with the ion included as an external potential,

$$\left[-\frac{\hbar^2}{2m}\nabla^2 + V(r) + U_0\left|\psi\right|^2\right]\psi = \mu\psi. \tag{3.26}$$

Here and in what follows we shall denote the chemical potential of an atom by μ, and for simplicity we have written $U_0 \equiv U_{\mathrm{aa}} = 4\pi\hbar^2 a_{\mathrm{aa}}/m$, since $m_{\mathrm{aa}} = m/2$. We wish to find solutions that tend to a constant at large distances from the ion, and since the potential is spherically symmetric, these solutions depend only on the radial coordinate r. Thus Eq. (3.26) becomes

$$-\frac{\hbar^2}{2m}\frac{1}{r}\frac{d^2}{dr^2}(r\psi) + \left[V(r) + U_0\left|\psi\right|^2\right]\psi = \mu\psi. \tag{3.27}$$

The behavior of the condensate wave function at large distances depends on the nature of the potential $V(r)$. On linearizing the GP equation (3.26) and making use of the fact that the chemical potential is related to the condensate wave function ψ_0 at large distances by the relation $\mu = n_0 U_0$ where $n_0 = |\psi_0|^2$, one finds that the deviation

$$\delta\psi = \psi - \psi_0 \tag{3.28}$$

of the condensate wave function from its asymptotic value satisfies the linearized GP equation

$$-\frac{\hbar^2}{2m}\frac{1}{r}\frac{d^2}{dr^2}(r\psi) + [V(r) + 2U_0 n_0]\,\delta\psi = -V(r)\psi_0. \tag{3.29}$$

For potentials with a finite range, one may neglect the potential at large distances from the ion, and the solution that vanishes for $r \to \infty$ is thus given by

$$\delta\psi \propto \frac{\mathrm{e}^{-k_\xi r}}{r}, \tag{3.30}$$

where $k_\xi = \sqrt{2}/\xi$ and the healing length ξ is defined in Eq. (3.24).

For a potential, such as the atom-ion potential, that falls off at large distances less rapidly than the solution (3.30), the behavior is different. The leading term in the solution for large r is then the Thomas–Fermi result ψ_{TF}, given by

$$V(r) + U_0|\psi_{\mathrm{TF}}|^2 = \mu, \tag{3.31}$$

which, for the atom-ion potential with the asymptotic form given by Eq. (3.2), amounts to

$$n_{\mathrm{TF}}(r) = n_0 - \frac{V(r)}{U_0} = n_0\left(1 + \frac{(\xi\beta_4)^2}{r^4}\right) \tag{3.32}$$

or, to first order in V,

$$\psi_{\mathrm{TF}} \approx \psi_0 - \frac{V(r)}{2U_0\psi_0}, \tag{3.33}$$

where we have taken ψ_0 to be real. The density perturbation at large distances is seen to be always positive. Corrections to this result for smaller r may be calculated from Eq. (3.29) by neglecting the potential on the left hand side of the equation:

$$\left[-\frac{1}{r}\frac{d^2}{dr^2}r + k_\xi^2\right]\delta\psi = -\frac{2m}{\hbar^2}V(r)\psi_0. \tag{3.34}$$

By inspection of (3.34) it is evident that the leading term for large r of the particular solution to the inhomogeneous equation is given by $\delta\psi = -(2m/\hbar^2 k_\xi^2)V(r)\psi_0$, which yields the Thomas-Fermi expression (3.33). To obtain the first correction to this result, we iterate Eq. (3.34) by moving the derivative term to the right hand side and replacing $\delta\psi$ in it by the Thomas-Fermi solution. For the ionic potential this results in

$$\frac{\delta\psi}{\psi_0} = -\frac{2m}{\hbar^2 k_\xi^2}V(r)\left(1 + \frac{12}{k_\xi^2 r^2}\right). \tag{3.35}$$

The leading correction to the Thomas-Fermi result for $\delta\psi$ given in (3.33) is thus seen to be proportional to r^{-6}. Since we have already neglected the potential

energy on the left hand side of (3.29), we cannot by this method obtain higher-order corrections to the particular solution than the one exhibited in (3.35).

By including in the general solution the exponentially decaying term we thus get the asymptotic result

$$\frac{\delta\psi}{\psi_0} \sim -\frac{V(r)}{2n_0U_0}\left(1+\frac{6\xi^2}{r^2}\right) + C\frac{e^{-k_\xi r}}{r}, \tag{3.36}$$

where C is an arbitrary constant.

For $r \to \infty$ the asymptotic behavior of the solution is always given by the TF result. However, whether or not this behavior is relevant for determining the structure of most of the cloud of atoms surrounding the ion depends on the relative size of the two characteristic lengths, β_4 and ξ. On the one hand, for $\beta_4 \gg \xi$ most of the cloud will be described by the TF approximation, and only at distances less than $\sim \xi$ will the exponential term become important. On the other hand, for $\xi \gg \beta_4$ (i.e. for low external density) the structure will be dominated by the exponential term, and the TF tail will become important quantitatively only at very large r. At shorter distances from the ion, the mean-field energy becomes small compared with the atom-ion potential and the GP equation reduces to a good approximation to the Schrödinger equation.

3.3   Simple model potentials

Before presenting results for the attractive $1/r^4$ potential we begin by examining two simpler model potentials, a repulsive hard-core and a spherical well.

3.3.1   Hard-core potential

Consider an interacting Bose-Einstein condensed gas in the presence of a repulsive hard-core potential of radius R. This model may be treated analytically in both the small and large core radius limits. The solution to the GP equation at large distances from the ion is given by Eq. (3.30),

$$\psi \simeq \sqrt{n_0}\left(1 + C\frac{\exp(-k_\xi r)}{r}\right). \tag{3.37}$$

If one assumes that this expression holds for all r greater than R, we can determine the constant of proportionality C by imposing the boundary condition $\psi(R) = 0$. This gives $C = -Re^{k_\xi R}$. For r close to R this has the form of the scattering solution for the Schrödinger equation, $\psi = 1 - R/r$. In fact, for $R/\xi \ll 1$ this solution becomes essentially exact, since this function fails to satisfy the GP equation only in the region where $r \simeq R$, and in this region the total change in the slope $d\chi/dr$ of the radial wave function is small and may be neglected. As an illustration of this fact, we calculate the excess number of particles, which is given by Eq. (3.4), and find

$$\begin{aligned}
\Delta N &= 4\pi n_0\left[-\frac{R^3}{3} + \int_R^\infty dr\, r^2\left(-2R\frac{e^{-k_\xi(r-R)}}{r} + R^2\frac{e^{-2k_\xi(r-R)}}{r^2}\right)\right] = \\
&= -4\pi n_0\left[\frac{R^3}{3} + R\xi^2 + \frac{3R^2\xi}{2\sqrt{2}}\right]. \tag{3.38}
\end{aligned}$$

For $\xi \gg R$, this reduces to

$$\Delta N = -\frac{R}{2a_{\mathrm{aa}}}. \tag{3.39}$$

Let us now compare this result with the one derived on the basis of thermodynamic arguments. For a hard-core potential the scattering length coincides with the core radius. Since we have assumed the ion to be stationary, its effective mass is taken to be infinitely large, and therefore the reduced mass for the ion and an atom is m, rather than the value $m/2$ one obtains for an ion and an atom with equal masses. Thus, this result is in precise agreement with Eq. (3.13).

When the core radius is much larger than the healing length, the wave function reaches its asymptotic value on a length scale that is short compared to R. Writing Eq. (3.27) as

$$\left[-\frac{\hbar^2}{2m}\frac{d^2}{dr^2} + V(r) + U_0\frac{|\chi|^2}{r^2} \right]\chi = \mu\chi \tag{3.40}$$

with $\chi = r\psi$, we can therefore replace the factor $1/r^2$ appearing in the nonlinear term by the constant $1/R^2$ and we are left with an effectively one-dimensional GP equation whose solution is

$$\psi = \sqrt{n_0}\tanh\frac{r-R}{\sqrt{2}\xi}, \quad r \geq R, \tag{3.41}$$

and zero otherwise, as may be seen by inspection. The excess number of particles is given by

$$\Delta N = -\frac{4}{3}\pi R^3 n_0 - \frac{R^2}{\sqrt{2}a_{\mathrm{aa}}\xi}, \tag{3.42}$$

where the leading term is due to exclusion of atoms from the core.

3.3.2 Attractive square well

We next consider a more physical potential, an attractive well:

$$V(r) = -\frac{\hbar^2 k_0^2}{2m}, \quad r < R, \tag{3.43}$$

$V(r) = 0$ otherwise. Like the actual ion-atom potential, this can have bound states for the two-body problem. With this potential we shall be able to examine how solutions of the GP equation disappear as the condensate density increases. The GP equation (3.40) reads

$$\left[-\frac{d^2}{dr^2} - k_0^2\theta(R-r) + 8\pi a_{\mathrm{aa}}\left(\frac{|\chi|^2}{r^2} - n_0\right) \right]\chi = 0, \tag{3.44}$$

where $\chi = r\psi$ and $\theta(x)$ is the step function. The scattering length for this potential is

$$a = R\left(1 - \frac{\tan k_0 R}{k_0 R}\right). \tag{3.45}$$

Since this equation is nonlinear, there can be multiple solutions for the same boundary conditions (i.e. the same bulk density n_0). As we will show in the

following, for small n_0 it has $2\nu_S + 1$ solutions, where ν_S is the number of nodes of the zero-energy solution of the Schrödinger equation ψ_S or, equivalently, the number of bound states of the Schrödinger equation. In the low background density limit, inside the well the solution with the maximum number of nodes approaches ψ_S, i.e. $\psi(r) \propto \sin(k_0 r)/r$, while outside it tends towards the uniform density n_0 with the asymptotic behavior given in Eq. (3.30), $\delta\psi(r) \propto \exp(-k_\xi r)/r$.

With increasing n_0, the mean-field repulsion between the atoms makes the effective potential shallower, which tends to push nodes of the wave function outwards. At the same time, the increase in the chemical potential has the opposite effect on the nodes. What we find is that if the zero-energy solution of the Schrödinger equation has ν_S nodes, for low condensate densities the GP equation has one solution with no nodes, and *two* solutions with any nonzero number of nodes less than or equal to ν_S.

To demonstrate this, we analyze separately the behavior of the wave function inside and outside the well, and match them at some intermediate point, which for this particular potential we take to be the edge of the well. Specifically, we integrate out from the origin, where $\chi = 0$, for different choices of the derivative of χ at $r = 0$ and calculate ψ and ψ' at the boundary $r = R$. These trace a curve in $\psi - \psi'$ space. Then we integrate inwards from large distances, where the solution is defined by the proportionality constant C of the Yukawa asymptotic form, Eq. (3.30). As C is varied, another curve in $\psi - \psi'$ space is traced out. If the mean-field interaction could be neglected for $r < R$, the ratio $\psi'(R)/\psi(R)$ would not depend on the normalization of the wave function, and therefore the curve corresponding to the inner boundary would be a straight line through the origin. In the presence of atom-atom interactions, the ratio ψ'/ψ obtained by integrating outwards traces out a spiral. For low n_0 this crosses the ψ' axis a number of times equal to the number of nodes the zero-energy solution of the Schrödinger equation has inside the potential. This follows from the observation that for low $\chi'(0)$ the solution will have the same number of nodes inside the potential as the zero-energy solution of the Schrödinger equation, while for very large values of $\chi'(0)$ the effects of the mean field will be so strong that the solution has no nodes inside the potential.

The corresponding plot obtained by integrating inwards has two branches, depending on whether $\psi(r \to \infty)$ is positive or negative. Examples of the plots are given in Fig. 3.1 for parameters such that $\nu_S = 3$. For low n_0, there are $2\nu_S + 1$ intersections of the two sets of curves, corresponding to solutions of the GP equation. This is illustrated in Fig. 3.1a. As n_0 increases, pairs of solutions with the same number of nodes merge and disappear, as shown in Fig. 3.1b. Eventually, at sufficiently high values of n_0 only the node-less solution survives.

In Figs. 3.1 and 3.2 we show how, with increasing external density, the solutions with the highest number of nodes actually merge. For densities higher than this critical value, the only solutions are ones with a smaller number of nodes.

Despite its short-range character, we will see in the next Section that the model given above captures the main features of the solutions of the GP equation for the long-ranged atom-ion potential. As we show in Appendix A, a one-dimensional model of an interacting gas in a square well potential, which is appealing because it may be solved analytically, fails even qualitatively to describe the physics of the three-dimensional problem: in particular, states exist
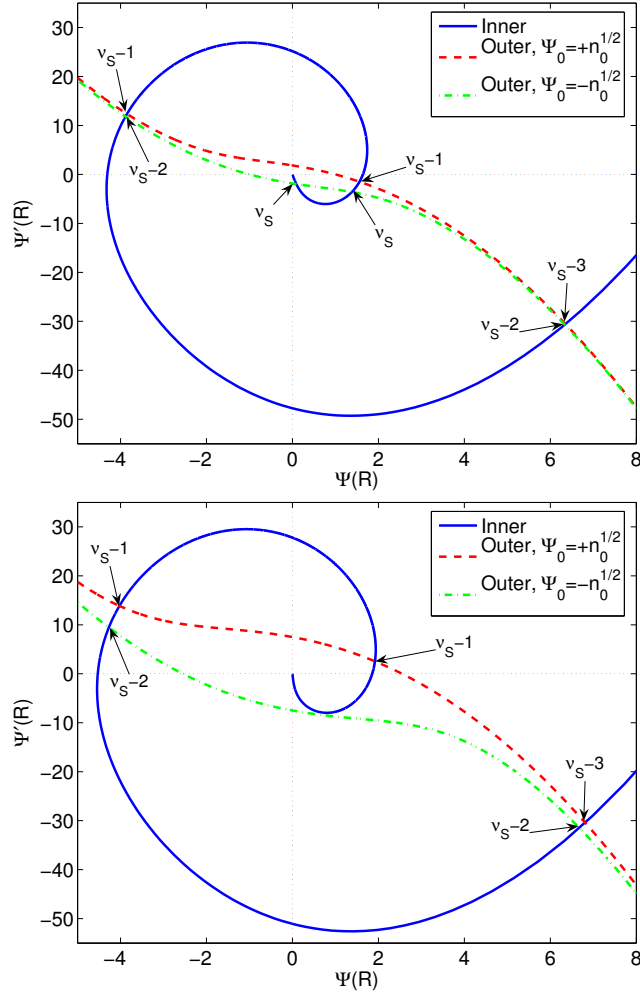
Figure 3.1: Behavior of $\psi(R)$ and $\psi'(R)$ for the solution inside the well (solid line) and outside it (dashed and dot-dashed lines for $\psi(r \to \infty) = \pm\psi_0$, respectively). In the plots we have set $k_0 R = 9$, which gives $\nu_S = 3$ (i.e. three bound states for the Schrödinger equation). We measure energies in units of $\hbar^2 k_0^2/2m$ and lengths in units of R. The calculations were performed for $U_0 = 0.45$ in these units, but results for other values of U_0 may be obtained by scaling, since for a given chemical potential, ψ and ψ' vary as $U_0^{-1/2}$. The symbols near intersections indicate the number of nodes of the solution. The upper panel (a) is for $\mu = 0.45$, and the lower one (b) for $\mu = 2.9$, just above the value $\mu = 2.52$ at which the two solutions with 3 nodes merge and disappear.
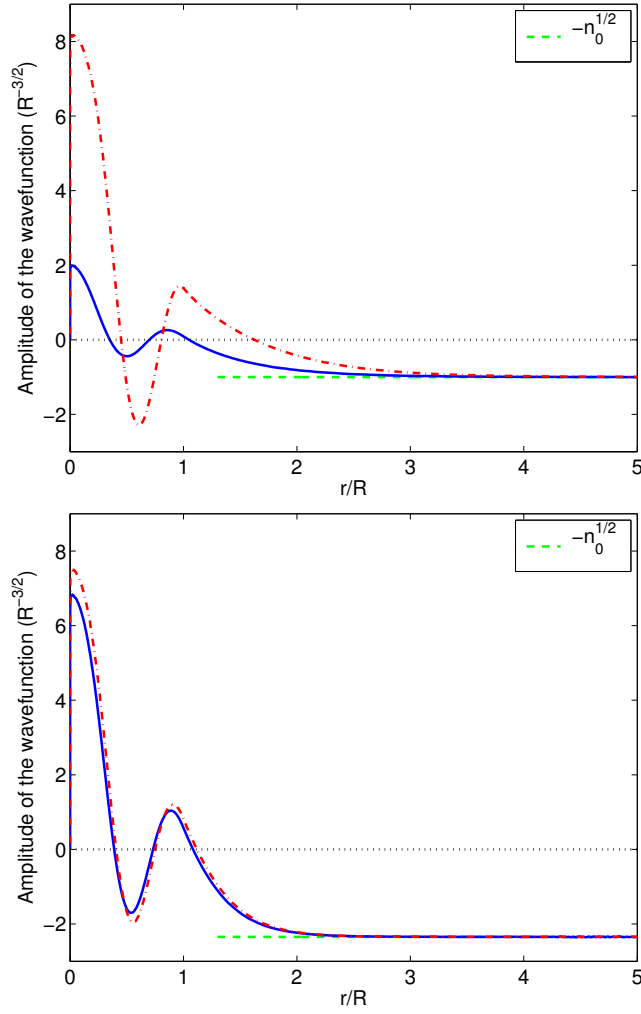
Figure 3.2: Two solutions of the Gross-Pitaevskii equation for the attractive square well potential. $k_0 R$ and U_0 are the same as in Fig. 3.1. For the upper panel, the chemical potential is 0.45, as in Fig. 3.1a, while for the lower one it is 2.5, just below the value at which the solutions merge. The solutions both have three nodes, and are the first to merge as the chemical potential increases.

in one dimension for arbitrarily high asymptotic densities.

3.4 The r^{-4} potential

We now turn to a more realistic potential with the same r^{-4} behavior as the actual atom-ion interaction at large distances. For definiteness, we consider parameters appropriate for a ^{87}Rb condensate, and we take $a_{\mathrm{aa}} = 100a_0$. At large distances, we take the atom-ion potential to be given by Eq. (3.2) with $\tilde{\alpha} = 320a_0^3$. The wave functions are sensitive to the short-range behavior of the potential, but we may obtain illustrative results by cutting the $1/r^4$ potential off by a repulsive hard core of radius R. Since many atoms are bound to the ion, we assume the ion to be static and set $m_{\mathrm{ai}} = m$. The atom-ion scattering length of such potential may be calculated in the WKB approximation, and is given by [49]

$$a_{\mathrm{ai}} = \beta_4 \cot \left[\frac{\beta_4}{R} \right].$$
(3.46)

The number of bound states allowed by the potential can be estimated by increasing the potential strength from zero to its actual value. A bound state appears each time the scattering length diverges, and therefore the number of bound states is given by

$$\nu_{\mathrm{S}} = \mathrm{Int} \left(\frac{\beta_4}{\pi R} \right),$$
(3.47)

where $\mathrm{Int}(x)$ denotes the integer part of x. To model actual atom-ion potentials, a physically reasonable value of R would be $\sim 10a_0$. However, the properties of the wave function of most importance here are those at relatively large distances, $r \gtrsim 10^3 a_0$, so we take $R = 300a_0$, since this should give us the correct physical behavior for the distances of interest. We do not expect the qualitative behavior of the wave function to depend on R, even though quantities like the scattering length do, and we have verified this numerically.

We now describe numerical solutions of the GP equation that approach a constant density n_0 far from the ion. Just as for the finite-range potential considered in the previous Section, there is generally more than one solution for a given value of the chemical potential, and for small external densities one expects $2\nu_{\mathrm{S}} + 1$ solutions. In Fig. 3.3 we show the wave functions corresponding to the two states with the highest number of nodes, namely seven for the parameters chosen, in agreement with the quasi-classical result (3.47). The free energy, for a given condensate density n_0, is highest for the states with the highest number of nodes, and decreases as the number of nodes decreases.

In the absence of inelastic processes, we expect only the uppermost state of the ionic potential to play an important role in the capture process, since it is the only one with an appreciable overlap with the continuum wave function representing the unbound atoms [8].

The excess number of atoms is given in terms of the atomic density distribution by Eq. (3.4) or, alternatively, from the free energy $F = E - \mu N$ by Eq. (3.9). In Fig. 3.5 we show results obtained from our numerical simulations by both methods. In the limit of very low condensate density we get values for ΔN in accord with the thermodynamic arguments in Sec. 3.1. The consistency
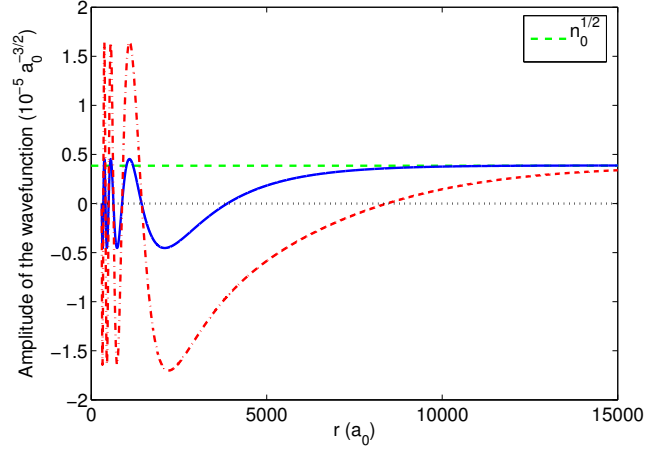
Figure 3.3: Condensate wave functions for the two uppermost states in the $1/r^4$ potential with the parameters given in the text for $n_0 = 10^{14}\text{cm}^{-3}$. Both states have seven nodes, but the resolution of the figure is inadequate to exhibit the rapid oscillations for r close to R. The state that, in the dilute limit, becomes the zero-energy solution of the Schrödinger equation is given by the solid line.
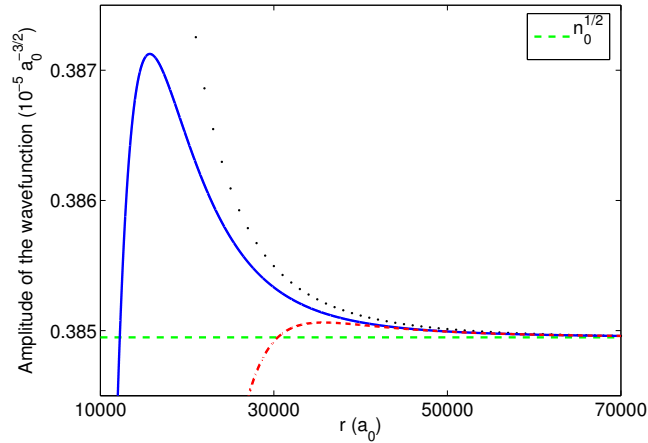

Figure 3.4: Large-r behavior of the condensate wave function for the same parameters as in Fig. 3.3: the dotted line is the TF approximation (3.33), which approaches its asymptotic value as $1/r^{-4}$.
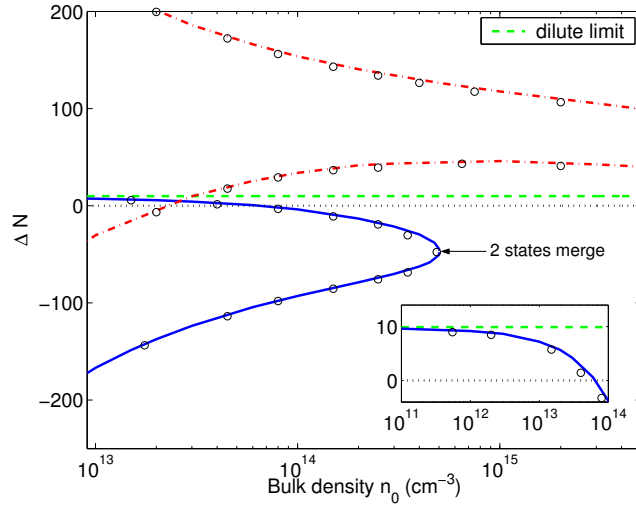
Figure 3.5: Excess number of atoms around a single ion as a function of the bulk density. The dashed line is the dilute limit appropriate for a fixed ion, $\Delta N = -a_{\mathrm{ai}}/2a_{\mathrm{aa}}$ ($R = 300a_0$ gives $a_{\mathrm{ai}} \approx -1980a_0$ for an infinitely massive ion). Results are shown for the four uppermost levels for this potential (i.e. the two with 7 nodes and the two with 6 nodes, indicated respectively by the solid and dot-dashed lines). The lines are obtained from Eq. (3.4), the circles from Eq. (3.9). The inset exhibits the behavior at lower densities.
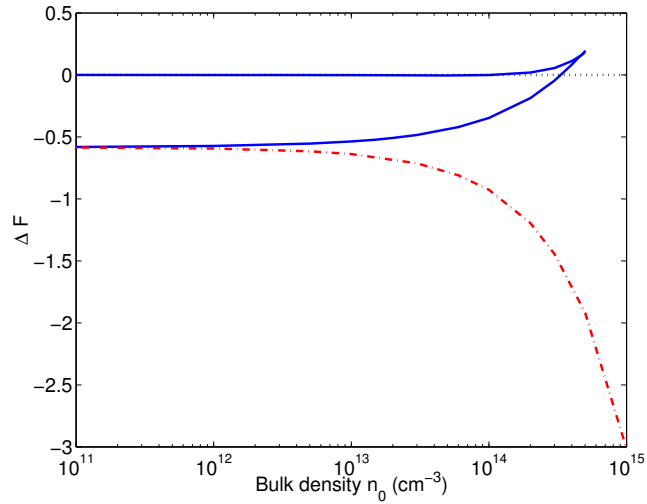

Figure 3.6: Difference in free energy for the states given in the previous figure: the solid lines are for the two states with 7 nodes and the dot-dashed line for one of the states with 6 nodes. The free energy is measured in units of $10^{-5}\hbar^2/ma_0^2$. The other state with 6 nodes lies much lower, at around $\Delta F \approx -3 \cdot 10^{-4}\hbar^2/ma_0^2$.

of the two methods of calculation has been confirmed for core radii that give scattering lengths in the range $|a_{\mathrm{ai}}| < 5000a_0$.

The figure shows that the excess numbers of atoms for two states with the same number of nodes become equal at the density above which the solutions no longer exist. This is to be expected, since the solutions become identical at this point. At the critical density we find $\beta_4^2/\xi^2 \approx 1$, in accord with the quasi-classical argument presented at the end of Sec. 3.1.

In the detailed calculations described so far we have focused attention on states with close to the maximum number of nodes. In particular, in the low-density limit and in the absence of inelastic processes that can cause the system to relax, one would expect the state of the condensate to be the one that close to the ion resembles the zero-energy solution of the Schrödinger equation. However, three-body processes can relax the system, thereby populating states with lower numbers of nodes. To calculate properties of such a system, one could start with a many-particle wave function of the Hartree-Fock type in which more than one single-particle state is occupied, and solve the Hartree-Fock equations. This is, however, beyond the scope of the present study because the density of atoms rises to values sufficiently high that the dilute gas approximation for the interaction energy employed in the GP approach fails at relatively large distances from the ion. To see this, we note that the states with small number of nodes are characterized by high overall densities and are well described by the Thomas-Fermi approximation, Eq. (3.32), down to very small distances from the core. The dilute gas approximation is valid provided $n|a_{\mathrm{aa}}|^3 \ll 1$, i.e. when

$$n|a_{\mathrm{aa}}|^3 \approx \left| \frac{V(r)}{2U_0} a_{\mathrm{aa}}^3 \right| = \frac{\beta_4^2 a_{\mathrm{aa}}^2}{16\pi r^4} \ll 1 \qquad (3.48)$$

or

$$r \gg (\beta_4|a_{\mathrm{aa}}|)^{1/2}/3, \qquad (3.49)$$

which for rubidium ($a_{\mathrm{aa}} \approx 100a_0$) implies that the GP equation is valid only for $r \gg 300a_0$ for such states.

3.4.1 Comparison with earlier work

In their paper, Côté *et al.* [8] looked at bound solutions to the GP equation, and argued that the binding energy of the atoms trapped by the ion is proportional to $N^{-2/3}$, with N being the number of neutral atoms trapped by the ion. This would imply the possibility to trap an infinite number of atoms in the absence of other effects such as thermal fluctuations. In the following we sketch their argument [50]. Let $E_0 = -\hbar^2/2ma_{\mathrm{ai}}^2$ be the energy of the last loosely bound state of a single atom in the potential created by a single static ion. The state has a characteristic spatial extension a_{ai}. When N atoms with repulsive interaction ($a_{\mathrm{aa}} > 0$) populate the same one-particle state, they will sit in an equilibrium configuration each at a distance $a_N \gg a_{\mathrm{ai}}$ from the ion. In a mean field calculation, the energy might be written as

$$E_N = E_0 + \frac{N U_{\mathrm{aa}}}{\frac{4}{3}\pi a_N^3}, \qquad (3.50)$$

where U_{aa} was defined in (3.12). If $E_N \ll E_0$, comparing the latter equation with the rough estimate $E_N = -\hbar^2/2ma_N^2$ one obtains

$$\frac{E_N}{E_0} = \left(\frac{a_{\mathrm{ai}}}{a_N}\right)^2 = \left(\frac{a_{\mathrm{ai}}}{6Na_{\mathrm{aa}}}\right)^{2/3}. \tag{3.51}$$

Although we are solving a different problem and we are not in the position to do a quantitative comparison with this result, our model predicts at low density a divergence of the number of trapped atoms for every state that in the dilute limit reduces to a bound state of the non-interacting problem (i.e. for every state except the one that stems out of the zero-energy Schrödinger solution, see Fig. 3.5). We observe in our simulations that, as the bulk density approaches zero, ΔN diverges for these states since their spatial extension increases indefinitely. This is in qualitative accord with the prediction of Côté *et al.*, that has been worked out to describe the uppermost bound state.

Nonetheless, at low condensate densities and in the absence of relaxation processes, the system will occupy the state that more closely resembles the zero-energy solution of the Schrödinger equation and not one of the bound states of the ionic potential. Consequently, the number of trapped atoms will be finite and given by the dilute limit result, Eq. (3.13).

3.5   Conclusions and discussion

In this Chapter we have calculated the excess number of condensate atoms collected by the polarization potential of a single ion. We find that at low bulk density it can be either positive or negative, depending on the sign of the atom-ion phase shift, and a typical magnitude is of order $10 - 100$. A typical spatial extension of this density disturbance is set by the length scale associated with the ionic potential, $\beta_4 \sim 1\ \mu$m. Our estimates indicate that the Gross-Pitaevskii equation gives a reliable description for the continuum wave function that in the dilute limit approaches ψ_{S}, the zero-energy Schrödinger solution. For states with fewer nodes, the GP equation may not be appropriate since the density of atoms around the ion may grow substantially.

We have analyzed the Gross-Pitaevskii equation for a Bose-Einstein condensate in the presence of an ion as a function of the asymptotic density, and characterized its asymptotic behavior. We find that for sufficiently low condensate densities the non-linear problem admits $2\nu_{\mathrm{S}} + 1$ different solutions, where ν_{S} is the number of bound states of the linear (Schrödinger) equation. With increasing condensate density, pairs of states become degenerate and disappear, and the state of the system must change discontinuously. An interesting challenge is to find experimental evidence for such a behavior.

There are many open problems in this relatively unexplored field. In most of the calculations we have assumed that the state of interest is the one with the maximum possible number of nodes. More study is needed of inelastic processes that will cause atoms to relax to lower states [8]. It would also be interesting to obtain insight into the equilibrium properties of these ion-atoms compounds when formed inside a trapped gas (i.e. whether these localize in the center of the cloud or are pushed to the surface by buoyancy). The calculation of the effective mass of the dressed ion would finally provide important information on its dynamics.
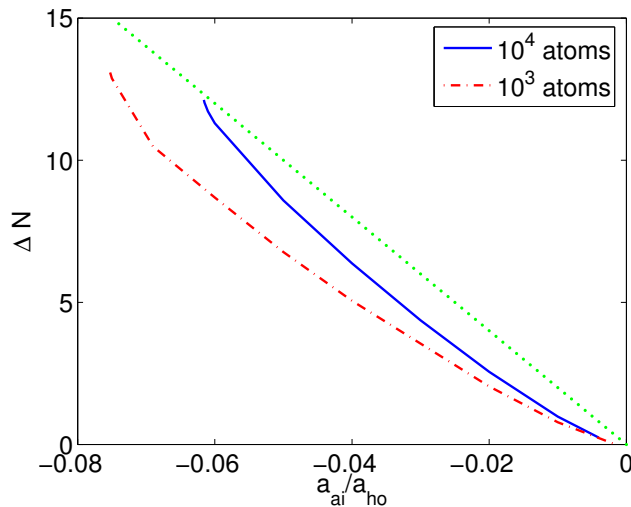
Figure 3.7: Excess number of atoms ΔN around a single impurity, calculated from Eq. (3.52) using self-consistent mean-field solutions for a single impurity and two different numbers of trapped atoms as a function of the atom-impurity scattering length a_{ai} ($a_{\mathrm{aa}} = 0.005a_{\mathrm{ho}}$, $m_a = m_i$ and $r_c = a_{\mathrm{ho}}$). The dotted line shows the analytical estimate for a homogeneous gas, Eq. (3.13). The cloud is expected to collapse if $a_{\mathrm{ai}} < -0.062a_{\mathrm{ho}}$ for a cloud of 10^4 atoms, and if $a_{\mathrm{ai}} < -0.075a_{\mathrm{ho}}$ for 10^3. Image courtesy of D. Blume and R. Kalas.

It is interesting to note here that in a subsequent work Kalas and Blume [51] have analyzed the possibility of localizing an impurity inside a trapped cloud. By means of a mean-field model with contact atom-impurity potential, they show that tuning the atom-impurity scattering length a_{ai} from 0 to a large negative value the impurity first gets localized inside the trapped condensate, and finally can even cause the collapse of the condensate. From the density profile of the atomic wave function they also calculate the excess number of atoms around the impurity. Since they fix the number of atoms and not the chemical potential, they define the excess number of atoms as

$$\Delta N = 4\pi \int_0^{r_c} dr \; r^2 \left[n(r) - n_0(r) \right] \tag{3.52}$$

where n is the density of the trapped condensate in the presence of the impurity, n_0 the density in its absence and r_c is an arbitrary cut-off radius (r_c needs to be finite since, with fixed N, $\Delta N = 0$ if $r_c \to \infty$). Their findings are in good agreement with our analytical result for a homogeneous gas (see Fig. 3.7), and should converge to it with increasing number of condensed atoms.

Experimental studies will be valuable in providing guidance for future work, and new investigations of condensate photoionization may soon start in the cold atoms group in Pisa [7]. On the experimental side, particular care should be taken in order to ensure sufficient observation times. In the experiment performed by Ciampini *et al.* [6], the ions were produced with a pulsed photoionization laser detuned above threshold by typically $\Delta E/h \approx 100\mathrm{GHz}$. Re-

membering that the mass m_e of the electron is much smaller than the mass of the ion m_i, the electron acquires a velocity of order

$$v_e = \sqrt{\frac{2\Delta E}{m_e}} \approx 10^4 \text{m/s}. \tag{3.53}$$

Assuming that the ion is "dressed" by a cloud of ~ 50 atoms, it would recoil in the opposite direction with

$$v_i = \frac{1}{50} \frac{m_e}{m_i} v_e \approx 2 \times 10^{-3} \text{m/s}. \tag{3.54}$$

For a typical condensate size of 5μm, this would result in a transit time of about 0.5ns for the electron and 2.5ms for the ion. The pulsed laser might be replaced by a continuous one, allowing for a much smaller detuning from the atomic threshold, $\Delta E/h \approx 1$MHz, and smaller dissociation kinetic energies. Electric stray fields are nonetheless normally present inside the vacuum chamber, and might drastically shorten the observation times independently of the initial speed: a typical field of 1V/cm applied to an ion initially at rest would already limit its transit time to 300ns. Careful control of electric stray fields down to the present "state of the art" limit of about 1mV/cm could increase the interaction time to about 10μs, a time scale that is still relatively short compared to typical observation times.

A very interesting proposition [52] is the possibility of replacing ions with Rydberg atoms, i.e. atomic states characterized by large principal quantum numbers $\mathfrak{n}$ ($40 \lesssim \mathfrak{n} \lesssim 80$). An alkali atom in such a state is electrically neutral and therefore it is not accelerated by the stray fields present in the cavity, but characterized by a huge dipole moment, $d \approx ea_o\mathfrak{n}^2$, since its valence electron sits on a quasi-classical, circular trajectory with very large radius. With careful excitation of a condensate, a small number of atoms could be promoted to a definite Rydberg state, and an external constant field could easily keep each dipole aligned for times long enough to allow the formation and observation of structures similar to the ones discussed in this Chapter.

We may try to estimate of the excess number of atoms around a Rydberg atom along the same lines of reasoning that led to Eq. (3.16). A single Rydberg atom creates in the far field $r \gg d/e$ an electrostatic field $\mathcal{E}_{\text{es}} = d/4\pi\varepsilon_0 r^3$ (we neglect for simplicity the $l = 2$ angular dependence) and gives an energy shift equal to

$$V(r) = -\tilde{\alpha} \frac{e_0^2 a_0^2 \mathfrak{n}^4}{2r^6}. \tag{3.55}$$

Equating potential and kinetic energies allows to find a characteristic length β_{Rydb},

$$\beta_{\text{Rydb}} = a_0 \mathfrak{n} \left(\frac{\tilde{\alpha}}{a_0^3} \frac{m}{m_e} \right)^{1/4}. \tag{3.56}$$

By analogy with Eq. (3.16), we would estimate the excess number of atoms trapped by the Rydberg atom to be roughly given by

$$|\Delta N| \sim \frac{\beta_{\text{Rydb}}}{\beta_6} \sim \mathfrak{n} \left(\frac{\tilde{\alpha}}{2a_0^3 C_6} \right)^{1/4}, \tag{3.57}$$

that yields $|\Delta N| \sim \mathfrak{n}/2$ in the case of rubidium. Since principal quantum numbers as high as $\mathfrak{n} = 80$ can be reasonably obtained, the present argument would imply that these structures may have sizes similar to the ones generated by static ions. Nonetheless, the characteristic length β_{Rydb} is comparable to the dipole moment $d \approx ea_o\mathfrak{n}^2$ and therefore the result given by Eq. (3.57) does not appear reliable, since it makes use of the potential (3.55) at distances outside its range of validity. A more accurate estimate should take into account the fact that at distances $r \lesssim d/e$ the dipole potential flattens, i.e. $V(r) \sim 1/(r + R)^6$ where R is a suitable cutoff of order the size of the dipole, d/e. The deeper understanding of the problem would involve the solution of the GP equation in the presence of a dipole potential, which is characterized by an $l = 2$ angular symmetry.

Experiments in this direction are planned in the close future by the Stuttgart group [52] and will surely provide useful insights into this new and exciting field.

Chapter 4

Collective oscillations in trapped interacting Fermi gases

In a trapped two-component Fermi gas in its normal state, collisions are predicted to be rare at both low and high temperatures. When $T \ll T_F$ the Fermi sphere is completely filled and collisions are suppressed due to the lack of available final states (so-called Fermi blocking). In the high temperature limit $T \gg T_F$, two-body encounters become exceedingly rare since the density of the gas drops like $T^{-3/2}$. In both these conditions the gas is what is referred to as in the collisionless regime. When weakly perturbed from its equilibrium position the trapped cloud undergoes collective oscillations whose frequencies are sums of integer multiples of the trap frequencies.

Very high gas densities, or strong interactions such as the ones induced by Feshbach resonances, may change this picture and allow for (classic) hydrodynamic effects in the intermediate regime where $T \approx T_F$. In addition, two-component Fermi gases in the cross over regime are predicted to become superfluid when $T \lesssim 0.3 T_F$, and in this case the dynamics has to be described by superfluid hydrodynamics. Gases under deep hydrodynamic conditions also perform undamped oscillations, but at definite frequencies that are somewhat smaller than the ones found in the collisionless regime. A careful and systematic study of the low-energy spectrum can give important informations on the dynamics and typical collision times in the gas.

Our motivation for the work presented in this Chapter was triggered by the publication of measurements characterizing the collective excitation modes of strongly-interacting ⁶Li atoms in a cigar-shaped trap as a function of interaction strength and temperature [18, 19]. In the weak confinement direction, the measured frequencies for the axial (quadrupole) mode are very close to the hydrodynamic value, in agreement with theoretical predictions. By contrast, the results for the breathing mode in the tightly confined radial plane are somewhat surprising: the measured frequencies agree with the expression for the hydrodynamic limit even though it is predicted that the typical collision times should not allow the system to reach local thermodynamic equilibrium in the period of a single oscillation (as we will see in the following, this is a necessary condition

to observe hydrodynamic behavior).

In order to come closer to the solution of this puzzle, we investigate in the following the problem of finding the frequency and attenuation of low-energy collective modes in an interacting trapped two-component Fermi gas as a function of temperature and interaction strength. We show indeed that, under the experimental conditions reported in [18, 19], the gas performing radial shape oscillations should never be able to enter the deep hydrodynamic regime, even in the case of unitarity limited interaction $(k_F|a|)^{-1} \ll 1$, and should lie at most in an intermediate region between the collisionless and hydrodynamic limits.

The detailed plan of the Chapter is as follows.

In the next Section we briefly recall the derivation of the collective-mode spectrum for a non-interacting gas in both the collisionless and hydrodynamic regimes. This has the sole purpose of introducing the reader to the topic: the material contained therein is not original and can be found in standard textbooks and reviews [53, 54, 4].

In Sec. 4.2 we first introduce the viscosity and viscous relaxation rate of a gas through the linearization of the Boltzmann equation and show how their asymptotic behavior at high and low temperatures is influenced by interactions in both the uniform and trapped cases, respectively in Secs. 4.2.1 and 4.2.2. Interactions effects are included in the collision integral via an energy-dependent cross sections, and their importance is evidenced in Sec. 4.2.3, where we compare the viscous relaxation rate predicted by our model with a calculation by Vichi based on an energy-independent cross section [55].

We show in Sec. 4.3 how the linearized Boltzmann equation can be improved to include an additional streaming term describing mean field interaction effects.

In Sec. 4.4 we solve the kinetic equation by a variational method, and extract the frequency and damping of the low-energy spectrum as a function of temperature and strength of the interactions in the case of an axially symmetric trap. The derivation contains a number of technical steps, that are described in Appendix B. We compare our results in Sec. 4.4.1 with those of a model by Pedri *et al.* [56], finding complete agreement in the range of validity of both theories regarding the predicted shifts due to interaction effects. Our work extends the latter by explicitly calculating the viscous relaxation rate and the importance of mean field effects as a function of temperature, thereby allowing for a direct comparison with current experiments.

The concluding Sec. 4.5 summarizes our main results and reviews the limit of validity of our theory and its possible extensions.

4.1   Collisionless and hydrodynamic limits

The behavior of a trapped gas can be described exactly in the two extreme limits of rare and frequent collisions. For definiteness, we will consider a gas of particles with mass m in a (generally anisotropic) harmonic trap,

$$V(\mathbf{r}) = \frac{m}{2}(\omega_x^2 x^2 + \omega_y^2 y^2 + \omega_z^2 z^2). \qquad (4.1)$$

In the absence of collisions, the atoms are free particles: their motion in the three orthogonal directions is decoupled, and they perform undamped oscillations in the trap with frequencies that are sums of integer multiples of the trap

frequencies ω_i,

$$\omega = \sum_{i=x,y,z} \nu_i \omega_i. \tag{4.2}$$

In the opposite limit of frequent collisions, each infinitesimal volume of the cloud can be considered to be in local thermodynamic equilibrium and the evolution is described by classical hydrodynamic theory. A typical collision rate $1/\tau$ is given by

$$\frac{1}{\tau} \sim \frac{\bar{v}}{l} \tag{4.3}$$

where $\bar{v}$ is the average particle velocity and $l = 1/n\sigma$ is the mean free path between collisions, n being the density and σ the total scattering cross section. Thermalization is ensured if each atom experiences many collisions during a single oscillation, i.e. if the collision rate is larger than the trap frequency:

$$\omega\tau \ll 1. \tag{4.4}$$

Another condition that needs to be satisfied is that the mean free path l should be small compared to the wavelength of the mode λ. The wavelength of a collective mode is restricted to be smaller than the size of the trapped cloud R (while perturbations with longer wavelengths are sound waves), and the second necessary condition for the validity of the hydrodynamic picture can be formulated as

$$l \ll \lambda \lesssim R. \tag{4.5}$$

In classical hydrodynamics the fluid is described as a continuous medium whose motion is completely determined in terms of five variables, the three components of the fluid velocity $\mathbf{u}$ and any two thermodynamic quantities, that can be taken as the density n and the pressure p. The density and the velocity are connected by the continuity equation

$$\frac{\partial n}{\partial t} + \nabla \cdot (n\mathbf{u}) = 0. \tag{4.6}$$

In an ideal fluid, no heat transfer occurs between different (moving) infinitesimal volumes of the fluid and the entropy is conserved locally. The other four equations necessary to close the description of the system can be taken as the three components of the Euler equation

$$\frac{\partial \mathbf{u}}{\partial t} + (\mathbf{u} \cdot \nabla)\mathbf{u} + \frac{\nabla p}{mn} = \mathbf{f}, \tag{4.7}$$

which reflects momentum conservation, and the adiabatic equation describing the conservation of entropy,

$$\frac{\mathrm{d}s}{\mathrm{d}t} = \frac{\partial s}{\partial t} + \dot{\mathbf{r}} \cdot \nabla s = 0. \tag{4.8}$$

In the above formulae, s is the entropy per particle and $\mathbf{f} = -\nabla V/m$ is the force per unit mass[1].

---

[1]In the case of non-ideal (viscous) fluids, the above equations are substituted respectively by the three components of the Navier-Stokes equation and by an expression describing the rate of conversion of mechanical energy into entropy.

Linearization of Eqs. (4.6) and (4.7) for an ideal gas obeying (under adiabatic condition) a generic equation of state $p \propto n^\gamma$ leads to the following relation [4],

$$\frac{\partial^2 \mathbf{u}}{\partial t^2} = \gamma \frac{p_{\text{eq}}}{n_{\text{eq}}} \nabla (\nabla \cdot \mathbf{u}) + \nabla (\mathbf{f} \cdot \mathbf{u}) + (\gamma - 1) \mathbf{f} (\nabla \cdot \mathbf{u}), \qquad (4.9)$$

which describes the velocity field $\mathbf{u}$ of a gas subject to the force $\mathbf{f}$. This equation can be employed to extract the frequencies of low-energy hydrodynamic modes for a harmonically trapped gas. To describe the simplest normal modes, we introduce the Ansatz

$$\mathbf{u} = (ax, by, cz)e^{-i\omega t}, \qquad (4.10)$$

which corresponds to an anisotropic homologous "breathing" of the cloud. Its divergence is constant in coordinate space, and inserting our Ansatz into (4.9) we obtain

$$-\omega^2 \mathbf{u} = \nabla (\mathbf{f} \cdot \mathbf{u}) + (\gamma - 1) \mathbf{f} (\nabla \cdot \mathbf{u}). \qquad (4.11)$$

Due to the linear character of both the force $\mathbf{f} = -(\omega_x^2 x, \omega_y^2 y, \omega_z^2 z)$ and the velocity field $\mathbf{u}$, only linear terms appear in Eq. (4.11), and the oscillation frequencies are given by the roots of the determinant of the homogeneous linear system for a, b and c.

For a monoatomic gas in the classical regime under adiabatic conditions $p \propto n^{5/3}$, and in a generic cylindrically symmetric trap with $\omega_x = \omega_y = \omega_\perp$ and $\omega_z = \lambda \omega_\perp$ one finds the three roots

$$\omega^2 = 2\omega_\perp^2 \qquad (4.12)$$

$$\omega_\pm^2 = \frac{\omega_\perp^2}{3} \left(5 + 4\lambda^2 \pm \sqrt{25 - 32\lambda^2 + 16\lambda^4} \right). \qquad (4.13)$$

The first root is associated with the $m = 2$ radial quadrupole mode $a = -b, c = 0$, and is independent of the trap anisotropy λ since it involves no motion in the z direction.

The other two frequencies are two $m = 0$ modes. In the spherically symmetric case ($\lambda = 1$) they are

$$\omega_+^2 = 4\omega_\perp^2 \quad \text{and} \quad \omega_-^2 = 2\omega_\perp^2, \qquad (4.14)$$

representing the monopole (spherically symmetric, $a = b = c$) and quadrupole modes ($a = b = -c/2$). In the highly elongated limit ($\lambda \ll 1$) they become

$$\omega_+^2 = \frac{10}{3}\omega_\perp^2 \quad \text{and} \quad \omega_-^2 = \frac{12}{5}\omega_z^2, \qquad (4.15)$$

and are associated with the breathing mode ($a = b = 5c/2$) and the quadrupole mode ($a = b = -\lambda^2 c/2$).

The procedure described above can also be employed to extract the eigenfrequencies of a Bose-Einstein condensed cloud at $T = 0$ when the number of particles is sufficiently large that the quantum pressure term in the superfluid hydrodynamic equation can be neglected, i.e. when the wavelength of the mode is larger than the coherence length. Under this assumption the motion of a condensate is described by an equation which is identical to its classical counterpart (4.9) but requires the additional condition that the velocity field should

be irrotational, $\nabla \times \mathbf{u} = 0$. The Ansatz (4.10) satisfies this property, and the derivation of the frequencies proceeds along the same lines, the only difference being that in the case of a dilute BEC the equation of state is $p \propto n^2$.

Hydrodynamic theory in trapped gases must be applied with caution. As already mentioned local thermodynamic equilibrium is ensured only by frequent collisions, and this in turn requires a high density of particles. As a consequence hydrodynamics never applies to the outer parts of trapped clouds, where the density drops to zero and the mean free path becomes very large: quantities like the averaged damping rate can be calculated from viscous hydrodynamics only introducing a suitable length scale to cutoff the spatial average [57]. In addition, for typical experimental parameters at temperatures at which the effects of quantum degeneracy become appreciable, the conditions for hydrodynamic behavior require that clouds should contain at least $10^6 - 10^8$ particles. Consequently, fully hydrodynamic conditions were not realized in early experiments on cold bosons in the classical regime. These systems were in an intermediate regime, characterized by $\omega\tau \approx 1$, and the frequency and damping of their collective modes has been the subject of numerous investigations [57, 58, 59, 60, 61, 62]. The situation changed drastically with the new generation of experiments realized with fermions: suddenly Feshbach resonances allowed the strongly interacting regime $k_F|a| \gg 1$ to be achieved, while Pauli principle limited three-body losses and allowed for long-lived clouds. In the next Section we shall calculate the characteristic relaxation rate for an interacting gas of fermions, analyzing both the uniform and trapped cases. The average relaxation rate $1/\tau$ will then be used in Sec. 4.3 to obtain the frequency and damping of the oscillations from a variational solution of the Boltzmann equation.

4.2   Viscous relaxation time

We shall consider a two-component Fermi gas of atoms with mass m (the same for both components) in its normal phase with equal populations in the two components. The gas may be uniform or trapped in a potential $V(\mathbf{r})$. Since we are dealing with dynamics for which the two components of the gas move in phase, we only need to introduce one distribution function referring to a definite set of internal quantum numbers, and $f = f_\uparrow = f_\downarrow$ (for brevity we have denoted the two sets by $\uparrow$ and $\downarrow$). We assume that the dynamics is described by a semi-classical distribution function $f(\mathbf{r}, \mathbf{p}, t)$ which satisfies the Boltzmann equation [63]

$$\frac{\partial f}{\partial t} + \dot{\mathbf{r}} \cdot \frac{\partial f}{\partial \mathbf{r}} + \dot{\mathbf{p}} \cdot \frac{\partial f}{\partial \mathbf{p}} = -I[f], \qquad (4.16)$$

where $\mathbf{r}$ and $\mathbf{p}$ evolve according to the Hamilton equations of motion,

$$\dot{\mathbf{r}} = \mathbf{v} = \frac{\mathbf{p}}{m}; \quad \dot{\mathbf{p}} = -\frac{\partial V}{\partial \mathbf{r}}, \qquad (4.17)$$

and I is the collision integral,

$$I[f] = \int \frac{d\mathbf{p}_1}{(2\pi\hbar)^3} \int d\Omega \frac{d\sigma}{d\Omega} |\mathbf{v} - \mathbf{v}_1| \left[f f_1(1 - f')(1 - f_1') - (1 - f)(1 - f_1) f' f_1' \right].$$
$$(4.18)$$

In the above expression, Ω is the solid angle for the direction of the relative momentum $\mathbf{p}'_r = (\mathbf{p}' - \mathbf{p}'_1)/2$ after the collision with respect to the relative momentum $\mathbf{p}_r = (\mathbf{p} - \mathbf{p}_1)/2$ before the collision. The first factor inside the square bracket describes the collision of two $\uparrow$ and $\downarrow$ fermions with initial momenta $\mathbf{p}$ and $\mathbf{p}_1$ scattering into states with momenta $\mathbf{p}'$ and $\mathbf{p}'_1$, while the second term refers to the opposite process. Since we consider s-wave scattering, the interactions only involve particles in different internal states and will be described by the energy-dependent scattering cross section for distinguishable particles derived in Eq. (2.33),

$$\frac{\mathrm{d}\sigma}{\mathrm{d}\Omega} = \frac{a^2}{1 + (p_r/\hbar)^2 a^2}. \tag{4.19}$$

In the present Section the streaming terms on the left hand side of (4.16) do not contain any effects of the interaction, but in the following Sec. 4.3 we shall add these as a mean field in the equations of motion (4.17).

The viscous relaxation time, which plays an important part in the following, is defined in terms of the viscosity. Let us briefly recall how one determines the viscosity by linearizing the kinetic equation. To describe small deviations from equilibrium, we write

$$f(\mathbf{r}, \mathbf{p}, t) = f^0(\mathbf{r}, \mathbf{p}) + \delta f(\mathbf{r}, \mathbf{p}, t). \tag{4.20}$$

In equilibrium the collision integral vanishes since $f^0 f_1^0 (1 - f^{0\prime})(1 - f_1^{0\prime}) = \left(1 - f^0\right)\left(1 - f_1^0\right) f^{0\prime} f_1^{0\prime}$ due to energy conservation. The linearization of Eq. (4.16) yields

$$\frac{\partial \delta f}{\partial t} + \frac{\mathbf{p}}{m} \cdot \frac{\partial \delta f}{\partial \mathbf{r}} - \frac{\partial V}{\partial \mathbf{r}} \cdot \frac{\partial \delta f}{\partial \mathbf{p}} = -I[\Phi], \tag{4.21}$$

where the linearized collision integral reads

$$I[\Phi] = \int \frac{\mathrm{d}\mathbf{p}_1}{(2\pi\hbar)^3} \int d\Omega \frac{\mathrm{d}\sigma}{\mathrm{d}\Omega} |\mathbf{v} - \mathbf{v}_1| [\Phi + \Phi_1 - \Phi' - \Phi'_1] f^0 f_1^0 (1 - f^{0\prime})(1 - f_1^{0\prime}), \tag{4.22}$$

and $\Phi = \delta f / \left[f^0 (1 - f^0)\right]$. Collisions conserve the number of particles, momentum and total energy: these constraints imply that the collision integral vanishes when Φ is a function of the form

$$\Phi(\mathbf{r}, \mathbf{p}) = a(\mathbf{r}) + \mathbf{b}(\mathbf{r}) \cdot \mathbf{p} + c(\mathbf{r})p^2, \tag{4.23}$$

since this ensures that $\Phi + \Phi_1 = \Phi' + \Phi'_1$: any function of the form above is called a *collisional invariant*. The distribution function describing a gas of fermions in equilibrium in a frame moving with velocity $\mathbf{u}$ is given by

$$f_{\mathbf{u}}(\mathbf{r}, \mathbf{p}) = \frac{1}{\mathrm{e}^{(p^2/2m + V - \mathbf{u}\cdot\mathbf{p} - \mu)/kT} + 1}, \tag{4.24}$$

and the change in f for small velocities $\mathbf{u}$ and small changes of μ and T is

$$\delta f = \frac{f^0(1 - f^0)}{kT} \left[\mathbf{u} \cdot \mathbf{p} + \delta\mu + \left(\frac{p^2}{2m} + V - \mu\right)\frac{\delta T}{T}\right], \tag{4.25}$$

where $f^0 = f_{\mathbf{u}=0}$. The corresponding Φ is a collisional invariant, in accord with the fact that $f_{\mathbf{u}}$ is an equilibrium function, i.e. a stationary solution of the Boltzmann equation.

We calculate in the following the viscosity in a uniform system, and for simplicity we take the direction of the flow velocity as our x-axis and assume that it varies in the y-direction, $\mathbf{u} = (u_x(y), 0, 0)$. The shear viscosity η relates the momentum current density Π_{xy}, given by

$$\Pi_{xy} = 2 \int \frac{d\mathbf{p}}{(2\pi\hbar)^3} v_y p_x f, \tag{4.26}$$

to the gradient of the flow velocity according to $\Pi_{xy} = -\eta \partial u_x / \partial y$. The factor of two appearing on the right hand side of (4.26) arises from summing over the contributions of the two components ($\uparrow$ and $\downarrow$).

Under stationary conditions (4.21) becomes

$$\frac{\mathbf{p}}{m} \cdot \frac{\partial \delta f}{\partial \mathbf{r}} = \frac{p_y}{m} \left(\frac{\partial u_x}{\partial y} p_x \right) \frac{f^0(1 - f^0)}{kT} = -I[\delta f]. \tag{4.27}$$

In order to establish the concept of a viscous relaxation time let us make a relaxation time approximation to the collision integral with a relaxation time τ_η, which is so far an unknown quantity,

$$I[\delta f] \approx \frac{\delta f}{\tau_\eta}. \tag{4.28}$$

The collision integral (4.28) together with (4.27) and (4.26) yields the viscosity

$$\eta = 2\tau_\eta \int \frac{d\mathbf{p}}{(2\pi\hbar)^3} \left(\frac{p_x p_y}{m} \right)^2 \frac{f^0(1 - f^0)}{kT}. \tag{4.29}$$

Introducing the scalar product

$$\langle A, B \rangle_{\mathbf{p}} = \int \frac{d\mathbf{p}}{(2\pi\hbar)^3} AB f^0(1 - f^0) \tag{4.30}$$

and the notation $X = p_x p_y / m$, we may rewrite Eq. (4.29) in the compact form

$$\eta \equiv \frac{2\tau_\eta}{kT} \langle X, X \rangle_{\mathbf{p}}, \tag{4.31}$$

that we will use as a *definition* for the relaxation time τ_η in terms of the viscosity, also when we will calculate it using the full collisional integral.

We want now to evaluate the ratio between the viscosity and the total particle density of the two components,

$$n_{\text{tot}} = 2 \int \frac{d\mathbf{p}}{(2\pi\hbar)^3} f^0. \tag{4.32}$$

The angular integration in momentum space yields a factor of $1/15$, and the result can be written in the form

$$\frac{\eta}{n_{\text{tot}}} = \frac{2}{5} \tau_\eta \frac{\int_0^\infty \epsilon^{5/2} f^0(1 - f^0) d\epsilon}{\int_0^\infty \epsilon^{3/2} f^0(1 - f^0) d\epsilon}. \tag{4.33}$$

Analytic expressions for the integrals occurring in (4.33) may be obtained when kT is either small or large compared to the Fermi energy $\epsilon_F = \hbar^2 k_F^2 / 2m$, where

the magnitude of the Fermi wave vector k_F is given by $k_F^3 = 3\pi^2 n_{tot}$. When the temperature is much larger than the Fermi temperature $T_F = \epsilon_F/k$, the equilibrium distribution function is $f^0 \simeq \exp[(\mu - \epsilon)/kT]$, with μ being the chemical potential, and (4.33) becomes

$$\frac{1}{\tau_\eta} = \frac{n_{tot}kT}{\eta}. \tag{4.34}$$

At low temperatures ($T \ll T_F$) we can approximate $f^0(1 - f^0) \approx \delta(\epsilon - \epsilon_F)$ and obtain from (4.33) that

$$\frac{1}{\tau_\eta} = \frac{2}{5}\frac{n_{tot}\epsilon_F}{\eta}. \tag{4.35}$$

4.2.1   Viscosity of a uniform gas

We shall now calculate the viscosity of a homogeneous gas using a variational principle commonly employed in transport theory. Defining the operator

$$H[\Phi] = \frac{I[\Phi]}{f^0(1 - f^0)}, \tag{4.36}$$

the linearized Boltzmann equation (4.27) has the form of a linear, inhomogeneous integral equation, $X = H[\Psi]$, where $X = p_x p_y/m$ and H is a positive semi-definite *linear* operator acting on the function

$$\Psi = \frac{kT}{\partial_y u_x}\Phi. \tag{4.37}$$

Using this compact notation, the viscosity can be written in the form

$$\eta = \frac{2}{kT}\langle \Psi, H[\Psi]\rangle_{\mathbf{p}}. \tag{4.38}$$

We note in passing that the same strategy outlined above can be applied to obtain other transport coefficients in the form of scalar products of suitable driving terms with the collision integral: the linearization of the Boltzmann equation with respect to the electric field or the temperature gradient allows one to extract respectively the electrical and thermal conductivities. A lower bound on the viscosity can be found using the Schwarz inequality, that ensures

$$\langle \phi, H[\phi]\rangle_{\mathbf{p}}\langle \Psi, H[\Psi]\rangle_{\mathbf{p}} \geq \langle \phi, H[\Psi]\rangle_{\mathbf{p}}^2 \tag{4.39}$$

for any trial function ϕ. Choosing $\phi = X$, the viscosity can be approximated by the lower bound

$$\eta \gtrsim \frac{2}{kT}\frac{\langle X, X\rangle_{\mathbf{p}}^2}{\langle X, H[X]\rangle_{\mathbf{p}}}. \tag{4.40}$$

The explicit factor of two in the numerator of (4.40) arises from summing the contributions of the two components. The corresponding viscous relaxation rate is then

$$\frac{1}{\tau_\eta} = \frac{\langle X, H[X]\rangle_{\mathbf{p}}}{\langle X, X\rangle_{\mathbf{p}}}, \tag{4.41}$$

which is seen to be independent of the normalization of X. The final expression (4.40) is thus an approximate expression, obtained by a trial function proportional to $v_y p_x$, but it is known [63] to differ at high and low temperatures by only a few per cent from the viscosity obtained from the exact solution of the Boltzmann equation.

The quantity $\langle X, X \rangle_{\mathbf{p}}$ appearing in the denominator of (4.41) can be calculated analytically in terms of the Fermi integral

$$f_n(z) = \sum_{l=1}^{\infty} (-1)^{l+1} \frac{z^l}{l^n} = \frac{1}{\Gamma(n)} \int_0^{\infty} \mathrm{d}t \frac{t^{n-1}}{z^{-1}\mathrm{e}^t + 1}, \qquad (4.42)$$

where $\Gamma(n)$ indicates the Gamma function. Introducing the fugacity $z_0 = \exp(\mu/kT)$ we find

$$\langle X, X \rangle_{\mathbf{p}} = \frac{kT}{3m} \int_0^{\infty} \frac{\mathrm{d}\mathbf{p}}{(2\pi\hbar)^3} p^2 f^0 = \left(\frac{m}{2\pi\hbar} \right)^{3/2} (kT)^{7/2} f_{5/2}(z_0). \qquad (4.43)$$

The calculation of $\langle X, H[X] \rangle_{\mathbf{p}}$ proceeds as in Ref. [61] where a similar quantity was evaluated in the case of scattering between identical bosons above the Bose-Einstein condensation temperature. To make a connection with the results presented in that paper, we note that the collision integral is invariant under rotations in momentum space, and the numerical value of $\langle X, H[X] \rangle_{\mathbf{p}}$ will be unchanged when evaluated with one of the following two trial functions,

$$3p_z^2 - p^2 \quad \text{or} \quad \sqrt{12} p_x p_y, \qquad (4.44)$$

the polynomials being respectively proportional to the spherical harmonic $Y_{l=2}^{m=0}$ and to the normalized linear combination $(Y_{l=2}^{m=2} - Y_{l=2}^{m=-2})/\sqrt{2}$. Substituting Bose distributions with Fermi ones, and noting that the s-wave scattering cross section for identical bosons is twice the one for distinguishable particles, we find

$$\langle X, H[X] \rangle_{\mathbf{p}} = \frac{8}{5\pi^3 m^3} (mkT)^{11/2} \sigma(0) \cdot I_a(T),$$

where $\sigma(0) = 4\pi a^2$ is the integrated cross-section at zero energy and $I_a(T)$ is a the following 4-dimensional integral:

$$I_a(T) = \int_0^{\infty} \mathrm{d}x_0 \int_0^{\infty} \mathrm{d}x_r \int_0^1 \mathrm{d}y \int_0^1 \mathrm{d}y' \, x_0^2 \frac{x_r^7}{1 + x_r^2 \frac{T}{T_a}} \left(1 + y^2 + y'^2 - 3y^2 y'^2 \right) F.$$

Here we have introduced the characteristic temperature

$$kT_a = \frac{\hbar^2}{ma^2} \qquad (4.45)$$

and the dimensionless variables $x_0 = |\mathbf{p}+\mathbf{p}_1|/(4mkT)^{1/2}$ and $x_r = p_r/(mkT)^{1/2}$. Finally, we have defined $y = \cos\theta_r$, where θ_r is the polar angle formed by the vector $\mathbf{p}_r$ with the z axis (similar relations hold for the primed variables), and $F(x_0, x_r, y, y')$ is equal to $f^0 f_1^0 (1 - f^{0\prime})(1 - f_1^{0\prime})$.

In the classical limit, $T \gg T_{\mathrm{F}}$, we may approximate $F \approx f^0 f_1^0$ and the 4-dimensional integral fully decouples yielding

$$I_a^{\mathrm{class}}(T) = \sqrt{\pi} z_0^2 \frac{\bar{\sigma}}{4\pi a^2}.$$

Here $\bar{\sigma}$ is an effective cross section, which depends on the ratio T/T_a:

$$\bar{\sigma} = \frac{4\pi a^2}{3} \int_0^\infty dx\, x^7 \frac{\mathrm{e}^{-x^2}}{1 + x^2 \frac{T}{T_a}}. \tag{4.46}$$

For $T \ll T_a$ we obtain from (4.46) the classical result $\bar{\sigma} = 4\pi a^2$, while in the opposite limit, $T \gg T_a$, Eq. (4.46) yields

$$\bar{\sigma} = 4\pi a^2 \frac{T_a}{3T} = \frac{2}{3} \cdot \frac{2\pi\hbar^2}{mkT}, \tag{4.47}$$

which is seen to be independent of the scattering length a and, apart from a numerical constant, equal to the square of the thermal de Broglie wavelength: in the unitarity limit, where $|a|$ tends to infinity, the calculated viscous relaxation rate approach a finite value that depends on temperature, since the cross section in this case is determined by the typical value of the wave number $p_r/\hbar$ for the relative motion.

The viscosity as given in (4.40) is in the classical limit $T \gg T_F$ equal to

$$\eta_{\mathrm{cl}} = \frac{5\sqrt{\pi}}{8} \frac{\sqrt{mkT}}{\bar{\sigma}}. \tag{4.48}$$

and the viscous relaxation rate expressed in terms of the viscosity using (4.34) is then

$$\frac{1}{\tau_{\eta_{\mathrm{cl}}}} = \frac{8}{5\sqrt{\pi}} n_{\mathrm{tot}} \left(\frac{kT}{m} \right)^{1/2} \bar{\sigma}. \tag{4.49}$$

At low temperatures, $T \ll T_F$, one expects on general grounds that $1/\tau_\eta \propto T^2$ due to the restrictions on the available phase space caused by the occupied states, the so-called Pauli blocking. The magnitude of $1/\tau_\eta$ depends on the dimensionless quantity $\gamma = (k_F a)^2 = 2T_F/T_a$. The corresponding variational solution to the Landau-Boltzmann equation of a Fermi liquid (see Ref. [63], Sec. 6.2.1) yields

$$\frac{1}{\tau_\eta} = 2\pi \frac{kT^2}{\hbar T_a} F(\gamma), \tag{4.50}$$

where the function $F(\gamma)$ is given by the integral

$$F(\gamma) = 2 \int_0^1 dx \frac{x^5}{\sqrt{1 - x^2}} \frac{1}{1 + \gamma x^2}, \tag{4.51}$$

the variable x being equal to the sine of half the angle between the two incoming particle momenta in a collision. The function $F(\gamma)$ decreases monotonically from the $\gamma = 0$ value $F(0) = 16/15$ to its asymptotic expression $F(\gamma) \simeq 4/3\gamma$ for $\gamma \gg 1$.

In the unitarity limit ($|a| \to \infty$) the viscous relaxation rate (4.50) becomes independent of the magnitude of the scattering length, since $F(\gamma)$ in this limit is proportional to $1/a^2$. In general, when the scattering length diverges, the calculated relaxation rate tends to a finite value which depends on temperature. The value of $1/\tau_\eta$ at unitarity vanishes as T^2 at low temperatures and as $T^{-1/2}$ at high temperatures.

In the intermediate temperature region the viscosity can be calculated numerically, and in Fig. 4.1 we plot our results for the viscosity as a function of
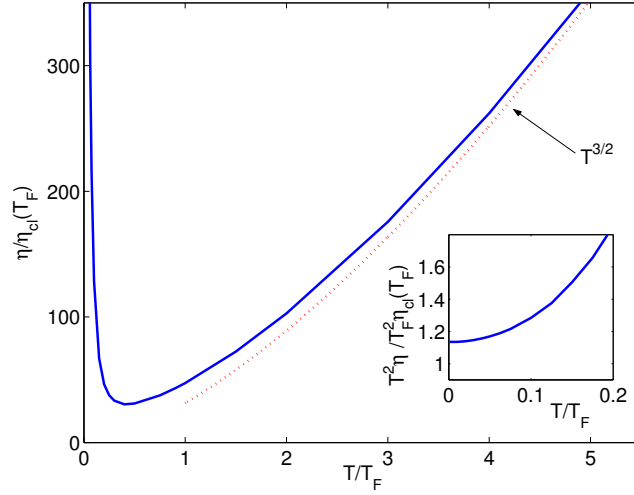
Figure 4.1: The viscosity η for a uniform gas as a function of temperature for $k_{\mathrm{F}}|a| = 4.5$, in units of $\eta_{\mathrm{cl}}(T_{\mathrm{F}})$, the classical value of the viscosity evaluated at the Fermi temperature $T = T_{\mathrm{F}}$ for an energy-independent scattering cross section. The inset illustrates the low-temperature T^{-2} dependence of the viscosity.

temperature for the value $k_{\mathrm{F}}|a| = 4.5$. The inset shows the viscosity multiplied by T^2 in order to illustrate its characteristic low-temperature behavior given by (4.50). Since $T_a = 0.1T_{\mathrm{F}}$ for this value of $k_{\mathrm{F}}|a|$, the viscosity at high temperatures is proportional to $T^{3/2}$. This may be seen by combining the high-temperature relation for the viscosity (4.48) and the unitarity limited effective cross-section (4.47). In the case of energy-independent scattering ($T_a \gg T_{\mathrm{F}}$) the high-temperature viscosity is proportional to $T^{1/2}$.

4.2.2   Viscous relaxation rate of a trapped gas

In order to apply these results to a trapped atomic cloud, we now include the harmonic trap potential (4.1) in the equilibrium Fermi function. The average viscous relaxation rate $1/\tau$ is defined by

$$\frac{1}{\tau} = \frac{\int d\mathbf{r} \, \langle X, H[X] \rangle_{\mathbf{P}}}{\int d\mathbf{r} \, \langle X, X \rangle_{\mathbf{P}}} = \frac{\langle X, H[X] \rangle}{\langle X, X \rangle}, \tag{4.52}$$

where $\langle \ldots \rangle$ denotes multiplication by $f^0(1 - f^0)$ and integration over the whole of phase space,

$$\langle \ldots \rangle = \int \frac{d\mathbf{r} \, d\mathbf{p}}{(2\pi\hbar)^3} f^0(1 - f^0) \ldots \quad . \tag{4.53}$$

Note that the spatial average of (4.41) is carried out for the denominator and numerator separately. As demonstrated in Appendix B, this is the quantity that enters as an effective relaxation rate when we take moments of the kinetic equation in order to determine the frequency and attenuation of the collective
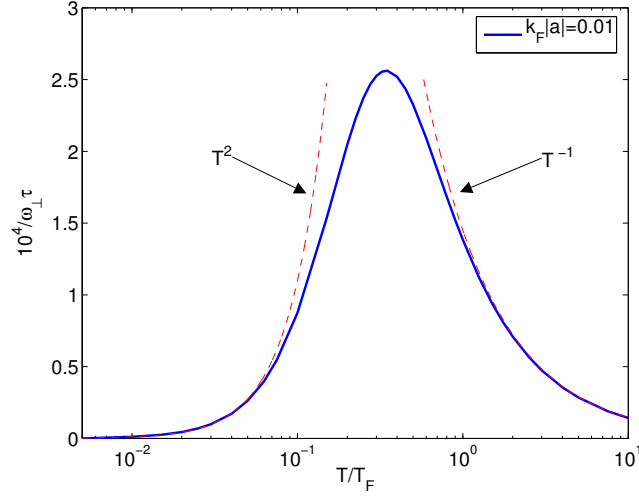
Figure 4.2: The average viscous relaxation rate $1/\tau$ divided by the transverse trap frequency $\omega_\perp$ as a function of temperature, for $k_\mathrm{F}|a| = 0.01$. The asymptotic temperature dependencies are indicated by the dashed lines. Note that the system is highly collisionless, since the maximum value of $1/\omega_\perp\tau$ is about 0.00025.

modes. Our definition generalizes the one adopted in Ref. [60], and reduces to it in the relaxation time approximation $I[p_z^2] \approx (p_z^2 - p^2/3)/\tau(r)$:

$$\frac{1}{\tau} = \frac{\left\langle \frac{1}{\tau(r)} p^4 \right\rangle}{\langle p^4 \rangle}.$$

The calculation of $1/\tau_\eta$ for a uniform gas involved integration over momentum space only, and the presence of a trapping potential can be taken into account through a spatial dependence of the fugacity,

$$z_0 \to z(\mathbf{r}) = z_0 \mathrm{e}^{-V(\mathbf{r})/kT},$$

where z_0 denotes now the fugacity in the center of the trap. The introduction of the rescaled variables $\tilde{r}_i = m\omega_i r_i$ allows us to transform the anisotropic trapping potential into a spherical one, $V(\mathbf{r}) = \tilde{r}^2/2m$, and the viscous relaxation rate is found in terms of 5-dimensional integrations, that we carried out numerically.

The results shown in Fig. 4.2 and all subsequent figures in this Chapter were obtained for a total number N of particles given by $N = 2.8 \times 10^5$, which represents a typical value for the experiments on ^{6}Li reported in [18, 19, 20]. We use the trap frequencies for the cigar-shaped cloud of [18], i.e. an axial frequency $\omega_z = 2\pi \times 70$ Hz and a transverse frequency $\omega_\perp = 2\pi \times 1550$ Hz, giving an anisotropy ratio equal to $\lambda = \omega_z/\omega_\perp = 0.045$.

The resulting average viscous relaxation rate is shown in Figs. 4.2 and 4.3 for two different values of the parameter $k_\mathrm{F}|a|$, one characterizing the regime of weak coupling and the other the regime near the unitarity limit, where k_F is the magnitude of the Fermi wave vector in the center of the trap. At low
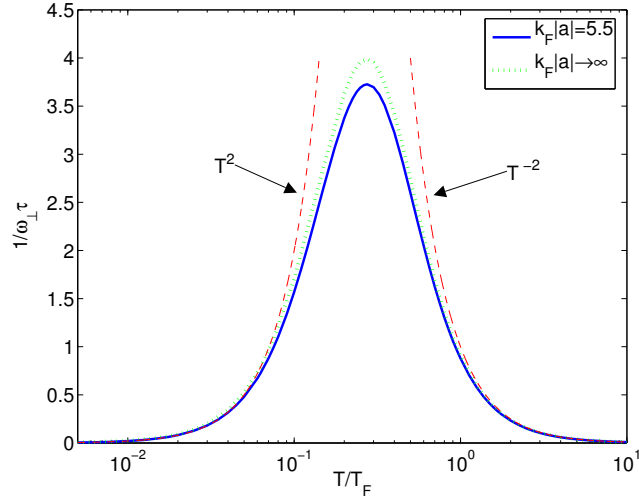
Figure 4.3: The average viscous relaxation rate $1/\tau$ divided by the transverse trap frequency $\omega_\perp$ as a function of temperature, for $k_F|a| = 5.5$ corresponding to the experiment of [18] at a magnetic field of 870 G. The asymptotic temperature dependencies are indicated by the dashed lines. The dotted line is the result obtained in the unitarity limit $|a| \to \infty$.

temperatures the relaxation rates are proportional to T^2, and they exhibit in both cases a pronounced maximum at a temperature somewhat below T_F. The asymptotic behavior at high temperatures differs in the two cases. When $k_F|a|$ is much less than unity, the average viscous relaxation rate decreases as $1/T$ at high temperatures. This may seem to be at odds with the fact that for a uniform gas $1/\tau_\eta$ according to (4.49) is proportional to $T^{1/2}$ in this limit, since $\bar\sigma$ is independent of temperature. However, the average density in a trapped gas is not a constant, but decreases at high temperatures as $T^{-3/2}$, which results in an average relaxation rate proportional to T^{-1}. When $k_F|a|$ is much greater than unity, the temperature-dependent cross section (4.47) causes the relaxation rate to decrease even more strongly, as T^{-2}. In the unitarity limit, when $|a|$ approaches infinity, the average viscous relaxation rate approaches a limiting value indicated by the dotted curve in Fig. 4.3. This is further illustrated in Fig. 4.4 where we plot the average viscous relaxation rate as a function of $1/k_F|a|$ for various temperatures.

In Figs. 4.2, 4.3 and 4.4, we have normalized the viscous relaxation rate to the transverse trap frequency $\omega_\perp$ used in the experiments [18, 20]. The limiting value of the average viscous relaxation rate for $|a| \to \infty$ is seen never to be large compared to $\omega_\perp$, which demonstrates that hydrodynamics cannot be applied to the transverse motion of the trapped atomic clouds in the normal phase. In the next Section we determine the frequency and attenuation of the collective modes and obtain results in support of this general conclusion.
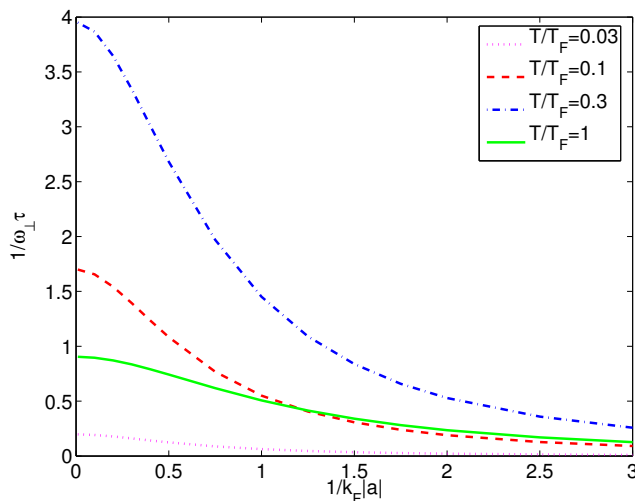
Figure 4.4: The average viscous relaxation rate $1/\tau$ divided by the transverse trap frequency $\omega_\perp$ as a function of $1/k_F|a|$ for four different temperatures. The parameters $T/T_F = 0.03$ and $T/T_F = 0.1$ correspond to the experimental conditions of Refs. [19] and [20], respectively.

4.2.3 Comparison with energy-independent model

In a previous paper, Vichi [55] has calculated the relaxation rate for quadrupole oscillations, averaging the collision integral over a different trial function, and using the zero-energy cross section $\sigma = 4\pi a^2$. His result, Eq. (15) in [55], reads

$$\frac{1}{\omega_{ho}\tau_Q} = \frac{4}{5\sqrt[3]{3}\pi} \left(N^{1/3} \frac{a}{a_{ho}} \right)^2 F_Q \left(\frac{T}{T_F} \right)$$

where ω_{ho} is the geometric mean of the trap frequencies, $a_{ho} = \sqrt{\hbar/m\omega_{ho}}$ the harmonic oscillator length and F_Q a universal function of the reduced temperature T/T_F. In the limit $k_F a \sim 0$ our relaxation rate (see Fig. 4.2) exactly coincides with the one derived by Vichi. The situation is different for the strongly interacting case. The result found by Vichi is manifestly proportional to a^2 and diverges in the unitarity limit $k_F|a| \to \infty$. In contrast, due to the saturation of our cross section for large relative momentum k_r, we find a strong reduction of the relaxation rate (and a finite value in the unitarity limit), implying much less hydrodynamic behavior than what an energy-independent theory would predict (the reduction is of a factor $1/20$ for the continuous line in Fig. 4.3, corresponding to $k_F a = 5.5$).

4.3 Frequency and attenuation of collective modes

We now extract the dispersion relation of the low-lying collective modes by solving the linearized Boltzmann equation (4.16) with an appropriate trial function Φ. The equations of motion (4.17) are modified to take into account the mean-

field potential U given by

$$U(\mathbf{r}) = gn(\mathbf{r}) = g[n^0(\mathbf{r}) + \delta n(\mathbf{r})], \tag{4.54}$$

where $g = 4\pi\hbar^2 a/m$ is the interaction constant. A description of the interactions in term of a mean-field term will hold as long as the gas is sufficiently dilute (for a typical peak density of about 10^{13}atoms/cm^3, this yields $a \lesssim 5000a_0$). The density n^0 denotes the equilibrium density for a single spin, that is $n^0 = n^0_\uparrow = n^0_\downarrow = n^0_{\text{tot}}/2$, and $\delta n(\mathbf{r})$ similarly denotes the non-equilibrium change in density for a single spin. The effective potential is thus the sum of U and the harmonic oscillator potential $V(\mathbf{r})$ given by (4.1), yielding the equations of motion

$$\dot{\mathbf{r}} = \mathbf{v} = \frac{\mathbf{p}}{m}; \quad \dot{\mathbf{p}} = -\frac{\partial(V + U)}{\partial \mathbf{r}}. \tag{4.55}$$

Let us first establish some useful relations between equilibrium quantities. We consider the kinetic equation in equilibrium, where the right hand side of (4.16) vanishes, and insert the equations of motion (4.55), obtaining

$$\sum_{i=x,y,z} \omega_i \left[p_i \frac{\partial f^0}{\partial \tilde{r}_i} - \left(\tilde{r}_i + mg\frac{\partial n^0}{\partial \tilde{r}_i} \right) \frac{\partial f^0}{\partial p_i} \right] = 0, \tag{4.56}$$

or equivalently

$$\sum_{i=x,y,z} \omega_i \left[p_i \frac{\partial[f^0(1-f^0)]}{\partial \tilde{r}_i} - \left(\tilde{r}_i + mg\frac{\partial n^0}{\partial \tilde{r}_i} \right) \frac{\partial[f^0(1-f^0)]}{\partial p_i} \right] = 0. \tag{4.57}$$

We have here introduced the rescaled variables $\tilde{r}_i = m\omega_i r_i$, in terms of which the potential becomes spherically symmetric, $V(\mathbf{r}) = \tilde{r}^2/2m$. If we now multiply (4.57) by $\tilde{x}p_x p_y^2$ and integrate over both position and momentum variables, we obtain

$$\langle p_x^2 p_y^2 \rangle - \langle \tilde{x}^2 p_y^2 \rangle + \frac{m^2}{2}kTg \int d^3r\,(n^0)^2 = 0. \tag{4.58}$$

Using $f^0(1-f^0) = -(mkT/p)\partial f^0/\partial p$, we can calculate analytically the integrals appearing in (4.58) and obtain the virial theorem,

$$E_{\text{kin}} - E_{\text{pot}} + \frac{3}{2}E_{\text{int}} = 0. \tag{4.59}$$

The kinetic, potential and interaction energies are respectively

$$E_{\text{kin}} = 2 \int \frac{d\mathbf{r}\,d\mathbf{p}}{(2\pi\hbar)^3} f^0 \frac{p^2}{2m}, \tag{4.60}$$

$$E_{\text{pot}} = 2 \int \frac{d\mathbf{r}\,d\mathbf{p}}{(2\pi\hbar)^3} f^0 V(\mathbf{r}), \tag{4.61}$$

and

$$E_{\text{int}} = g \int d\mathbf{r}\,(n^0)^2. \tag{4.62}$$

In general, in $d \geq 2$ dimensions the virial theorem holds in the form

$$E_{\text{kin}} - E_{\text{pot}} + \frac{d}{2}E_{\text{int}} = 0. \tag{4.63}$$

To lowest order in the coupling constant g, the linearized version of Eq. (4.16) reads

$$\frac{\partial \Phi}{\partial t} + \sum_{i=x,y,z} \omega_i \left[p_i \frac{\partial \Phi}{\partial \tilde{r}_i} - \left(\tilde{r}_i + mg \frac{\partial n^0}{\partial \tilde{r}_i} \right) \frac{\partial \Phi}{\partial p_i} \right.$$
$$\left. - \frac{mg}{f^0(1-f^0)} \frac{\partial \delta n}{\partial \tilde{r}_i} \frac{\partial f^0}{\partial p_i} \right] = -\frac{I[\Phi]}{f^0(1-f^0)}, \tag{4.64}$$

where n^0 as before denotes the equilibrium density for a single spin while the corresponding non-equilibrium change in the density is

$$\delta n = \int \frac{d^3p}{(2\pi\hbar)^3} f^0(1-f^0)\Phi. \tag{4.65}$$

We shall in the following consider modes for which the drift velocity $\mathbf{u}$ has a spatial dependence given by $u_i \propto r_i$. The deviation function Φ of a fluid moving with velocity $\mathbf{u}$ is proportional to $\mathbf{u} \cdot \mathbf{p}$. Since acting on $\mathbf{u} \cdot \mathbf{p}$ with the left side of (4.16) generates terms like x^2, p_x^2, etc., we follow [60] in choosing the trial function as

$$\Phi = e^{-i\omega t} \sum_{i=x,y,z} (a_i \tilde{r}_i^2 + b_i \tilde{r}_i p_i + c_i p_i^2). \tag{4.66}$$

We insert this Ansatz into the kinetic equation (4.64) and calculate moments multiplying by the product of $f^0(1-f^0)$ and any of the terms $\tilde{x}^2, \tilde{y}^2, \ldots, p_z^2$ appearing in Φ, and subsequently integrating over both $\mathbf{r}$ and $\mathbf{p}$. The result is a set of nine coupled homogeneous equations for the nine coefficients $a_x, a_y, \ldots, c_z$ and the frequencies of the collective modes emerge as the roots of the determinant. The details of the calculation are given in the Appendix for the general case when all three trap frequencies are different.

4.4   Results and comparison with experiment

In order to make contact with recent experiments [18, 19, 20] we consider an axially symmetric trap with $\omega_x = \omega_y = \omega_\perp$ and $\omega_z = \lambda \omega_\perp$. We introduce the parameter

$$\xi = \frac{\frac{3}{2} E_{\text{int}}}{E_{\text{pot}}}, \tag{4.67}$$

which, as we shall see, determines the sign and relative magnitude of the frequency shifts. We shall expand our results to first order in ξ, since our mean-field treatment of the interaction in the streaming terms of the kinetic equation is only valid when $|\xi|$ is small compared to unity. The temperature dependence of ξ is shown in Fig. 4.5. In accord with our first order treatment of the mean field we calculate ξ by approximating the equilibrium Fermi function, which enters E_{int} as well as E_{pot}, by its value in the absence of interaction. At high temperatures one finds from (4.67) that $|\xi| \propto T^{-5/2}$, since the interaction energy E_{int} in the classical regime is inversely proportional to the volume of the cloud ($E_{\text{int}} \propto T^{-3/2}$), while the potential energy is proportional to the temperature.

The determinant of the matrix, which is derived in Appendix B, has the form of a polynomial in the frequency ω. The vanishing of the determinant
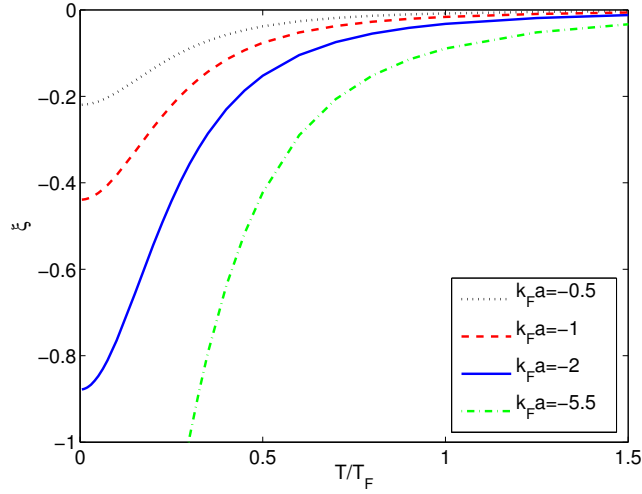
Figure 4.5: The temperature dependence of the parameter ξ given by (4.67) for different values of $k_F a$. At high temperatures $|\xi|$ decreases as $T^{-5/2}$.

yields the following equation

$$\omega \left[(\omega^2 - \omega_{\mathrm{hd}}^2) - i\omega\tau(\omega^2 - \omega_{\mathrm{cl}}^2) \right]$$
$$\left[(\omega^2 - \omega_{\mathrm{hd+}}^2)(\omega^2 - \omega_{\mathrm{hd-}}^2) - i\omega\tau(\omega^2 - \omega_{\mathrm{cl+}}^2)(\omega^2 - \omega_{\mathrm{cl-}}^2) \right] = 0, \qquad (4.68)$$

where τ is defined by (4.52). Note that the average viscous relaxation rate $1/\tau$ depends on temperature as illustrated in Figs. 4.2, 4.3 and 4.4.

In general, the solutions to (4.68) have real and imaginary parts, $\omega = \mathrm{Re}(\omega) + i\mathrm{Im}(\omega)$, which determine the frequency and the damping of the collective modes, respectively. The (purely real) frequencies appropriate to the hydrodynamic limit, $\omega\tau \to 0$, are denoted by subscript (hd), while those for the collisionless limit, $\omega\tau \to \infty$, carry the subscript (cl). We will quote our results only up to first order in ξ since our calculation of the frequency shifts caused by the interaction cannot be trusted beyond that. The first term in square brackets in (4.68) corresponds to the $m = 2$, λ-independent mode, see Eq. (4.12), and we find

$$\omega_{\mathrm{hd}}^2 = 2\omega_\perp^2 \qquad (4.69)$$

$$\omega_{\mathrm{cl}}^2 = 4\omega_\perp^2 (1 - \frac{\xi}{2}). \qquad (4.70)$$

The second term in square brackets represents the two $m = 0$ modes, see Eq. (4.13), and in the hydrodynamic limit we find

$$\frac{\omega_{\mathrm{hd\pm}}^2}{\omega_\perp^2} = \frac{5 + 4\lambda^2 \pm \gamma}{3} \pm \xi \frac{4\lambda^4 - \lambda^2(5 \mp \gamma) + 2(5 \pm \gamma)}{6\gamma}$$

with $\gamma = (25 - 32\lambda^2 + 16\lambda^4)^{1/2}$. For $\lambda \ll 1$ the latter are given by

$$\omega_{\mathrm{hd+}}^2 = \frac{10}{3}\omega_\perp^2 (1 + \frac{\xi}{5}) \quad \text{and} \quad \omega_{\mathrm{hd-}}^2 = \frac{12}{5}\omega_z^2 (1 + \frac{\xi}{20}). \qquad (4.71)$$
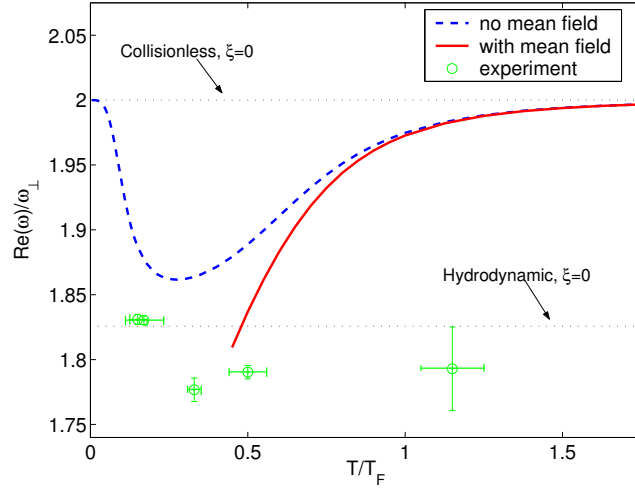
Figure 4.6: The calculated frequency of the breathing $(+)$ mode as a function of temperature, with and without the mean-field correction for values of $|\xi|$ less than or equal to 0.5. The experimental values from [18] are indicated with the estimated error bars included.

The modes labeled $+$ and $-$ are the breathing and quadrupole modes, respectively, which are studied in the experiments [18, 19, 20].

In the collisionless limit, a Taylor expansion of the roots of the determinant for small ξ and for a generic trap anisotropy λ is not analytic in $\lambda = 1$ (since two normal modes are degenerate in the spherical case). The expansion can nonetheless be performed separately for the two cases of elongated traps $(\lambda \ll 1)$

$$\omega_{cl+}^2 = 4\omega_\perp^2 \quad \text{and} \quad \omega_{cl-}^2 = 4\omega_z^2(1 - \frac{\xi}{4}) \tag{4.72}$$

and spherical traps $(\lambda = 1)$

$$\omega_{cl+}^2 = 4\omega_\perp^2(1 + \frac{\xi}{4}) \quad \text{and} \quad \omega_{cl-}^2 = 4\omega_\perp^2(1 - \frac{\xi}{2}). \tag{4.73}$$

In addition, we find from (4.68) three purely damped modes, $\text{Re}(\omega) = 0$, corresponding to relaxation of temperature anisotropies. The first one is associated with the overall factor ω in front of the square brackets, corresponds to a homogeneous temperature change in all directions and causes no relaxation at all, $\omega = 0$. The second comes from the first square bracket, has $m = 2$ and frequency $\omega = -i/\tau$ in the hydrodynamic limit $\omega_\perp \tau \ll 1$ and $\omega = -i\omega_{hd}^2/\omega_{cl}^2 \tau$ in the collisionless limit, again λ-independent since it involves only relaxation in the $x - y$ plane. The third arises from the second square bracket, has $m = 0$ and frequency $\omega = -i/\tau$ in the hydrodynamic limit and $\omega = -i\omega_{hd+}^2\omega_{hd-}^2/\omega_{cl+}^2\omega_{cl-}^2 \tau$ in the collisionless limit.

In Fig. 4.6 we plot the calculated frequency as a function of temperature for $k_F|a| = 5.5$, which corresponds to the parameters quoted in [18], along with their experimental values. Since we assume $|\xi|$ to be small compared to unity, we show the mean-field curve only in the temperature region where $|\xi|$
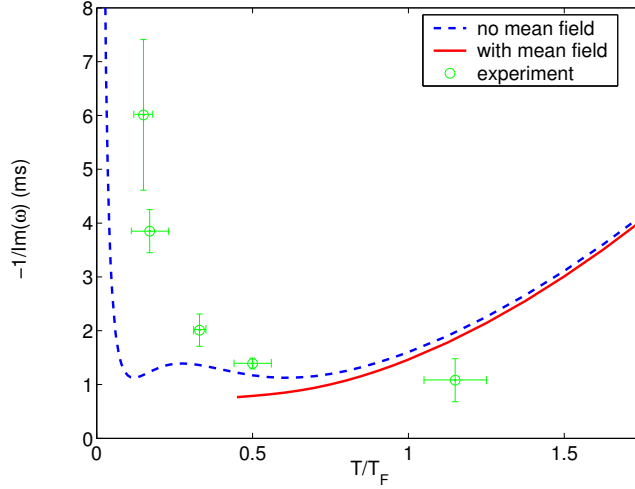
Figure 4.7: The damping time of the breathing (+) mode as a function of temperature, with and without the mean-field correction. The mean-field corrected curve is plotted for values of $|\xi|$ less than or equal to 0.5. The experimental values from [18] are indicated.

is less than 0.5. There is a clear discrepancy between our calculated frequency and the experimental result at $T = 1.15T_{\mathrm{F}}$ and its possible origin is discussed in the next Sec. 4.5. The corresponding results for the damping, given by the imaginary part of the frequency, are shown in Fig. 4.7. In order to compare with the experimental data below $0.5T_{\mathrm{F}}$ in Figs. 4.6-4.7, it is necessary to improve our treatment of the interaction effects in the streaming terms of the kinetic equation.

In Figs. 4.8 and 4.9 we show results for the real and imaginary part of the frequency of the quadrupole (-) mode. In elongated traps the mode implies motion mainly in the axial direction and, since $\omega_z \ll \omega_\perp$, there is a broad temperature region where the system behaves hydrodynamically. The damping shows a double-peak structure that reflects, as temperature is lowered, the transition between the different regimes, from collisionless to hydrodynamic and back to collisionless behavior [55]. The mean-field corrections in Fig. 4.8 are seen to be much smaller than those in Fig. 4.6, in agreement with the different prefactors of ξ in Eq. (4.71).

4.4.1 Comparison with earlier results

In a recent work, Pedri *et al.* [56] calculated the frequency shifts induced by interaction describing the non-equilibrium distribution function by a scaling Ansatz,

$$f(t, r_i, v_i) = \frac{1}{\prod_j (b_j \theta_j^{1/2})} f^0 \left[\frac{r_i}{b_i}, \frac{1}{\theta_i^{1/2}} \left(v_i - \frac{\dot{b}_i}{b_i} r_i \right) \right], \qquad (4.74)$$

f^0 being the equilibrium distribution function, $b_i(t)$ and $\theta_i(t)$ 6 scaling parameters that describe linear dilatation and effective temperature in each direction.
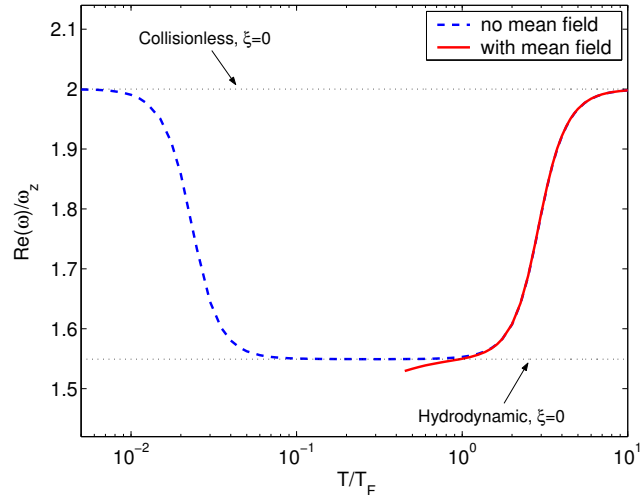
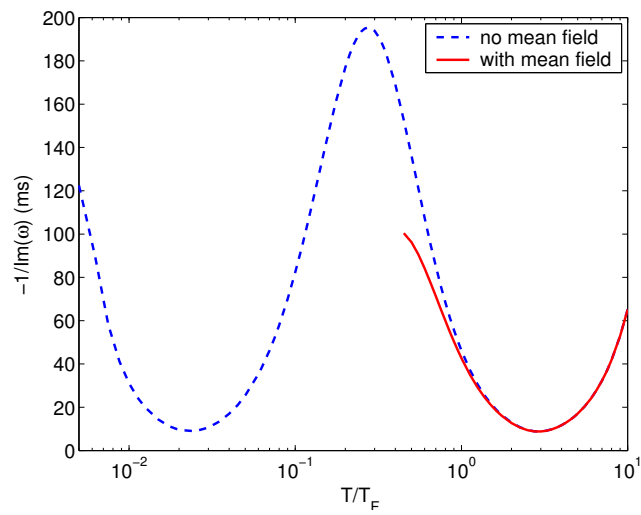Figure 4.8: The frequency of the quadrupole $(-)$ mode as a function of temperature.

Figure 4.9: The damping time of the quadrupole $(-)$ mode as a function of temperature.

For small perturbations, one can write $b_i = 1 + \delta b_i$ and $\theta_i = 1 + \delta\theta_i$ and expand Eq. (4.74) to recast it in a more familiar form as $\delta f = f^0(1 - f^0)\Phi$ where

$$\Phi = a_i\left(\tilde{r_i}^2 - i\frac{\omega}{\omega_i}\tilde{r}_ip_i\right) + c_ip_i^2$$

with $a_i = -2\delta b_i$ and $c_i = -\delta\theta_i$. In the spherical case and in the absence of mean field, inserting this Ansatz into the linearized Boltzmann equation and taking the moment with $\tilde{r}^2$ one easily obtains the relation $a = -c$, that allows to find

$$\int \mathrm{d}\mathbf{r}\,\delta n = \int \frac{\mathrm{d}\mathbf{r}\mathrm{d}\mathbf{p}}{(2\pi\hbar)^3}f^0(1 - f^0)\Phi = 0.$$

In the non-interacting limit, the Ansatz of Pedri *et al.* explicitly enforces particle conservation at the expense of reducing the number of variational parameters. Our results for the frequency shifts, valid to first order in ξ, are in agreement with those of Pedri *et al.* when expanded to first order in ξ. Our results differ to second and higher order. This is understandable since the form of Eq. (4.66) is more general than the scaling Ansatz (4.74), which involves six rather than nine parameters. However, since our calculation of the frequency shifts caused by the interaction cannot be trusted beyond first order in ξ, our results are in essential agreement with those of [56]. Our work thus extends that of [56] in the sense that we determine ξ and τ as functions of temperature, thereby allowing for a direct comparison with experiment.

4.5   Discussion and conclusions

In this Chapter, we have calculated the viscous relaxation rate for an interacting Fermi gas in its normal phase by means of an approximate solution of the Boltzmann equation in both the uniform and trapped cases. We have found the asymptotic behavior at low/high temperatures and for weak/strong interactions, and performed a numerical integration of the collision integral mapping the intermediate temperatures currently investigated in the experiments [18, 19, 20]. In particular we have pointed out that, for typical experimental parameters, hydrodynamic conditions for motion in the transverse direction are not attained even in the unitarity regime $k_\mathrm{F}|a| \gg 1$.

Subsequently we have solved the kinetic equation for the semi-classical distribution function including the mean field as an additional streaming term and determined the frequency and attenuation of collective modes as a function of temperature in presence of strong inter-particle interactions. Our treatment applies to both the collisionless and the hydrodynamic limits, as well as to the intermediate regime.

We have quantitatively compared our theory with a recent experiment performed in the Duke University group [18] and found definite discrepancies in the high temperature region: observed frequencies agree with the hydrodynamic result even for $T > T_\mathrm{F}$, a regime where the gas is definitely in its normal phase and our theory predicts a behavior closer to the collisionless one. In the following we analyze possible origins of this disagreement.

To begin with, we note that the cross section (4.19) used in our treatment of the collision integral neglects medium effects, i.e. the possibility that intermediate scattering states may not be available due to Fermi blocking. As

shown in [64], these effects can be significant at very low temperatures. In a subsequent work Bruun and Smith [65] have improved the calculation of the viscous relaxation rate presented in Sec. 4.2 using a many-body scattering matrix which explicitly includes Fermi blocking of intermediate states. At unitarity and for temperatures close to T_C (the temperature for the transition to the superfluid state, predicted to be at about $0.3T_{\rm F}$), the improved cross section gives an important increase of the relaxation rate, almost an order of magnitude in the uniform case. When averaging over the spatial profile of a trapped cloud, medium effects are reduced in the low-density region at the boundaries and the increase is only a factor of 3. The improved collision rate nonetheless reduce to ours in both the weakly-interacting ($k_{\rm F}|a| \ll 1$) and/or high temperature ($T \gtrsim 0.5T_{\rm F}$) regimes, and the discrepancy at temperatures of order $T_{\rm F}$ between our theory and the experimental results of [18] is not solved by the inclusion of the improved scattering matrix.

The Boltzmann equation was originally developed to describe classical and dilute gases, which obey Boltzmann statistics and are satisfactorily described by a picture of freely propagating particles rarely undergoing only two-body collisions. Despite its "classical" origins, the Boltzmann equation can be applied to arbitrarily low temperatures provided the appropriate quantum distribution (fermionic or bosonic) is used whenever the thermal de Broglie wavelength becomes larger than the interparticle distance. Kinetic theory has also been successfully employed in describing the collective properties of the so-called Fermi liquids, such as electrons in metals and liquid ^{3}He: in these systems interactions are indeed very strong but Fermi statistics ensures that at temperatures $T \ll T_{\rm F}$ collective excitations are well defined quasiparticles with very long lifetimes, proportional to $(T_{\rm F}/T)^2$, that can be satisfactorily described by the Boltzmann equation.

When dealing with strongly interacting gases, an important role might be played by a number of processes beyond two-body scattering, such as many-body encounters, pairing or formation of short-lived molecules. As one goes from the weak- to the strong-coupling regime the length scale associated with the interactions becomes formally infinite, and simple dimensional considerations show that thermodynamic quantities follow a universal behavior, each becoming simply proportional to its respective non-interacting value. The adjective "unitarity" often used to designate this regime is indeed motivated by this universality. The proportionality constant is independent of the particular system and is usually a number of order one: none of the thermodynamic variables shows particularly marked signatures of the transition. Transport properties should instead be more deeply affected when the interaction parameter becomes infinite.

Gelman *et al.* [66] advance the hypothesis that ultracold gases near Feshbach resonances might be near-ideal liquids, with mean free paths comparable to or even smaller than the interparticle distance: they suggest describing low-frequency dynamics of such strongly-interacting matter within the framework of viscous hydrodynamics, which is based on an expansion in inverse power of the cross-section and yields damping rates that are proportional to the integrated viscosity [57]. This approach seems interesting and worthy of further investigation.

Finally, in the pioneering experiments described earlier in this Chapter temperature calibrations were extremely hard to perform and small trap anhar-

monicities in the radial directions ($\omega_x \neq \omega_y$) could affect substantially results that need to be precise at the percent level to distinguish between the different regimes[2].

It would be interesting to study further the behavior of the gas all the way through the transition between the weakly- and strongly-interacting regimes: by measuring the oscillation frequencies at various magnetic fields as a function of temperature, one could test the predictions for shifts in frequency and attenuation due to the interaction. Quoting from a recent paper [67], "the observed hydrodynamic behavior at high temperatures is not explained by existing theories".

---

[2]The Duke group recently measured the anisotropy of their trap to be $\omega_x/\omega_y \approx 1.1$ [21].

Chapter 5

3D Anderson localization of matter waves

In a paper that dates back to the early years of quantum mechanics, von Neumann and Wigner [68] showed that the Schrödinger equation can admit isolated eigenstates embedded in the continuum of states with energy higher than the maximum of the potential. By an elegant argument, they constructed a class of bizarre potentials with rapid oscillations, but bounded and vanishing at infinity, and showed that these potentials support eigenfunctions that are localized, i.e. square-integrable. An example of a potential and a wave function of a localized state constructed by this model is shown in Fig. 5.1. Von Neumann and Wigner attributed the existence of these puzzling *localized eigenstates*, that are stationary even though the motion would be unbounded classically, to *diffractive interference*.

Many years later Anderson, in his celebrated work "Absence of Diffusion in Certain Random Lattices" published in 1958 [27], proposed that the number of these isolated states could grow considerably in the presence of disorder. He dealt with a simple model Hamiltonian,

$$H = \sum_n \epsilon_n \ket{n}\bra{n} + \sum_{m,n} V_{m,n} \ket{m}\bra{n}, \tag{5.1}$$

that describes non-interacting particles hopping on a 3D lattice with random on-site energies ϵ_n, and demonstrated that for a sufficiently strong disorder there is, after an infinite time, a non-zero probability of finding at a certain site n_0 a particle that had been placed on the same site at $t = 0$. He showed also that the populations of the neighboring sites decrease exponentially fast when moving away from n_0. There exists therefore in his model a definite threshold for the strength of the disorder beyond which diffusion comes to a halt: this peculiar quantum phenomenon, which more generally leads to the formation of a macroscopic number of localized eigenstates as a non-interacting ensemble is exposed to a static disordered potential, is usually referred to as *Anderson localization*. A localized state does not extend over the whole system and does not contribute to transport: when a sufficient number of those is formed, diffusion is inhibited and transport theory becomes inadequate to describe the state of the system. The topic has been subject of intense investigations in the last 40
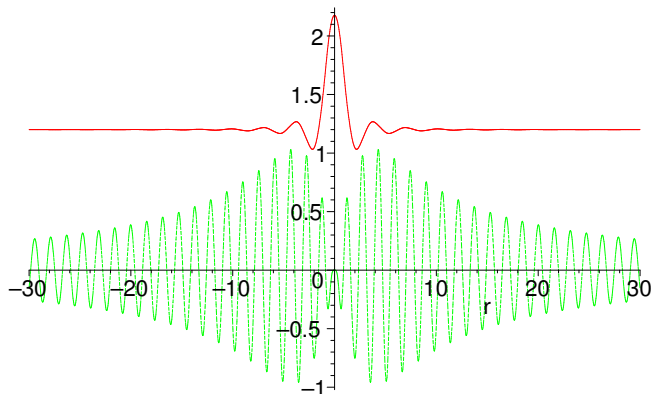
Figure 5.1: Localized state (continuous red line), confined by a bounded, non-random potential vanishing at infinity (dashed green line), obtained by the von Neumann-Wigner method [68, 69]. The state has an energy equal to twice the maximum of the potential.

years (for a review on the work done, see e.g. [25, 26]), but the overall picture is still far from being clear and the only experimental signature of the transition in three-dimensional case [28] has been object of a long debate.

As correctly argued by von Neumann and Wigner, the localization of the wave functions is due to destructive quantum interference of multiply scattered waves, and its onset can be qualitatively predicted by the Ioffe-Regel criterion, which states that the wavelength of the matter wave λ should be larger than the mean free path l,

$$\lambda \gtrsim l. \tag{5.2}$$

The mean free path is related to the density of scatterers n and the scattering cross section σ by $l = 1/n\sigma$, and ultracold atoms seem to be a perfect playground for putting in evidence Anderson localization since very large λ can be obtained and atom-atom interactions can be easily tuned by means of Feshbach resonances. Moreover, ultracold gases have very weak coupling to the environment, and undesired effects of decoherence can be made negligible.

In recent months, a rapid succession of experiments on Bose-Einstein condensates (BECs) in random potentials has been reported [30, 31, 32, 33]. In these experiments, a spatially random one-dimensional potential is induced on cigar-shaped BECs by means of a speckle field [29]. The analysis of density profiles after expansion provided evidence for many disorder-related effects, such as fragmentation of the condensate, suppression of diffusion, frequency shifts and damping of collective oscillations. Nonetheless, if one is interested in providing evidence for Anderson localization, care needs to be taken in order to guarantee that the matter wave is not classically trapped, i.e. in the case of speckle potentials one must require that the chemical potential is much bigger than the typical amplitude of the random potential. In particular, this will never be satisfied in the late stage of the expansion, and small fractions of the cloud remain trapped in deep valleys of the random potential. Moreover, repulsive interactions smooth the modulations of the wave function induced by the random potential, and localization is expected to be inhibited unless the

healing length of the condensate $\xi = 1/\sqrt{8\pi na}$ is much larger than the typical correlation length of the pattern Δr [33, 70]. In the experiments with speckles [30, 31, 32, 33] this condition is generally not satisfied, since the minimum length scale for the disordered potential is limited by diffraction to $\Delta r \sim 5 - 20\mu$m, while typically $\xi \sim 1\mu$m.

In this Chapter, we analyze a way of realizing a disordered potential that allows one to obtain much smaller correlation lengths and where classical localization effects are completely ruled out. Following the work of Gavish and Castin [34] and extending their analysis to three-dimensions, we study the behavior of a non-interacting matter wave in the presence of a random gas of scatterers, constituted by particles of another species populating randomly chosen sites of a deep optical lattice. In Sec. 5.1 we describe in detail our proposal, both its practical implementation and its modeling. In Sec. 5.2, we show numerically that the considered scheme leads to the appearance of a large number of localized states in a range of parameters accessible by present experiments, provided that the effective coupling constant of the matter wave to a single scatterer is large enough. Section 5.3 is devoted to the study of the scattering between two particles, one of which is free and the other trapped in a lattice site, and to the discussion of the confinement-induced resonances arising in this problem: our analysis shows that the large effective coupling constants required in Sec. 5.2 can indeed be obtained. Possible strategies for observation of these localized states and our conclusions are reported in Sec. 5.4. Appendices C and D contain the calculation of the Green's function for a particle in a box and the detailed derivation of an integral equation appearing in the two-body scattering problem.

5.1   The model

We propose to study quantum localization effects induced by a static random potential on a non-interacting matter wave. A schematic view of the proposed setup is reported in Fig. 5.2. A one-dimensional analysis of this model has been presented in [34], and in this Chapter we study the three-dimensional case. We address here the question of how to realize experimentally both the disordered potential and the non-interacting matter wave, and introduce our model Hamiltonian, carefully justifying all the approximations involved. The numerical solution of the model is presented in Sec. 5.2.

5.1.1   The disordered potential

The scatterers are a set of identical particles, whose chemical species and quantum numbers will be indexed by the letter B, randomly occupying (with filling factor $p < 1$) the sites of a 3D cubic optical lattice. The potential seen by the B atoms is produced by a superposition of three identical laser standing waves along the x, y and z axes,

$$V^B(\mathbf{r}) = V_0^B[\sin^2(k_L x) + \sin^2(k_L y) + \sin^2(k_L z)], \qquad (5.3)$$

where $V_0^B > 0$ is the modulation depth of the lattice and $k_L = 2\pi/\lambda_L$ is the laser wavenumber. We shall denote the lattice spatial period along each axis by $d = \lambda_L/2 = \pi/k_L$. Multiple occupation of a lattice well is assumed to be absent,
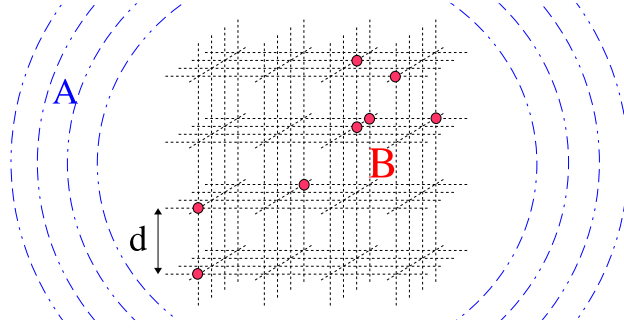
Figure 5.2: Sketch of our proposal: a matter wave (A, blue) scatters on randomly distributed particles (B, red), each occupying the vibrational ground state of a node in a 3D optical lattice (here the average occupancy p is 10%). The lattice does not act on the matter wave A.

by use of polarized fermions, or by creation of vacancies in a unit occupancy Mott phase state [23], or simply by choosing p sufficiently small to make it statistically irrelevant.

We choose the lattice depth V_0^B to be much larger than the recoil energy $E_r^B = \hbar^2 k_L^2/2m_B$ of the B atoms so that the tunneling time of B atoms from one lattice site to another ($t_{\text{tunnel}} \approx 3 \times 10^4 \hbar/E_r^B$ for $V_0^B = 50E_r^B$) is negligible over the duration of the experiment and the disordered spatial pattern of B atoms is static.

We also require that each B atom is found in the vibrational ground state of the local lattice micro-trap. This condition would be achieved automatically if one raises adiabatically the optical lattice on top of a condensate cloud of atoms B and ensures that the A atoms interact with an ensemble of identical potentials (each centered on an occupied site), and that each scattering event is elastic if the A atoms have sufficiently low energy: indeed, energy conservation guarantees that the B atom is left in the vibrational ground state after scattering with an A atom of momentum k if

$$\frac{\hbar^2 k^2}{2m_A} \ll \hbar\omega = 2(V_0^B \, E_r^B)^{1/2} \qquad (5.4)$$

where ω is the oscillation frequency of a B atom in a micro-trap.

The required density for the trapped particles is not particularly high for ultracold gases standards ($n \lesssim 10^{13}$ atoms/cm^3), and one could also start from an atomic molasses of atoms B, that does not need to be in the quantum degenerate regime. In this case, each of the B atoms might be cooled to its vibrational ground state by using Raman sideband cooling techniques [71, 72].

A last point is to ensure that spontaneous emission processes are negligible for the B atoms. In order to achieve large values of V_0^B with negligible heating of the trapped scatterers, we require the lattice to be blue-detuned with respect to the strongest transition of the B atoms (in blue-detuned lattices, particles are trapped in the minima of intensity of the stationary light field). Including the Lamb-Dicke type reduction factor coming from the trapping of B atoms close

to the nodes of the laser field, one gets the fluorescence rate

$$\Gamma^B_{\text{fluo}} = \Gamma_B \frac{V^B_0}{\omega_L - \omega_B} \frac{3k^2_L}{2m_B\omega} \tag{5.5}$$

where $\omega_L - \omega_B$ is the atom-laser detuning and Γ_B is the spontaneous emission rate of B atoms.

For the bosonic ^{87}Rb isotope of rubidium ($\lambda_{B,D2} = 780$nm, $\lambda_{B,D1} = 794.8$nm) and an optical lattice tuned at $\lambda_L = 779$nm, only at 1nm to the blue of the strongest rubidium transition at 780nm, at the required lattice intensity $V^B_0 = 50E^B_r$ the tunneling time is $t_{\text{tunnel}} \approx 1.3$s and the fluorescence rate is $\Gamma^B_{\text{fluo}} \sim 10^4 E^B_r/\hbar \sim 3$s^{-1}, allowing experimental times up to 300ms.

5.1.2   Model Hamiltonian for the matter wave

The matter wave to be Anderson-localized is made of atoms of another species, that we will label by A. We shall ignore interaction effects among these A atoms. One way to fulfill this condition in a real experiment would be to take spin polarized fermionic atoms: s-wave interactions are prohibited by the exclusion principle and p-wave interactions are very weak at low energies in the absence of a p-wave resonance.

The A atoms experience interactions with the trapped species B. We model these interactions at low energy by static contact potentials, corresponding to infinitely-massive point-like scatterers, each located at the center of a micro-well occupied by a B atom:

$$\mathcal{V} = \sum_{\mathbf{r}_j \in \text{occupied sites}} g_{\text{eff}}\delta(\mathbf{r}_A - \mathbf{r_j})\partial_{|\mathbf{r}_A - \mathbf{r_j}|}\left(|\mathbf{r}_A - \mathbf{r_j}|\ldots\right). \tag{5.6}$$

The coupling constant of this effective interaction is

$$g_{\text{eff}} = \frac{2\pi\hbar^2 a_{\text{eff}}}{m_A}, \tag{5.7}$$

where

$$a_{\text{eff}} = a_{\text{eff}}\left(\frac{a}{a_{\text{ho}}}, \frac{m_B}{m_A}\right)$$

is the scattering length of an A atom on a trapped B atom. The harmonic-oscillator length is $a_{\text{ho}} = \sqrt{\hbar/m\omega}$ and a is the $A - B$ scattering length in free space. The sketch in Fig. 5.3 shows pictorially how the effective interaction arises. The value of a_{eff} and the validity condition of our model potential, Eq. (5.6), will be given in Sec. 5.3.

The A atoms also experience the optical lattice potential, with the same spatial dependence as in Eq. (5.3) but with a different modulation amplitude V^A_0. We require the optical lattice to be much closer to resonance with B atoms than with A atoms, $|\omega_L - \omega_A| \gg |\omega_L - \omega_B|$, such that V^A_0 will be much smaller than V^B_0. In particular, we impose that

$$|V^A_0| \ll E^A_r = \frac{\hbar^2 k^2_L}{2m_A} \tag{5.8}$$

so that, in the absence of B atoms, the A atoms can be safely considered as free. In this respect, a particularly promising combination is given by fermionic ^{6}Li
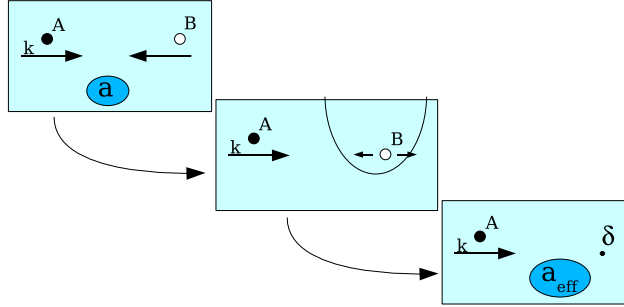
Figure 5.3: Left: in free space, A and B interact with scattering length a. Center: the B particles are trapped in micro-wells of the optical lattice. Right: at low energy, the scattering dynamics of particles A is well described by collisions with static point scatterers. The confinement affects the interaction strength, and the appropriate scattering length a_{eff} is calculated via the two-body scattering problem solved in Sec. 5.3.

for the species A ($\lambda_A = 671$nm) and ^{87}Rb for the species B: taking $\lambda_L = 779$nm and a laser intensity such that $V_0^B = 50E_r^B$, one finds[1] $V_0^A = -0.04E_r^A$.

We shall therefore neglect the effect of the optical lattice on the A atoms and take as a model Hamiltonian for the matter wave:

$$\mathcal{H} = \mathcal{H}_0 + \mathcal{V} \quad \text{with} \quad \mathcal{H}_0 = -\frac{\hbar^2}{2m_A}\Delta_{\mathbf{r}_A}. \tag{5.9}$$

We note in passing that in the original Anderson model the A particles were instead assumed to be in the tight-binding regime.

In the low-energy limit, our model can be also used to describe a matter wave scattering on an ensemble of randomly-distributed hard spheres of radius a_{eff}. The related problem of a gas of hard spheres in a potential that is the sum of randomly located scattering centers of random strengths was considered by Huang and Meng in [73].

5.2   Localized states

A simple estimate shows that the setup we propose allows one to approach the localized regime with experimentally reasonable parameters. As we will see in Sec. 5.3, the effective scattering length presents an infinite number of divergences that can be exploited to obtain a resonant cross-section for the matter wave, $\sigma = 4\pi/k^2$. In this case, the Ioffe-Regel criterion (5.2) reads:

$$kd \lesssim (4\pi p)^{1/3}, \tag{5.10}$$

which for a filling factor $p = 10\%$ yields $kd \lesssim 1$. A typical thermal wave number can be estimated by $\hbar^2 k^2/2m_A \approx 3k_B T/2$ and the former condition

---

[1]If the matter wave is a gas of fermionic ^{40}K atoms ($\lambda_A = 769.9$nm), the same calculation yields $V_0^A = -3.6E_r^A$. Due to the smaller detuning and the larger mass, the optical potential would induce noticeable effects on the potassium matter wave.

can be written as

$$T \lesssim \frac{(4\pi p)^{2/3}}{3} \frac{\hbar^2}{m_A k_B d^2}.$$ (5.11)

With an inter-well distance $d \approx 400$nm, favorable conditions for the localization of a ^{6}Li fermionic cloud are obtained at temperatures of order 200nK, which can be routinely reached in present experiments.

In this Section, we numerically investigate the possibility for the disordered model Hamiltonian Eq. (5.9) to lead to matter wave localization. A central question is now how to obtain numerical evidence for it. Various answers have been given in the literature, and in the following we will approach the problem from different directions.

5.2.1 Decay of the off-diagonal elements of the resolvent

A criterion presented by Kramer and MacKinnon [26] consists in showing that, at a positive energy $E \equiv \hbar^2 k^2 / 2m_A$, off-diagonal elements of the resolvent $\mathcal{G} = (E + i0^+ - \mathcal{H})^{-1}$ in real space decrease exponentially with the distance between the two considered points. This is straightforward to implement numerically, and the equivalent problem for light waves has been addressed in [35, 36]. The resolvent in presence of N point-like scatterers can be expanded in increasing powers of the interaction,

$$\mathcal{G} = \mathcal{G}_0 + \mathcal{G}_0 \mathcal{V} \mathcal{G}_0 + \mathcal{G}_0 \mathcal{V} \mathcal{G}_0 \mathcal{V} \mathcal{G}_0 + \dots,$$ (5.12)

$\mathcal{G}_0$ being the resolvent of $\mathcal{H}_0$. The particle propagator in free space is

$$g_0 (\mathbf{r} - \mathbf{r}') \equiv \langle \mathbf{r} | \mathcal{G}_0 | \mathbf{r}' \rangle = -\frac{m_A}{\hbar^2} \frac{e^{ik|\mathbf{r}-\mathbf{r}'|}}{2\pi |\mathbf{r} - \mathbf{r}'|}.$$ (5.13)

Assuming $\mathbf{r}, \mathbf{r}' \neq \{\mathbf{r}_j\}$, for the matrix elements of the second order term we find

$$\langle \mathbf{r} | \mathcal{G}_0 \mathcal{V} \mathcal{G}_0 \mathcal{V} \mathcal{G}_0 | \mathbf{r}' \rangle = g_{\text{eff}}^2 \sum_{j \neq l} g_0 (\mathbf{r} - \mathbf{r}_j) g_0 (\mathbf{r}_j - \mathbf{r}_l) g_0 (\mathbf{r}_l - \mathbf{r}') +$$
$$g_{\text{eff}}^2 \sum_{j=l} g_0 (\mathbf{r} - \mathbf{r}_j) \left\{ \frac{\partial}{\partial r} \left[r g_0 (\mathbf{r}) \right] \bigg|_{r=0} \right\} g_0 (\mathbf{r}_j - \mathbf{r}').$$ (5.14)

The pseudo-potential regularizes the terms with $j = l$, which are otherwise divergent:

$$\frac{\partial}{\partial r} \left[r g_0 (\mathbf{r}) \right] \bigg|_{r=0} = -\frac{m_A}{\hbar^2} \frac{ik}{2\pi}$$ (5.15)

The higher order terms are treated in a similar way and the resulting geometric series can be re-summed to give

$$\langle \mathbf{r} | \mathcal{G} | \mathbf{r}' \rangle = g_0 (\mathbf{r} - \mathbf{r}') + \frac{2\pi\hbar^2}{m_A} \sum_{jl} g_0 (\mathbf{r} - \mathbf{r}_j) \left[M^{-1} \right]_{jl} g_0 (\mathbf{r}_l - \mathbf{r}')$$ (5.16)

where

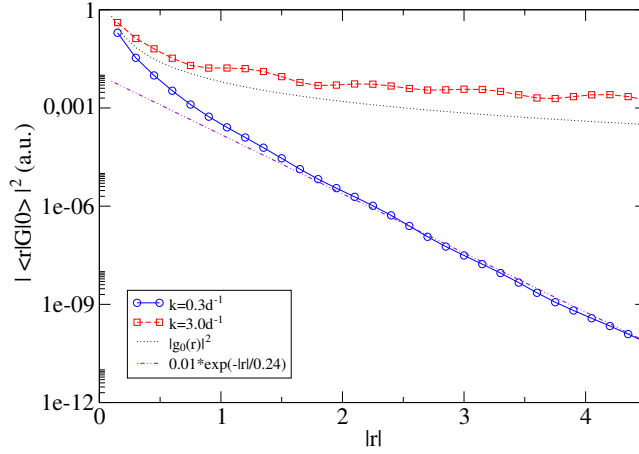$$M = \frac{\mathrm{I}}{a_{\text{eff}}} + M^\infty$$ (5.17)

Figure 5.4: Decay of the Green's function as a function of the distance from the center of the cloud of scatterers, averaged over 100 different realizations of the random potential. The ≈ 4600 scatterers ($a_{\text{eff}} = 0.3d$) are distributed in a cubic box of side $21d$, occupying each site of the lattice with $p = 50\%$.

is a $N \times N$ matrix, I the identity matrix and M^{∞} a symmetric matrix with elements defined by

$$M_{jl}^{\infty} = \begin{cases} \exp\left(ik\left|\mathbf{r}_j - \mathbf{r}_l\right|\right)/\left|\mathbf{r}_j - \mathbf{r}_l\right| & \text{if } j \neq l, \\ ik & \text{if } j = l. \end{cases} \tag{5.18}$$

The *exact* calculation of the resolvent in coordinates space is in this way reduced to the inversion of a complex symmetric (not hermitian) $N \times N$ matrix. We have implemented the criterion by Kramer and MacKinnon, and indeed we found an exponential decay of $|\langle \mathbf{r} | \mathcal{G} | \mathbf{r}' \rangle|^2$ for sufficiently small energies, as shown in Fig. 5.4.

However, as we shall demonstrate, this rapid decay may not be due to localization, but to the fact that the energy E is in a spectral gap of the system [34].

To prove this statement, we have enclosed our lattice of scatterers in a box of side L, imposing periodic boundary conditions on the walls of the box. This amounts to replacing Eq. (5.13) by the particle propagator satisfying the correct boundary conditions[2]:

$$g_0^{\text{Box}}(\mathbf{r}) = \frac{2m}{\hbar^2 L^3} \sum_{\mathbf{q}} \frac{e^{i\mathbf{q}\cdot\mathbf{r}}}{k^2 - \mathbf{q}^2}, \tag{5.19}$$

with $\mathbf{q} = 2\pi\mathbf{n}/L$ and $\mathbf{n} \in \mathbb{Z}^3$ (a triplet of integers). Indeed we found that, for the ensemble of scatterers used in Fig. 5.4, the ground state of the system, once enclosed in a box of side $L = 23d$ (slightly larger than the scattering medium), is characterized by a wave number $k_{\min} = 0.7202d^{-1}$. The exponential decay

---

[2]The summation must be performed numerically and its convergence is very slow, since $\sum_{\mathbf{q}} \mathbf{q}^{-2} \sim \int \mathrm{d}q\, O(1)$: to evaluate it efficiently, we manipulated algebraically Eq. (5.19) as shown in Appendix C.

shown at $k = 0.3d^{-1}$ by $|\langle \mathbf{r}\, |\mathcal{G}|\, \mathbf{r}' \rangle|^2$ is therefore simply indicating that at such low energy no state can exist deep inside the medium. In a scattering experiment, we might imagine a plane wave coming from infinity that scatters on the trapped B atoms: if $k < k_{\min}$ the incoming wave undergoes total reflection, and inside the random medium only penetrates an evanescent wave, that decays exponentially from the boundary of the medium towards its interior. This example clearly points out that an exponential decay of $|\langle \mathbf{r}\, |\mathcal{G}|\, \mathbf{r}' \rangle|^2$ is not a sufficient criterion to prove localization in our system, since it does not guarantee the existence of states deep inside the random potential.

5.2.2 Direct imaging of the states

The most direct way to prove localization seems to exhibit stationary states that are 'localized' inside the disordered potential, that is with a wave function strongly peaked inside the scattering medium, decreasing exponentially towards the borders of the scattering medium. To this end, we use the fact that the wave function

$$\phi(\mathbf{r}; \mathbf{r}_0) \equiv \mathrm{Im}\, \langle \mathbf{r}|\mathcal{G}(E + i0^+)|\mathbf{r}_0 \rangle, \tag{5.20}$$

when not identically zero, is an exact eigenstate[3] of $\mathcal{H}$ with energy E, whatever the arbitrary location of its center $\mathbf{r}_0$. Here we take $E > 0$ so that $\phi(\mathbf{r}; \mathbf{r}_0)$ belongs to the continuum of the energy spectrum of $\mathcal{H}$, like the scattering states.

In the remaining part of this Section, we will present numerical results obtained for a single realization of a random potential containing ≈ 900 scatterers that occupy the nodes of a cubic lattice with 21 sites/side, $\{\mathbf{r}_j\}/d \in [-10 : 10]^3$, with a filling factor $p = 10\%$ (unless otherwise stated). The discussed features do not however depend on this specific realization.

In Fig. 5.5 we plot the square of the amplitude of ϕ inside the scattering medium, normalized to its value outside, as a function of the wave number k of the matter wave. In order to avoid a choice that would break symmetry we plot $\phi_{\mathrm{in}}^2/\phi_{\mathrm{out}}^2$, where both numerator and denominator are averaged over a few points. We define ϕ_{in}^2 as the average of the 6 values $\phi^2(\mathbf{r}_{\mathrm{in}}; \mathbf{r}_{\mathrm{in}})$, with $\mathbf{r}_{\mathrm{in}}$ chosen between the 6 values $\{(0.5, 0, 0), (-0.5, 0, 0), \text{ and cyclic permutations}\}$. Similarly, we define ϕ_{out}^2 as the average of the 36 values $\phi^2(\mathbf{r}_{\mathrm{out}}; \mathbf{r}_{\mathrm{in}})$, with $\mathbf{r}_{\mathrm{out}}$ chosen between the 6 values $\{(15, 0, 0), (-15, 0, 0), \text{ and cyclic permutations}\}$, and $\mathbf{r}_{\mathrm{in}}$ as before. The graph reveals extremely narrow peaks, corresponding to narrow energy intervals where the matter wave can significantly penetrate the scattering medium.

It remains to be checked that, at these penetrating energies, the wave function is well localized inside the scattering medium. This we have verified for a large number of energy peaks. Since the stationary wave function $\phi(\mathbf{r}; \mathbf{r}_0)$ generally diverges as $|\mathbf{r} - \mathbf{r}_j|^{-1}$ for $\mathbf{r}$ tending to the position $\mathbf{r}_j$ of a scatterer, as imposed by the contact potential, we introduce for each lattice node the coarse grained density distribution

$$\bar{\rho}(\mathbf{r} \in \text{lattice nodes}) = \int_{[-d/2, d/2]^3} d\mathbf{u}\, |\phi(\mathbf{r} + \mathbf{u}; \mathbf{r}_0)|^2 \tag{5.21}$$

---

[3]Let $|\chi\rangle \equiv \mathcal{G}(E + i\eta)|\mathbf{r}_0\rangle$. By definition of $\mathcal{G}$,

$$(E + i\eta - \mathcal{H})\chi(\mathbf{r}) = \delta\,(\mathbf{r} - \mathbf{r}_0)\,.$$

Taking the limit $\eta \to 0^+$ of the imaginary part in the latter equation leads to $\mathcal{H}\phi = E\phi$.
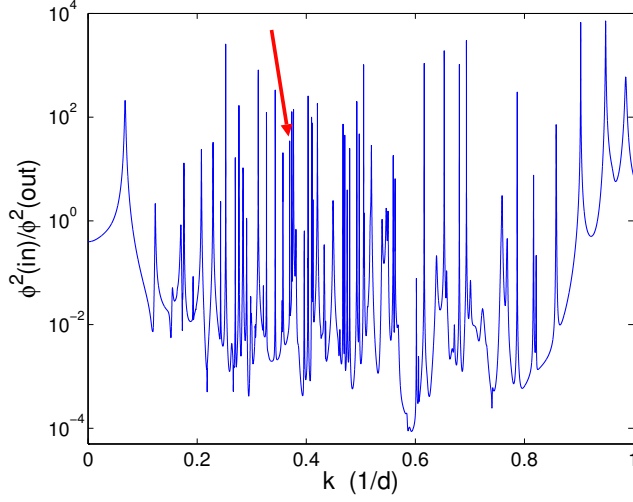
Figure 5.5: Average value of ϕ^2 in the center of the scattering medium, normalized to its value outside (see the text for details) as a function of $k = (2m_A E)^{1/2}/\hbar$, with $a_{\mathrm{eff}} = d$, for a given realization of the disorder with $N \approx 900$ scatterers. The energy intervals where the matter wave significantly penetrates the scattering medium correspond to the narrow peaks in this figure. The oblique arrow indicates the peak chosen in Fig. 5.6 to show that the wave function is actually spatially localized in these energy intervals.
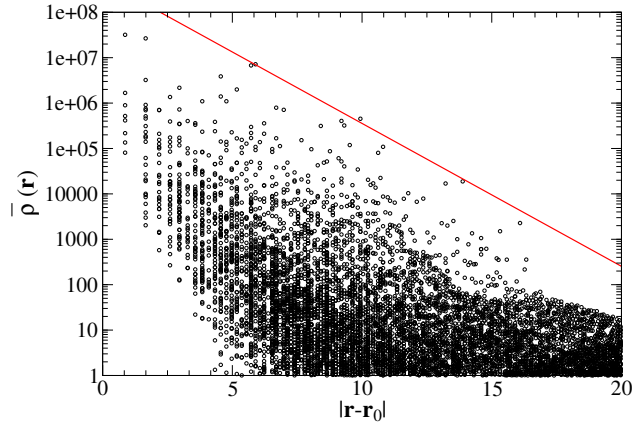

Figure 5.6: Plot of the coarse grained distribution $\bar{\rho}(\mathbf{r})$ as a function of the distance $|\mathbf{r} - \mathbf{r}_0|$, for a randomly selected energy peak in Fig. 5.5. This reveals a localized state, whose amplitude decreases roughly exponentially towards the borders of the scattering medium. It is centered at $\mathbf{r}_0/d = (0.5, -0.5, -3.5)$ and we have set $a_{\mathrm{eff}} = d$. The red line is an exponential fit, that gives a localization length $\xi_{\mathrm{loc}} \sim 1.4d$. The realization of the disorder is the same as the one used in Fig. 5.5, and the corresponding peak is marked by an arrow in Fig. 5.5: it is centered at $k = 0.3695215\,d^{-1}$ and has a half-width $\Delta k = 3 \times 10^{-5}\,d^{-1}$.
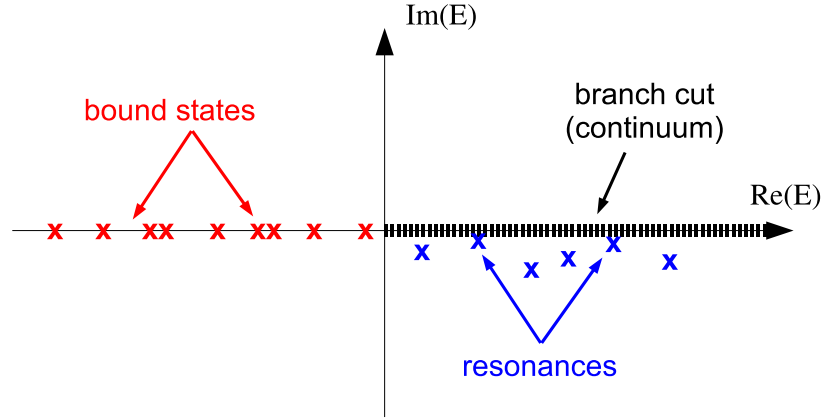
Figure 5.7: Poles of the analytic continuation of the resolvent $\mathcal{G} = (E + i0^+ - \mathcal{H})^{-1}$ in the complex energy plane. For bizarre or random potentials, in addition to the poles lying on the $\text{Re}(E)$ axis the resolvent may present a discrete set of poles in the fourth quadrant: the associated states are the resonances of the system.

obtained by integrating the modulus squared of ϕ over the unit cell of the lattice around each lattice site. In practice, for a given energy E, the arbitrary position $\mathbf{r}_0$ is chosen numerically inside the scattering medium, on a lattice shifted with respect to the one containing the scatterers, so that the coarse grained distribution $\bar{\rho}$ is maximal in the lattice cell containing the point $\mathbf{r}_0$. In Fig. 5.6 we plot the coarse grained density profile of ϕ for an energy corresponding to a randomly chosen peak in Fig. 5.5: this indeed corresponds to a spatially localized state. An exponential fit gives a tail of $\bar{\rho}(\mathbf{r})$ decreasing as $e^{-|\mathbf{r}-\mathbf{r}_0|/\xi_{\text{loc}}}$, where the localization length ξ_{loc} is $\approx 1.4d$. Such a small value for the localization length could seem strange at first glance for a typical physical state, and has indeed a numerical origin. A quick estimate shows that, requiring a state centered on $\mathbf{r} = (0, 0, 0)$ to decay significantly (let us say at least 3 orders of magnitude) in each spatial direction along a lattice of scatterers with half-side of $10d$, i.e. $e^{-10d/\xi_{\text{loc}}} = 0.001$, one obtains indeed the condition $\xi_{\text{loc}} \lesssim 1.5d$. The inversion of large matrices is a very time- and resource-consuming calculation, and we are unfortunately unable at present to investigate much larger configurations. This numerical limitation does not affect in any way the validity of the results presented here, and we expect larger localization lengths for bigger scattering samples (i.e. for larger number of B particles).

After this first brute force exploration of the problem, we interpret the multi-peaked structure of Fig. 5.5 in terms of the properties of the resolvent $\mathcal{G} = (E + i0^+ - \mathcal{H})^{-1}$ (see Fig. 5.7). Its isolated poles at negative energies correspond to true bound states of the potential, while at positive energies the poles form a branch cut and correspond to the continuum of scattering states. Due to the boundary conditions that we have imposed (i.e. the infinitesimal $i0^+$ in the denominator of $\mathcal{G}$, that guarantees that only outgoing waves are present in the scattered wave), its analytic continuation to complex energies is regular in the

upper half-plane, but may have a set of discrete poles along the lower rim of the positive $\mathrm{Re}(E)$ axis: to each of these poles there is associated a *resonance*, i.e. a state with a probability density decaying as $\approx \mathrm{e}^{2\mathrm{Im}(E)t}$ and therefore a finite lifetime $1/\Gamma$ proportional to the inverse of the imaginary part of its energy,

$$\frac{1}{\Gamma} = -\frac{\hbar}{2\mathrm{Im}(E)}. \tag{5.22}$$

If a localized state exists in our model, it must have a finite lifetime since we are considering a scattering medium with a finite spatial extension: the tails of the localized wave function, even if exponentially decaying, always reach the boundary of the scattering medium, allowing the state to escape after a finite time. A localized state must therefore correspond to one of these resonances. The imaginary parts of the energy of the poles go to zero exponentially with the linear size of the disordered medium, so that in the limit of disorder with infinite extension the localized states become eigenstates of the Hamiltonian with real energy and infinite lifetime. Strictly speaking, since we consider disorder with a finite extension, the states we find are not "localized". Indeed, the exponential decrease of their envelope stops outside the scattering medium, and the states are not square-integrable. Nonetheless, for any practical purpose these can be considered as localized if their density presents a sufficient decrease or, equivalently, if their lifetime is sufficiently long on the timescale of the experience.

In Fig. 5.5 the wave number k is swept along the branch cut, and we expect a close connection between the narrow peaks and the poles of $\mathcal{G}$: in particular, a spike should appear each time k passes above a resonance (the closer is the pole to the lower rim of the x-axis, the more pronounced will be the spike). As we will see in the following Sec. 5.2.3, however, it is in general a non trivial numerical task to find the positions of a large number of poles of $\mathcal{G}$ in the complex plane. Fortunately, we are interested here only in the poles of $\mathcal{G}$ that are extremely close to the real axis. We then expect that these poles leave signatures on the real axis, in the form of purely imaginary eigenvalues of the matrix M, defined in Eq. (5.17), with an extremely small modulus, for values of the energy $E = \hbar^2 k^2/2m_A$ close to the real part of the poles. As opposed to the poles of $\mathcal{G}$, the eigenvalues of M can be calculated in a straightforward manner, and in Fig. 5.8 these are shown as a function of the incoming wave number k (for two different realizations of the disorder, in the left and right columns respectively). We observe that, as the incoming wave number k decreases below the inverse of the mean distance between the scatterers $\bar{k} = p^{1/3}/d$, a large number of eigenvalues acquire an extremely small imaginary part and accumulate in the region $Re(\lambda) \sim -\bar{k}$ [74]. We expect that, as k is varied, a spike appears in Fig. 5.5 as one of the eigenvalues with sufficiently small imaginary part crosses the $\mathrm{Re}(\lambda) = 0$ axis in Fig. 5.8. Indeed, we have confirmed numerically on a large number of peaks the correspondence between eigenvalues of M crossing the $\mathrm{Re}(E) = 0$ axis and spikes.

It is interesting to note that a_{eff} enters in the eigenvalues of M only in the simple form $\lambda_i = [1/a_{\mathrm{eff}} + \mathrm{Re}(\lambda_i^\infty)] + \mathrm{Im}(\lambda_i^\infty)$, where $\{\lambda_i^\infty\}$ are the eigenvalues of M^∞, as can be seen explicitly in Eq. (5.17). As we will show in the next Section, a_{eff} is a function of the two dimensionless ratios a/a_{ho} and m_B/m_A, and in an experiment a_{eff} might be easily tuned by making use of a Feshbach resonance to modify the free-space scattering length a (or by changing the wavelength of the lattice to modify a_{ho}). This suggests choosing $a_{\mathrm{eff}} \sim 1/\bar{k}$ to shift the
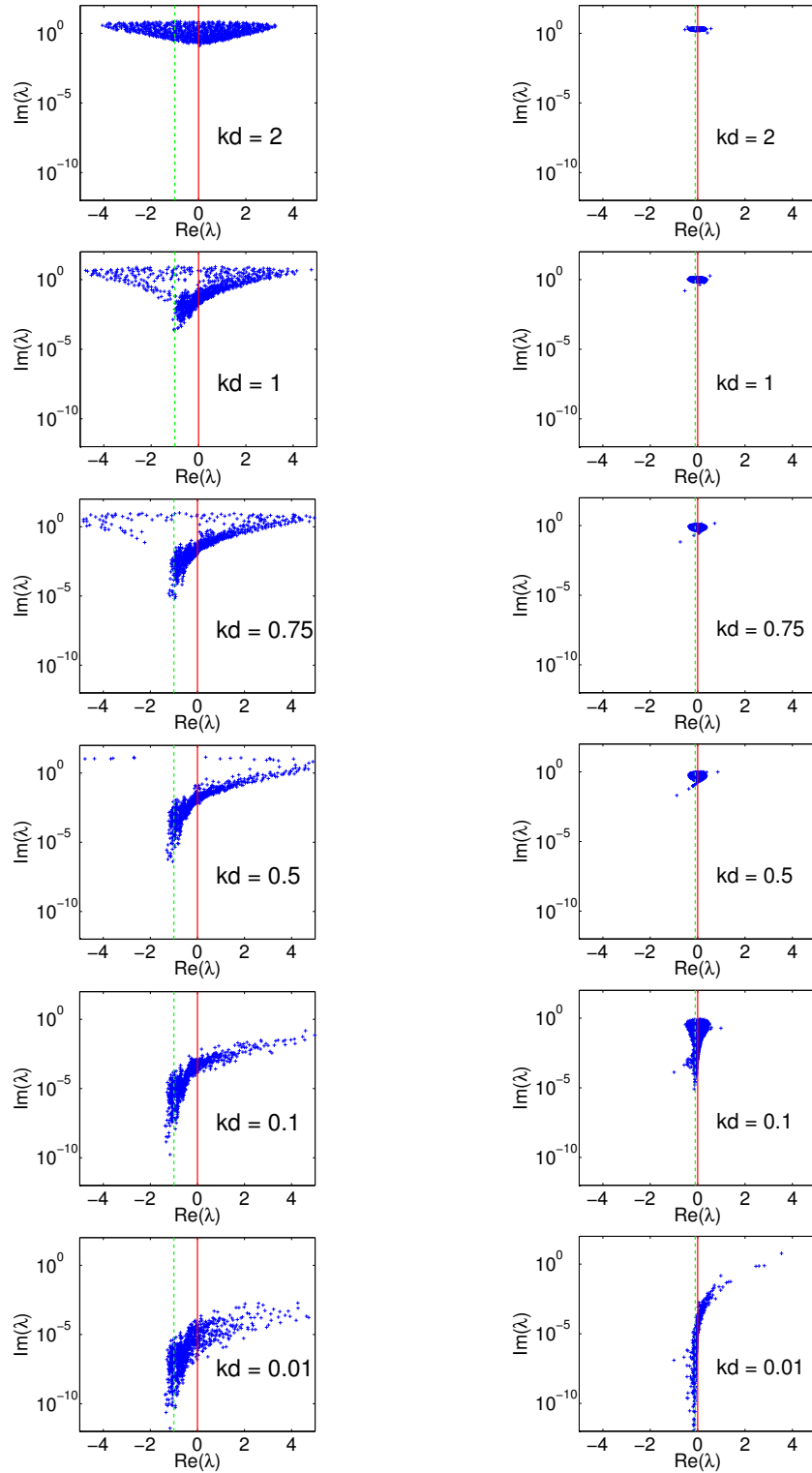
Figure 5.8: Real and imaginary parts (x and y axis, respectively) of the eigenvalues of M^∞ (i.e. of M with $a_{\text{eff}} = \infty$) for different values of the wave number k of the matter wave (units of $1/d$). Left column: cubic lattice with 21 sites/side, $p = 10\%$ and 872 scatterers, $\bar{k}d = 0.5$ (same as in Figs. 5.5 and 5.6). Right column: cubic lattice with 209 sites/side, $p = 0.01\%$ and 878 scatterers, $\bar{k}d = 0.05$. The eigenvalues of M with another value of a_{eff} are obtained by an horizontal displacement, $\lambda_i = [1/a_{\text{eff}} + \text{Re}(\lambda_i^\infty)] + \text{Im}(\lambda_i^\infty)$. The green dashed lines mark the values $\text{Re}(\lambda) = -1/d$ (left) and $\text{Re}(\lambda) = -0.1/d$ (right), respectively.

$\text{Re}(\lambda) = 0$ axis in the middle of the cloud of eigenvalues (see the green dashed lines in Fig. 5.8): as k decreases below $\bar{k}$, one finds in this way a very large number of eigenvalues with modulus extremely close to 0, i.e. "almost-zeros" of the determinant of M. Each of these eigenvalues will provide a spike in Fig. 5.5 as it crosses the $\text{Re}(\lambda) = 0$ axis. Seen from another point of view, each of these eigenvalues can be transformed into a true zero of $\det(M)$, i.e. a pole of the resolvent, by the addition of a small negative imaginary part to its energy (see Fig. 5.7).

5.2.3   Lifetime of the most localized state

The lifetime of localized states is expected to increase exponentially with the size of the system. To check whether our system shows such a feature, we allow k to have an imaginary part and use a variant of Newton's method to find a zero of the determinant of M. We proceed as follows:

1. Start with a real value of $k = k_0$, calculate the eigenvalues of M^∞, and set $a = a_0 = -1/\text{Re}(\lambda_0)$, where λ_0 is the eigenvalue of M^∞ with smallest imaginary part, in order to give vanishing real part to λ_0.

2. Set $M = 1/a_i + M^\infty$ and add a small complex shift to the momentum, $k_{i+1} = k_i + \alpha \cdot \delta k$, where δk is given by Newton's method[4] and $\alpha(k_0) > 1$ is an empirical factor inserted in order to accelerate convergence.

3. Calculate the eigenvalues of the new matrix M, and set to zero the real part of λ_0 imposing $1/a_{i+1} = 1/a_i - \text{Re}(\lambda_0)$ (where λ_0 is the eigenvalue of M with smallest imaginary part).

4. Repeat steps 2 and 3 until convergence.

This scheme converges for small enough initial momenta ($k \lesssim \bar{k}$), and in Fig. (5.9) we show the behavior of the imaginary part of the energy for the pole of the resolvent with smallest $|\text{Im}(E)|$: as expected, the lifetime of the state associated to this pole grows exponentially with the linear size of the scattering medium.

Our scheme unfortunately converges only to a single pole per given spatial configuration of the random potential, and does not allow us to investigate the lifetimes of the other localized states. With this method we can prove that *one* state is localized, but this may not convince a sceptic of the presence of Anderson localization in our system. Indeed, as we have shown in Fig. 5.1, even non-random potentials can support localized states. What is peculiar about the

---

[4]Newton's method to solve the equation $\det[M(k)] = 0$: by iteration, find $k_{i+1} = k_i + \delta k$ that gives

$$0 = \det \left[M(k_i) + \delta k \left. \frac{\partial M}{\partial k} \right|_{k=k_i} \right] = \det \left[M(k_i) \right] \det \left[I + \delta k \cdot M^{-1}(k_i) \left. \frac{\partial M}{\partial k} \right|_{k=k_i} \right].$$

The desired value of the shift is given by

$$\delta k = - \frac{1}{\text{Tr} \left[M^{-1}(k_i) \left. \frac{\partial M}{\partial k} \right|_{k=k_i} \right]}.$$

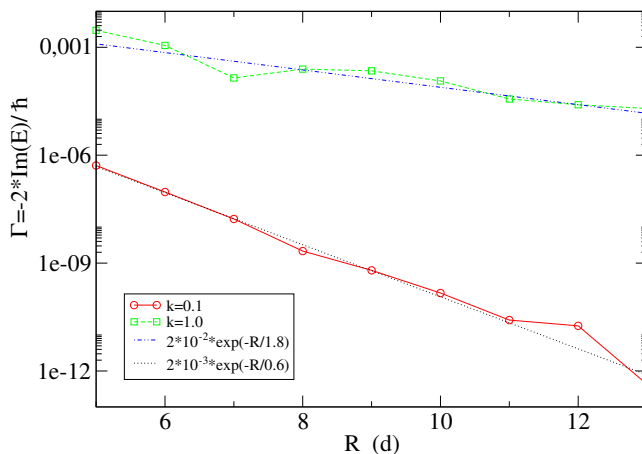The method converges only if $\det[M(k_0)]$ is sufficiently small.

Figure 5.9: Imaginary part of the energy of the pole of the resolvent with smallest $|\mathrm{Im}(E)|$ as a function of the linear size of the system, averaged over 5 realizations. Cubic lattice of half-side R populated by scatterers with $p = 10\%$ and $a_{\mathrm{eff}} \approx d$. The y-axis is in units of $8\nu_r^A/\pi$, where the recoil frequency is $\nu_r^A = E_r^A/h$.

Anderson transition in 3D is that, above a certain disorder threshold, a *massive* number of states becomes localized. This is clearly shown by the analysis performed in the latter Sec. 5.2.2, where we have been able to put in evidence the presence of many localized states for a sufficiently strong coupling between the matter wave and the trapped scatterers. In the following Section we will show that arbitrary large coupling constants can indeed be realized.

5.3 Effective interaction

We will solve here the two-body problem of a free atom A scattering on a single trapped particle B, and derive the coupling constant g_{eff} introduced in Eq. (5.41). The particle B is found in the ground state of its micro-well before the interaction with A. To ensure elastic scattering, we assume that collisions between A and B happen at an energy that is low enough to leave the B in the ground state of its micro-well at the end of the scattering event. Approximating each micro-well of the lattice by an harmonic potential of frequency ω, we require the kinetic energy of the matter wave to be small compared to the level spacing of the trapping potential: this is expressed in Eq. (5.4), or equivalently by

$$ka_{\mathrm{ho}}\sqrt{\frac{m_B}{m_A}} \ll 1, \qquad (5.23)$$

where k is the wave number of the A atoms and $a_{\mathrm{ho}} = \sqrt{\hbar/m_B\omega} \approx \sqrt[4]{E_r^B/V_0^B}\,d/\pi$ is the harmonic-oscillator length, $\approx 50\,$nm for the optical lattice considered.

The Hamiltonian in the absence of interactions,

$$H_0 = -\frac{\hbar^2\Delta_A}{2m_A} - \frac{\hbar^2\Delta_B}{2m_B} + \frac{1}{2}m_B\omega^2 r_B^2, \qquad (5.24)$$

admits the s-wave solution

$$\psi_0(\mathbf{r}_A, \mathbf{r}_B) = \langle \mathbf{r}_A, \mathbf{r}_B | \psi_{\mathbf{k},0} \rangle = \frac{\sin(kr_A)}{kr_A} \phi_0(r_B). \qquad (5.25)$$

The latter represents a spherical matter wave (A) of wave vector k and a particle (B) in the ground state of the harmonic potential, $\phi_0(r_B) = \exp(-r_B^2/2a_{\mathrm{ho}}^2)/\left(\sqrt{\pi}a_{\mathrm{ho}}\right)^{3/2}$, and has an energy $E = \hbar^2 k^2/2m_A + 3\hbar\omega/2$. We model the A-B interaction with a regularized contact potential,

$$H = H_0 + g\delta(\mathbf{r}_A - \mathbf{r}_B)\frac{\partial}{\partial|\mathbf{r}_A - \mathbf{r}_B|}\left(|\mathbf{r}_A - \mathbf{r}_B|\dots\right), \qquad (5.26)$$

the coupling constant g being expressed in terms of the reduced mass $\mu = m_A m_B/(m_A + m_B)$ and the free-space scattering length a (relative to the A-B collision in the absence of the trapping potential) by

$$g = \frac{2\pi\hbar^2 a}{\mu}. \qquad (5.27)$$

The Schrödinger equation $H\psi = E\psi$ can be reformulated equivalently in the integral form

$$\psi(\mathbf{r}_A, \mathbf{r}_B) = \psi_0(\mathbf{r}_A, \mathbf{r}_B) + g\int \mathrm{d}\boldsymbol{\rho}\, G_E(\mathbf{r}_A, \mathbf{r}_B; \boldsymbol{\rho}, \boldsymbol{\rho})\psi_{\mathrm{reg}}(\rho) \qquad (5.28)$$

in terms of the two-particle retarded Green's function for the non-interacting Hamiltonian

$$G_E = \frac{1}{E + i0^+ - H_0} \qquad (5.29)$$

and the regularized part of the two-particle wave function,

$$\psi_{\mathrm{reg}}(\mathbf{R}) = \left.\frac{\partial}{\partial|\mathbf{r}_A - \mathbf{r}_B|}\left[|\mathbf{r}_A - \mathbf{r}_B|\psi\left(\mathbf{r}_A, \mathbf{r}_B\right)\right]\right|_{\mathbf{r}_A = \mathbf{r}_B} \qquad (5.30)$$

where $\mathbf{R} = (\mathbf{r}_A + \mathbf{r}_B)/2$ and $\psi_{\mathrm{reg}}(\mathbf{R}) = \psi_{\mathrm{reg}}(R)$ since we consider s-wave scattering only. Inverting Eq. (5.28), we find that the regularized part of the wave function satisfies an equation of the form

$$\tilde{\psi}_{\mathrm{reg}} = \frac{I}{I - g\hat{O}}\tilde{\psi}_0, \qquad (5.31)$$

where $\hat{O}$ is an integral operator, and $\tilde{\psi}(R) = R\psi(R)$. The detailed derivation of this equation and the explicit form of $\hat{O}$ are presented in Appendix D.

The integral formulation of the Schrödinger equation is useful to derive an effective interaction that in the low energy limit describes the A-B collision in terms of a simple contact interaction. In order to see how, we expand G_E on the basis of eigenstates of H_0,

$$G_E = \int \frac{\mathrm{d}\mathbf{k}'}{(2\pi)^3} \sum_{\mathbf{n}} \frac{|\psi_{\mathbf{k}',\mathbf{n}}\rangle \langle \psi_{\mathbf{k}',\mathbf{n}}|}{E + i0^+ - E_{\mathbf{k}',\mathbf{n}}}, \qquad (5.32)$$

and project it in position space to obtain

$$G_E(\mathbf{r}_A, \mathbf{r}_B; \boldsymbol{\rho}, \boldsymbol{\rho}) = \frac{2m_A}{\hbar^2} \left[-\frac{e^{ik|\mathbf{r}_A - \boldsymbol{\rho}|}}{4\pi |\mathbf{r}_A - \boldsymbol{\rho}|} \phi_0(\mathbf{r}_B)\phi_0(\boldsymbol{\rho}) \right.$$

$$\left. - \sum_{\mathbf{n} \neq 0} \frac{e^{-\kappa_{\mathbf{n}}|\mathbf{r}_A - \boldsymbol{\rho}|}}{4\pi |\mathbf{r}_A - \boldsymbol{\rho}|} \phi_{\mathbf{n}}(\mathbf{r}_B)\phi_{\mathbf{n}}(\boldsymbol{\rho}) \right] . \quad (5.33)$$

Under the low-energy assumption (5.4),

$$-\frac{\hbar^2 \kappa_{\mathbf{n}}^2}{2m_A} = \frac{\hbar^2 k^2}{2m_A} - \hbar\omega \left(n_x + n_y + n_z \right) < 0 \text{ for every } \mathbf{n} \neq 0.$$

As a consequence, the terms of Eq. (5.33) involving excited states of the harmonic oscillator give exponentially vanishing contributions and can be neglected when A is far away from the center of the harmonic well. Expanding $|\mathbf{r}_A - \boldsymbol{\rho}| \simeq r_A - \boldsymbol{\rho} \cdot \mathbf{r}_A / r_A$, averaging over the direction of $\mathbf{r}_A$ and substituting into Eq. (5.28), we get

$$\psi(\mathbf{r}_A, \mathbf{r}_B) \stackrel{r_A \to \infty}{\simeq}$$

$$\left[\frac{\sin(kr_A)}{kr_A} - a\frac{m_A}{\mu}\frac{\exp(ikr_A)}{r_A} \int \mathrm{d}\boldsymbol{\rho} \, \frac{\sin(k\rho)}{k\rho} \phi_0(\rho)\psi_{\mathrm{reg}}(\rho) \right] \phi_0(r_B). \quad (5.34)$$

We know that the scattering solution (5.28) can generally be written as

$$\psi(\mathbf{r}_A, \mathbf{r}_B) \stackrel{r_A \to \infty}{\simeq} \left[\frac{\sin(kr_A)}{kr_A} + f_k\frac{\exp(ikr_A)}{r_A} \right] \phi_0(r_B), \quad (5.35)$$

the factorized form being ensured by the low-energy scattering condition (5.4). Comparing (5.34) and (5.35), we obtain the scattering amplitude

$$f_k = -a\frac{m_A}{\mu} \int \mathrm{d}\boldsymbol{\rho} \, \frac{\sin(k\rho)}{k\rho} \phi_0(\rho)\psi_{\mathrm{reg}}(\rho). \quad (5.36)$$

In the limit of zero-energy, the scattering amplitude defines the *effective scattering length* a_{eff} through

$$a_{\mathrm{eff}} \equiv -\lim_{k \to 0} f_k = a\frac{m_A}{\mu} \int \mathrm{d}\boldsymbol{\rho} \, \phi_0(\rho)\psi_{\mathrm{reg}}(\rho). \quad (5.37)$$

For low but non-zero energy, the effective range r_e of the effective interaction is obtained by inverting Eq. (2.36),

$$r_e = \frac{2}{k^2} \left[Re\left(\frac{1}{f_k}\right) + \frac{1}{a_{\mathrm{eff}}} \right]. \quad (5.38)$$

As seen in Chap. 2, a contact potential has strictly vanishing effective range, and can be used consistently to replace a more complex two-body potential only if the effective range correction is negligible, i.e. only if

$$kr_e \ll 1. \quad (5.39)$$

We will see in the following that generally $r_e \approx a_{\mathrm{ho}}$, and the latter condition usually reduces to the one for elastic scattering, Eq. (5.23).

Under the low-energy conditions stated in Eqs. (5.4) and (5.39), the collision between the free particle A and the particle B, trapped in a harmonic well centered around $\mathbf{r}_j$, can be completely described in terms of the following effective interaction acting on the free particle A:

$$V_{\mathrm{eff,j}}(\mathbf{r}) = g_{\mathrm{eff}} \delta(\mathbf{r} - \mathbf{r}_j) \frac{\partial}{\partial |\mathbf{r} - \mathbf{r}_j|} \left(|\mathbf{r} - \mathbf{r}_j| \ldots \right). \tag{5.40}$$

The coupling constant of the effective interaction is

$$g_{\mathrm{eff}} = \frac{2\pi \hbar^2 a_{\mathrm{eff}}}{m_A}, \tag{5.41}$$

where a_{eff} is given in Eq. (5.37) and we have m_A rather than μ in the denominator since we consider the collision of A with a static potential.

As seen in Eq. (5.37), the effective scattering length a_{eff} depends explicitly on the regularized wave function, which in turn is the solution of an integral equation, Eq. (5.31). The latter must be solved numerically, but analytical results may be extracted in the limit of weak trapping $\omega \ll (1 + m_A/m_B)^{-2} \hbar/m_A a^2$ (or equivalently $a_{\mathrm{ho}}/|a| \gg (1 + m_A/m_B)\sqrt{m_A/m_B}$), where an expansion to lowest order of (5.31) gives $\tilde{\psi}_{\mathrm{reg}} = \tilde{\psi}_0$ (so-called Born approximation) and

$$a_{\mathrm{eff,Born}} = a \frac{m_A}{\mu}. \tag{5.42}$$

When the trapping is very weak, the B particle is almost free and the effective coupling constant g_{eff} correctly reduces to g, the coupling constant in free space, given in Eq. (5.27). In the same limit, an expansion of the scattering amplitude for small energies gives the effective range for the interaction:

$$r_{e,\mathrm{Born}} = -\frac{\mu}{m_A} \frac{a_{\mathrm{ho}}^2}{a}. \tag{5.43}$$

We have solved numerically Eq. (5.37), and in Figs. 5.10-5.12 we plot a_{eff} as a function of $1/a$ for different values of m_B/m_A. We choose $m_B/m_A = 0.15, 1, 6.67$, corresponding to the physical cases of a mixture of ^{6}Li (B) and ^{40}K (A), a mixture of two different internal states of atoms of the same species, and a mixture of ^{40}K (B) and ^{6}Li (A), respectively. In Figs. 5.11 and 5.13 we also plot the behavior of the effective range in the case $m_B = m_A$: r_e is generally of order a_{ho}, but diverges when $a_{\mathrm{eff}} \to 0$, as explained in Sec. 2.1.

The effective coupling constant shows an infinite set of resonances due to the presence of the external confinement. A similar effect, termed confinement-induced resonance (CIR), has been been analyzed theoretically in 1D wave guides [75, 76, 77], in 3D optical lattices [79], and in quasi-2D condensates [78]. In 1D wave guides the effect is particularly marked: due to the presence of the transverse confinement, a contact potential acquires a bound state for any value of the 3D scattering length (while in free space it is well known that a contact potential has a bound state only for $a > 0$). Confinement-induced modifications of two-body scattering properties have very recently been observed experimentally by the Zürich group in 1D waveguides [80] and in 3D optical lattices [81]. In most of the cited articles, the underlying translational symmetry
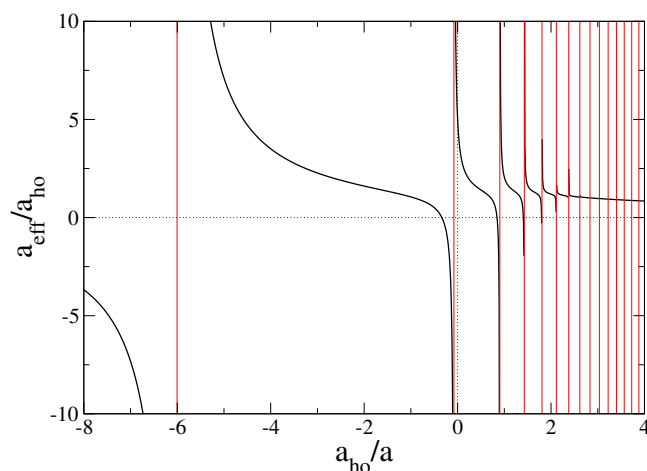
Figure 5.10: Effective scattering length a_{eff} (continuous line) as a function of a^{-1} for $m_B/m_A = 0.15$ (trapped ^{6}Li and free ^{40}K). The vertical lines (red) mark the positions of the resonances (a step of $a_{\text{ho}}/a = 0.01$ is used to sample the curves, and some of the resonances are too narrow to be seen on the graph).

and the harmonic nature of the confinement allow for the factorization of the center-of-mass motion: this in turn implies that a single CIR can exist in such systems, since only one state in the closed channel is coupled to the open channel [76]. When this factorization is not possible, as in our setup or in the case of a 1D wave guide with anharmonic transverse confinement [77], an infinite set of states in the closed channel has non-zero overlap with the open one, and an infinite number of resonances appears. In practice however only a few of them may be resolved and relevant in an experiment since they become increasingly sharper as a_{ho}/a becomes larger.

5.3.1 Resonances of the effective scattering length

The resolvent G_E is purely real in the limit $k \to 0$ [see Eq. (5.33)]: $\hat{O}$ turns out to be real and symmetric, and all its eigenvalues $\{\lambda_i\}$ are as a consequence real as well. This means that a resonance in a_{eff} is expected whenever the denominator of Eq. (5.31) vanishes, i.e. whenever the free space scattering length a equals $\mu/2\pi\hbar^2\lambda_i$. These resonances have different origins, depending on the sign of a.

5.3.1.1 Positive a

When $a > 0$, the pseudopotential admits a bound state in which the two particles can "sit" for a variable time, forming a molecule that oscillates in the harmonic well. To understand this point, we rewrite the two-body Hamiltonian (5.26) as

$$-\frac{\hbar^2\Delta_R}{2(m_A + m_B)} + \frac{1}{2}m_B\omega^2 R^2 - \frac{\hbar^2\Delta_r}{2\mu} + g \cdot \delta(\mathbf{r}) \cdot \frac{\partial}{\partial r}r$$
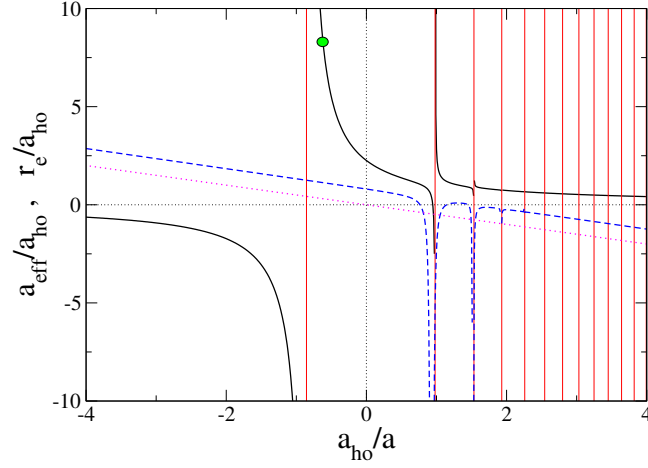$$+ \left[\frac{1}{8}m_B\omega^2 r^2 - \frac{1}{2}m_B\omega^2\mathbf{R}\cdot\mathbf{r}\right], \quad (5.44)$$

Figure 5.11: Same as Fig. 5.10 for two particles of equal mass. The blue dashed line is the effective range r_e, and the magenta dotted line is $r_{e,\mathrm{Born}}$, Eq. (5.43). A green dot at $a = -1.6a_{\mathrm{ho}}$ marks the position where $a_{\mathrm{eff}} \approx d$ if $V_0^B = 50E_r^B$.
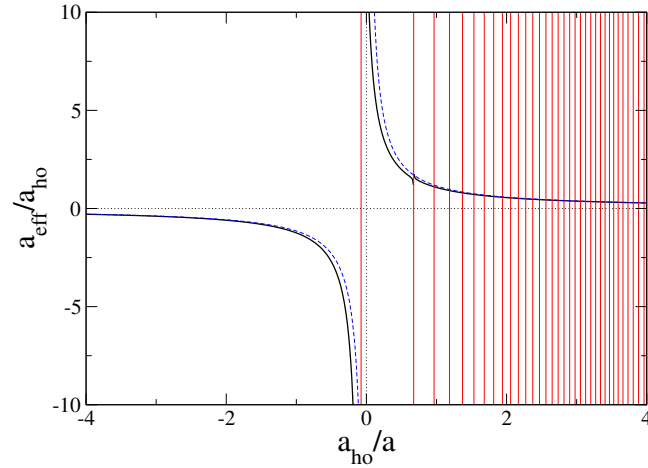

Figure 5.12: Same as Fig. 5.10 for $m_B/m_A = 6.67$ (trapped ^{40}K and free ^{6}Li). The dashed line is $a_{\mathrm{eff,Born}}$, Eq. (5.42).
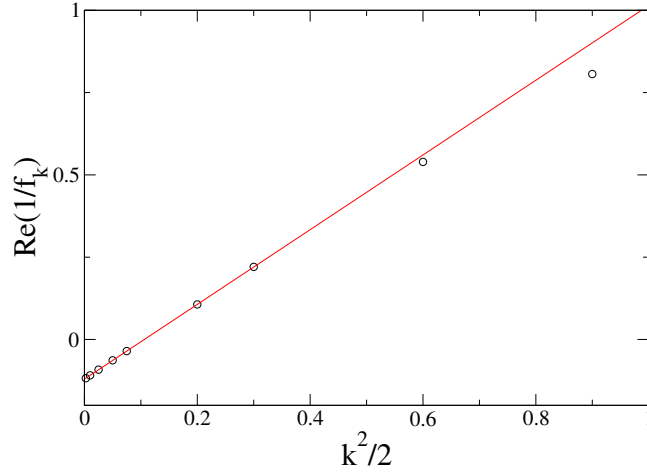
Figure 5.13: Energy dependence of the scattering amplitude for two particles of equal mass at $a = -1.6a_{\text{ho}}$ (green marker in Fig. 5.11). The linear fit at low energy, $Re(1/f_k) = -1/a_{\text{eff}} + r_e k^2/2$, yields $r_e = 1.135a_{\text{ho}}$ (units of a_{ho}^{-2} and a_{ho}^{-1} on the x and y axis, respectively).

and treat the terms in the square parenthesis as a perturbation. The unperturbed part admits the factorized eigenstates $\psi_{2n} = \phi_{2n}(R)\chi(r)$ that describe a bound molecule with $\chi(r) = \exp(-r/a)/\sqrt{2\pi a}r$ and center-of-mass in an eigenstate of the harmonic oscillator. Since both the initial state and the Hamiltonian are spherically symmetric, conservation of parity allows only even intermediate states. Within this unperturbed approximation, a_{eff} diverges each time the energy of the oscillating molecule corresponds to the ground state energy of the pair of atoms, i.e. at the values of $a = a_{\text{res}}$ that satisfy

$$\left(2n + \frac{3}{2}\right)\hbar\omega\sqrt{\frac{m_B}{m_A + m_B}} - \frac{\hbar^2}{2\mu a_{\text{res}}^2} = \frac{3}{2}\hbar\omega. \tag{5.45}$$

As can be seen in the upper part of Fig. 5.14, this formula describes the position of the resonances with $a > 0$ in a wide region of the graph, since corrections to it are only $O(a/a_{\text{ho}})^2$. In fact, to first order in the perturbation series the term r^2 gives a shift equal to

$$\delta E^{(1)} = \frac{1}{16}\hbar\omega\left(a/a_{\text{ho}}\right)^2, \tag{5.46}$$

while the term $\mathbf{R} \cdot \mathbf{r}$ gives zero to first order, and a complex shift proportional to $(1 + i/2)\hbar\omega\left(a/a_{\text{ho}}\right)^2$ to second order.

5.3.1.2 Unitarity limit

In the unitarity limit $1/a = 0$, the presence of at least one resonance can be demonstrated by a variational argument. As discussed in Chap. 2, a contact potential characterized by scattering length a can be replaced by the simple

boundary condition $\psi(\mathbf{R}, \mathbf{r}) \stackrel{r \to 0}{=} C(\mathbf{R}) \left(r^{-1} - a^{-1} \right) + O(1)$, where C is an arbitrary function of the center of mass coordinate $\mathbf{R}$. The s-wave Ansatz

$$\psi(R, r) = \mathcal{N} \exp\left(-R^2/\lambda^2\right) \frac{\exp\left(-r^2/\sigma^2\right)}{r}, \qquad (5.47)$$

with λ and σ variational parameters, satisfies the boundary conditions imposed by a unitarity limited contact potential, i.e. characterized by $1/a = 0$. Its energy can be calculated from the Hamiltonian (5.44) without the interaction term: the term $\mathbf{R} \cdot \mathbf{r}$ has a vanishing contribution when averaged over this state, and the energy assumes the minimum value

$$E^\infty = \frac{3}{2}\hbar\omega\sqrt{\frac{m_B}{m_A + m_B}} + \frac{1}{2}\hbar\omega\sqrt{\frac{m_B}{4\mu}}. \qquad (5.48)$$

We might imagine continuously tuning a from 0^-, where no bound state can exist, towards $-\infty$. If $E^\infty < 3\hbar\omega/2$ (i.e. if $m_B/m_A < 1.275$) a bound state for $1/a = 0$ is guaranteed by the former Ansatz, and at least one resonance for a_{eff} must exist in the $a < 0$ region.

5.3.1.3   Negative a

When $a < 0$ and $m_B/m_A \ll 1$, the position of the resonances can be found with the aid of a mean-field approximation. We can write an effective Hamiltonian for the particle A supposing that the particle B remains in the ground state of the well for the duration of the scattering event, thereby creating an effective Gaussian attractive well:

$$H_{\text{eff}} = \frac{\hbar^2 k^2}{2m_A} - \frac{2\pi\hbar^2|a|}{m_B}\frac{\exp(-r_A^2/a_{ho}^2)}{\left(\sqrt{\pi}a_{\text{ho}}\right)^3}. \qquad (5.49)$$

As argued above, the characteristic range of the potential is of order a_{ho}. This Hamiltonian can be easily solved, and predicts a divergence of a_{eff} whenever the combination $(|a|/a_{\text{ho}})(m_A/m_B)$ equals the critical value for the appearance of a new bound state (see Fig. 5.14, dashed lines in lower graph). We expect this approximation to work when $k_{\text{rel}}|a| \ll 1$, where $\mathbf{k}_{\text{rel}} \sim \mathbf{k}_B - \mathbf{k}_A m_B/m_A$. B is in the ground state of the harmonic trap, and $k_B \sim a_{\text{ho}}^{-1}$, while A is accelerated by the attractive Gaussian potential and acquires a maximum kinetic energy $\hbar^2 k_A^2/2m_A \sim g/(\sqrt{\pi}a_{\text{ho}})^3$. Therefore, the two conditions $|a|/a_{\text{ho}} \ll 1$ and $(m_B/m_A)(|a|/a_{\text{ho}})^3 \ll 1$ should be simultaneously satisfied.

5.4   Experimental outlook and conclusions

We have presented in this Chapter an appealing setup that makes it possible to obtain a disordered potential and a matter wave satisfying two important conditions for the observation of Anderson localization.

On the one side, correlation lengths for the disorder as short as 0.5μm can be obtained, much shorter than the ones realized presently with speckle potentials. As we have shown, our setup permits to fulfill the Ioffe-Regel criterion
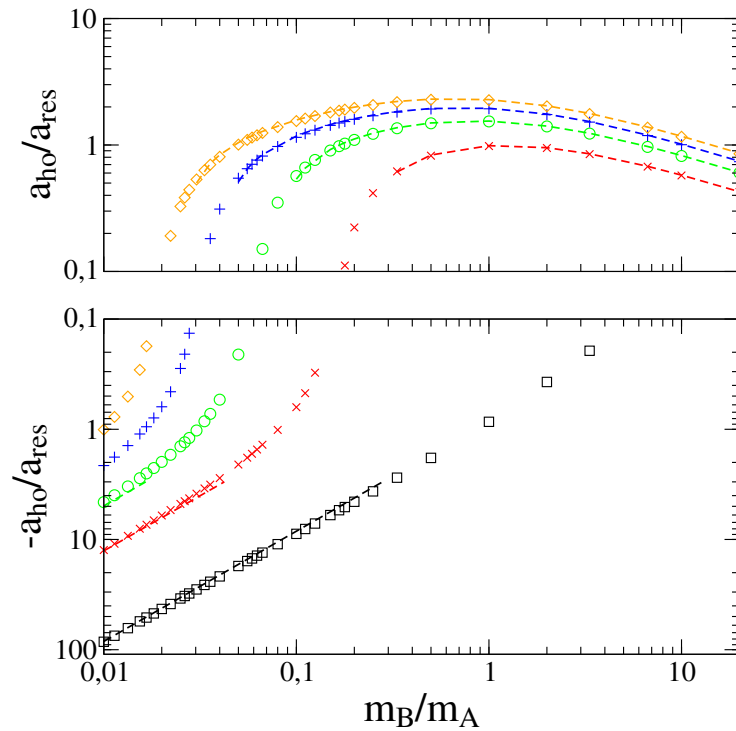
$$\lambda \gtrsim l \qquad (5.50)$$

Figure 5.14: Position of the broadest resonances for positive (upper graph) and negative (lower graph) a as a function of m_B/m_A. The dashed lines are the theoretical predictions, given by Eq. (5.45) for $a > 0$ and by the Hamiltonian in Eq. (5.49) for $a < 0$. In the upper graph, from top to bottom symbols correspond to $n = 4, 3, 2, 1$ in Eq. (5.45).

for a cloud of ^{6}Li atoms already at a temperature of order 200nK, that can routinely be obtained in present experiments. On the other side, the use of polarized fermions for the matter wave would also allow one to completely turn off interactions in the matter wave. As discussed at the beginning of this Chapter, this is important since interactions tend to shield localization effects.

To describe the system, we have modeled the trapped scatterers with a set of contact potentials, and demonstrated that the effective coupling constant shows interesting confinement-induced resonances (CIRs) in a region accessible by present experiments. Exploiting a CIR, experimentalists might obtain a unitarity-limited interaction between the matter wave and the disordered potential. By the exact calculation of the resolvent in coordinate space, we have been able to show directly that our disordered potential, when strongly coupled to the matter wave, supports at low energy a *massive* number of localized states, i.e. eigenstates with exponentially decaying envelope.

We discuss now possible strategies for the practical implementation of our setup. The onset of Anderson localization may be observed in a typical expansion experiment, mapping the cloud size as a function of the amount of disorder. Here below a possible experimental sequence is presented:

1. cool a mixture $A - B$ in a usual harmonic trap.

2. raise the optical lattice to the desired intensity, and ensure that each scatterer B is in the vibrational ground state of its micro-well.

3. let the system equilibrate.

4. switch off the harmonic confinement (but *not* the optical lattice) so that the matter wave will expand freely in the presence of the disordered potential.

5. since we are interested in studying the dynamics of the matter wave in presence of a *static* potential, we want to get rid of the $A - B$ relative acceleration imposed by gravity. This can be achieved in different ways:

   - set the *experimental* reference frame (i.e. the disordered potential) in free fall, by applying an appropriate time-dependent frequency shift to some of the lasers building the optical lattice (the two in the vertical direction). In a similar setup, a 50cm long vacuum chamber would allow up to 300ms of observation.

   - set the whole *laboratory* frame in free fall, by performing the experiment in a micro-gravity environment, e.g. at ZARM[5], on airplanes performing parabolic flights[6], or on an orbiting space station[7].

   - compensate gravity by using magnetic levitation of the matter wave (though, this technique generates an expulsive potential in the horizontal plane, which should be taken accordingly into account in the calculation).

---

[5]ZARM is a 120 meters high drop-tower facility in Bremen, Germany, that provides 4.5s of micro-gravity. An experiment with BECs will be realized there in the close future [82].

[6]Experiments with atomic clocks on parabolic flights have been reported in [83]. Parabolic flights provide up to 20s of micro-gravity.

[7]Experiments with BECs on the International Space Station have been planned by the European Space Agency.

6. let the system evolve: the extended states will escape from the disordered potential, while the localized ones will stay trapped inside.

7. measure the size of the cloud after expansion as a function of the expansion time, the size of the trapping potential (N), the amount of disorder (p) and/or the coupling strength (a_{eff}).

As a_{eff} increases from 0 to a sufficiently high value ($a_{\text{eff}} \sim d$), we have shown that the spectrum of the Hamiltonian contains more and more localized eigenstates, and we expect consequently that the expansion of the cloud will be more and more inhibited.

Doubts might arise about the quantum or classical origin of the reduced expansion. As we will show now, classical trapping is completely ruled out in the proposed scheme, and the reduced expansion could only be attributed to quantum interference, i.e. to Anderson localization.

- The low-energy scattering condition, Eq. (5.4), forbids by energy conservation the formation of a $A - B$ stationary bound states.

- Two identical fermions of mass m_A in the same quantum state, interacting with another particle of mass m_B might undergo the formation of Efimov bound states if $m_A/m_B > 13.6$, implying a possible loss mechanism [84]. This would be avoided in our proposal, since for the pair ${}^6\text{Li}(A)$-${}^{87}\text{Rb}(B)$ one has $m_A/m_B \approx 0.07$.

- Three-body collisions might actually lead to the formation of a bound state, since when $a_{\text{eff}} > 0$ the effective interaction admits a bound state. Those encounters are anyway strongly suppressed by the Pauli principle, since they would forcefully imply the presence of two identical fermions of type A in a very limited region of space.

- If necessary, three-body recombination could be avoided by employing a low density for the matter wave.

- The condition $V_0^A/E_r^A \ll 1$, Eq. (5.8), ensures that the matter wave is sufficiently shielded from interacting with the optical lattice.

For all the reasons explained above, we believe that our proposal offers a viable route to the experimental observation of three-dimensional Anderson localization.

Chapter 6

Conclusions

The main results presented in the thesis are here summarized.

In Chap. 3 we analyzed the properties of charged impurities in a uniform Bose-Einstein condensate, showing that important modifications of its density profile can be induced by a single ion. By a thermodynamic argument we demonstrated that the excess number of atoms ΔN around an ion is proportional, in the limit of low condensate density, to the ratio of the atom-ion and atom-atom scattering lengths [Eq. (3.13)]. For higher densities, we solved the Gross-Pitaevskii equation for the condensate in the presence of different model potentials, which included between others a 3D attractive square well and a long-range potential that closely resembles the ionic one, and evaluated ΔN numerically. For low bulk densities, we found excess numbers of atoms in agreement with our thermodynamic result. With increasing mean-field interactions, we showed that pairs of solutions with equal number of nodes become degenerate and disappear, implying a discontinuous behavior that could be observed in experiments [Fig. 3.5].

Chapter 4 is dedicated to the study of a strongly interacting Fermi gas in its normal phase in the context of transport theory. For a uniform system, we found how the temperature dependence of the viscosity is influenced by interactions, and showed how through the viscosity one may define a viscous relaxation rate $1/\tau$ which gives informations on the typical collision rate inside the gas. We calculated $1/\tau$ for a trapped gas as a function of both temperature and interactions, and showed that classical hydrodynamics should not be applied to describe the transverse oscillations measured in the experiments performed by the groups at Duke and Innsbruck Universities [Fig. 4.3]. By a variational solution of a Boltzmann equation containing interaction effects in both the streaming terms and the collision integral, we extracted the frequency and the damping of the axial and radial collective modes of interest in current experiments as a function of temperature and interaction strength [Figs. 4.6-4.9]. We pointed out that at sufficiently high temperature ($T \gtrsim T_F$) the frequencies of both collective modes should approach the value given by collisionless theory.

In Chap. 5 we addressed the possibility of observing Anderson localization in three dimensions using ultracold gases. A disordered potential can be realized by trapping atoms in the sites of a deep optical lattice with a small filling factor. The dynamics of atoms of a different species which interact with the trapped particles but not with the optical lattice could then be exploited to show the

presence of quantum localization. This scheme completely rules out the possibility of classical trapping, and may be realized experimentally in a mixture of ^{87}Rb and spin-polarized ^{6}Li with a strong optical lattice tuned just to the blue of the strongest rubidium transition. We have shown that the interaction of the matter wave with a trapped scatterer can be successfully modeled by a contact potential. Through the exact solution of our model Hamiltonian (describing a non-interacting matter wave in the presence of a randomly-distributed ensemble of point-like scatterers of strength g_{eff}), we have been able to show by direct imaging that at sufficiently low-energies and strong-couplings our model Hamiltonian supports a large number of exponentially decaying eigenstates, i.e. localized states [Figs. 5.5 and 5.6]. To conclude, we solved the two-body problem of a matter wave colliding with a trapped scatterer and calculated the effective coupling constant g_{eff} [Figs. 5.10-5.12]. The trapping strongly modifies the free-space scattering properties, and we have found for g_{eff} an interesting infinite set of confinement-induced resonances, that may be exploited in the experiments to obtain the large coupling strength necessary for Anderson localization.

Appendix A

Interacting gas in a 1D square well

It is instructive to examine a one-dimensional model which can be solved analytically in terms of Jacobi elliptic functions. We consider a square well potential,

$$
V(x) = \begin{cases} +\infty & x < 0 \\ -\frac{\hbar^2 k_0^2}{2m} & 0 \leq x \leq L \\ 0 & x > L, \end{cases} \tag{A.1}
$$

and investigate its (real) stationary solution, that represent either continuum or bound states.

A.1 Continuum solutions

We look first for continuum solutions whose density per unit length approaches the constant value $n_0 = \mu/U_0$ outside the well:

$$
\left[-\frac{\hbar^2 \nabla^2}{2m} + V + U_0 \psi^2 \right] \psi = \mu \psi. \tag{A.2}
$$

We write their chemical potential, which is positive, in terms of a wavenumber k according to

$$
\mu = \frac{\hbar^2 k^2}{2m}, \tag{A.3}
$$

and similarly the 1D interaction term as $U_0 = \hbar^2 u / 2m$.

Outside the well $(x > L)$ the GP equation reads

$$
-\psi'' + u\psi^3 = k^2 \psi. \tag{A.4}
$$

Multiplying by ψ' and integrating we find

$$
\psi' = \pm \sqrt{t - k^2 \psi^2 + \frac{u \psi^4}{2}} \tag{A.5}
$$

where the integration constant $t = k^2 n_0 - u n_0^2 / 2$ is chosen to satisfy the boundary conditions $\psi^2(\infty) = n_0$ and $\psi'(\infty) = 0$. Outside the well we have 4 possible

solutions,

$$\psi_{out} = \left\{ \begin{array}{l} \pm\sqrt{n_0}\tanh\left[k(x-x_0)/\sqrt{2}\right] \\ \pm\sqrt{n_0}\coth\left[k(x-x_0)/\sqrt{2}\right] \end{array} \right. \qquad \text{(A.6)}$$

the offset x_0 being a free parameter.

Inside the well a similar treatment gives

$$\psi' = \pm\sqrt{q - \kappa^2\psi^2 + \frac{u\psi^4}{2}}$$

where $\kappa^2 = k_0^2 + k^2$ and $q = k^4/2u + k_0^2\psi(L)^2$ is fixed by the conditions of continuity of the wave function and its derivative at the boundary $x = L$. Inside the well the solution is then written in terms of a Jacobi elliptic function [85]:

$$\psi_{in} = r \cdot \text{sn}(\gamma x | m), \qquad \text{(A.7)}$$

where

$$r_\pm^2 = \frac{\kappa^2 \pm \sqrt{\kappa^4 - 2uq}}{u}, \quad m_\pm = \frac{ur_\pm^4}{2q}, \quad \text{and} \quad \gamma = \sqrt{\frac{q}{r_\pm^2}}. \qquad \text{(A.8)}$$

Since $m_+ \cdot m_- = 1$, the identity

$$\text{sn}(x, \ m) = \frac{1}{\sqrt{m}}\text{sn}(\sqrt{m} \cdot x, \ \frac{1}{m}) \qquad \text{(A.9)}$$

can be used to demonstrate the equivalence of the two solutions (generated by r_+ and r_-): we will limit ourself to consider the (-) one, for which $0 \le m < 1$. The m parameter continuously deforms the Jacobi sn function from a sine ($m = 0$) to a hyperbolic tangent ($m \to 1^-$). The period of the $\text{sn}(\gamma x | m)$ function is given by $4K[m]/\gamma$, where $K[m]$ is the complete elliptic integral of the first kind [85]: $K[m]$ is also called quarter period and assumes the limiting values $K[0] = \pi/2$ and $K[m \to 1^-] = \infty$. For a given value of n_0, the solutions can be found by solving the equation $\psi_{in}(L) = \psi_{out}(L)$ for the free parameter x_0, subject to the condition

$$\psi^2(L) = \left\{ \begin{array}{l} n_0\coth^2\left[k(L-x_0)/\sqrt{2}\right] \\ n_0\tanh^2\left[k(L-x_0)/\sqrt{2}\right] \end{array} \right\} \le \psi_{TF}^2 \equiv n_0(1 + \frac{k_0^2}{2un_0}), \qquad \text{(A.10)}$$

which ensures that the coefficients r, γ and m will be real (the condition is automatically satisfied for the tanh solutions).

Since the GP equation is a nonlinear differential equation, we expect to find many different solutions for the same boundary conditions (i.e. the same bulk density n_0). The existence and the number of nodes of the various solutions are connected to the value of the parameter $\rho \equiv L\gamma/K[m]$, whose integer part gives the total number of quarter periods of ψ_{in}, the wave function inside the well. In general, for a solution with z nodes, ρ is constrained by the condition $2z - 1 < \rho < 2z+2$ [see Fig. (A.1)]. For $2z-1 \le \rho < 2z+1$, the solution has a tanh shape outside the well, and x_0 decreases as ρ approaches $2z+1$. When $\rho = 2z+1$, the solution has vanishing derivative at the boundary and connects to the constant $\psi_{out} = \pm\sqrt{n_0}$ outside; when $2z + 1 < \rho < 2z + 2$, the solution assumes a coth shape outside the well. As can be seen in Fig. (A.2), $\partial\rho/\partial n_0$ is always positive: therefore a solution with z nodes exists only for densities $n_0 > n_{crit}^{(z)}$, where $n_{crit}^{(z)}$ is the solution of the equation $\rho(n_{crit}^{(z)}) = 2z - 1$. Fig. (A.2b) shows that this
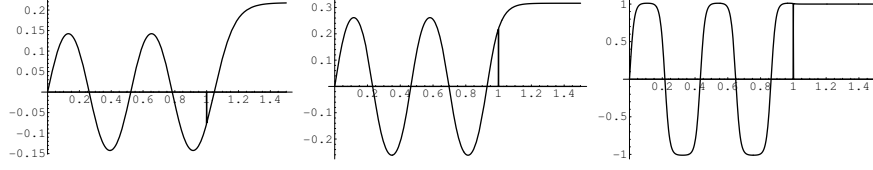
Figure A.1: Amplitude of wave functions with $z = 4$ nodes (x-axis is in units of the well width). The 2 images on the left (a,b) show tanh solutions ($7 < \rho < 9$), the one on the right (c) contains a coth solution ($9 < \rho < 10$). The plots in Figs. (A.1-A.3) are obtained for $k_0 \cdot L = 8$ and $u \sim 2500$.
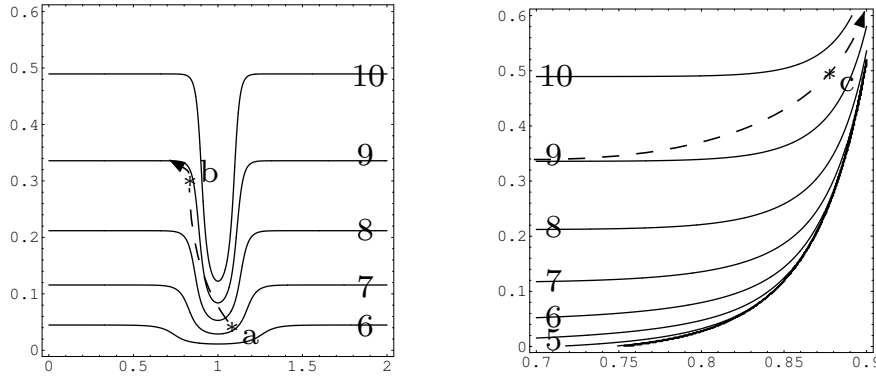

Figure A.2: Contour plots of ρ as a function of x_0/L (x-axis) and $n_0 L$ (y-axis) in the case of tanh-like (left) and coth-like (right) solutions. The isolines show $\rho = 10, 9, 8, ...$ (from top to bottom). The dashed arrows evidence the path followed by the solutions with 4 nodes, and the stars mark the points corresponding to the states shown in Figs. (A.1a,b,c). For these parameters, $n_{\rm crit}^{(4)} L \approx 0.05$. The condition stated in Eq. (A.10) is violated in the region filling the lower-right corner of the right graph.

solution can be followed up to unlimited bulk densities: ρ increases continuously from 0, on the right side of the plot, to a finite and positive asymptotic value on the left side of the plot; its integer part must assume all values between these two limits and therefore no state can disappear.

In Fig. (A.3) we plot the excess number of atoms trapped by the 1D square well as a function of the bulk density.

A.2   Bound levels

We look now for bound solutions, characterized by a negative chemical potential

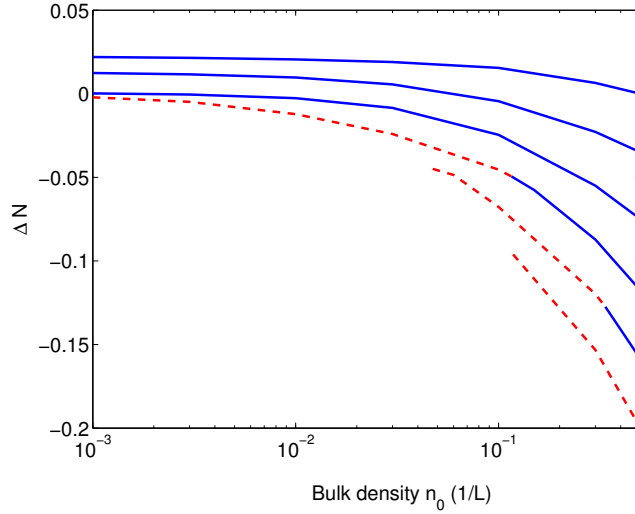$$\mu = -\frac{\hbar^2 k^2}{2m}.$$

(A.11)

Figure A.3: Excess number of atoms as a function of the bulk density. Shown in the picture are the results given by states with a number of nodes z between 0 and 5 (from top to bottom). The continuous lines are coth-like states, while the dashed lines are tanh-like states.

We normalize the (real) condensate wave function $\psi(x)$ to unity,

$$\int_0^\infty \mathrm{d}x\, \psi^2(x) = 1, \qquad (A.12)$$

which implies that the coefficient of the nonlinear term in the GP equation will be proportional to the number of atoms, $u = 8\pi Na$ (N is the number of atoms per unit area and a is the scattering length).

In the region $x > L$, the GP equation reads as in Eq. (A.4), and the boundary condition of vanishing ψ at infinity gives $t = 0$ in Eq. (A.5). The solution outside the well is

$$\psi(x) = \frac{k\sqrt{2/u}}{\sinh[k(x - L) + \phi]}, \qquad (A.13)$$

where ϕ is a proper integration constant. In the region $x < L$ the solution is given by (A.7) and (A.8), with $\kappa^2 = k_0^2 - k^2$ and $q = k_0^2 \psi(L)^2$. The chemical potential associated with a given number of particles can now be determined through the normalization of the wave function. We are interested in determining the maximum number of particles that can be trapped by the potential and therefore let $k \to 0$ (i.e. $\kappa^2 \sim k_0^2$) in the expressions (A.8) . When the potential is sufficiently deep that $k_0 L \gg 1$ the interior wave function is nearly flat everywhere, corresponding to the limit $m \to 1$. The sn-function is then proportional to a hyperbolic tangent over most of the interior region. In the Thomas-Fermi approximation, it can be seen that the condition $u < k_0^2 L$ must be fulfilled. The next term in the expression can be found as follows.

Since we want to match the solution inside the well with the one outside, r^2 must be real; in the opposite case γ becomes imaginary, the solution acquires a
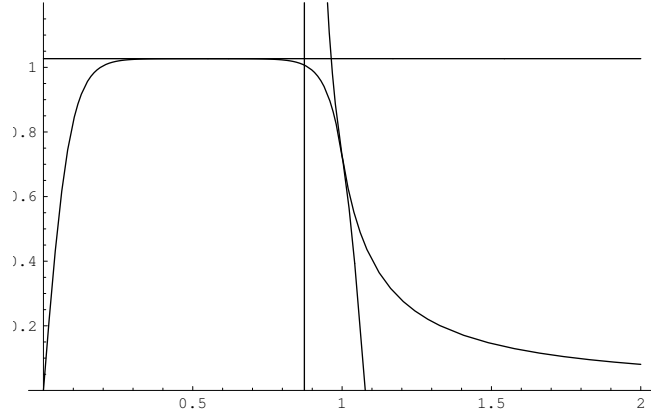
Figure A.4: Plot of the limiting tanh functions.

positive derivative at the boundary and connects to an asymptotically divergent solution outside. Imposing the condition $k \to 0$, we obtain

$$\sqrt{u} \cdot \psi(L) \sim \frac{k_0}{\sqrt{2}}, \qquad (A.14)$$

that leads to $r = k_0/\sqrt{u}$, $m = 1$, $\gamma = k_0/\sqrt{2}$ and therefore

$$\psi_I(x) = \frac{k_0}{\sqrt{u}} \cdot \tanh\left(\frac{k_0}{\sqrt{2}}x\right). \qquad (A.15)$$

This wave function is clearly a limiting one, since the hyperbolic tangent never shows a decreasing derivative, necessary to match with the solution outside the well. In the limit of very deep well, we know the density will be relatively flat inside the well and symmetric with respect to the point $x = K(m)/\gamma$ (where $K(m)$ is the complete elliptic integral of the first kind), located somewhere in the middle of the well; a reasonable trial wave function inside the well can therefore be constructed as:

$$\begin{array}{llll}
\psi_1(x) = & r \cdot \tanh\left(\gamma x\right) & 0 \le x < \frac{L}{2} \\
\psi_2(x) = & r \cdot \tanh\left(\beta - \gamma x\right) & \frac{L}{2} \le x < L
\end{array} \qquad (A.16)$$

where $\beta \equiv \tanh^{-1}\left(1/\sqrt{2}\right) + \gamma L$, so that $\psi_2(x = L) = \psi(L)$. In Fig. (A.4) we show a sketch of the above function.

The logarithmic derivative at the boundary is $\psi_2'(L)/\psi_2(L) = -k_0/2$ and the condition for the continuity of derivatives at the boundary therefore coincides with the condition of vanishing discriminant, Eq. (A.14). The norm of the wave function is calculated as follows:

$$\rho_1^2 = L\frac{r^2}{2} - \frac{r^2}{\gamma}\tanh(\gamma L/2) \qquad (A.17)$$

$$\rho_2^2 = L\frac{r^2}{2} + \frac{r^2}{\sqrt{2}\cdot\gamma} - \frac{r^2}{\gamma}\tanh\left[\tanh^{-1}(\frac{1}{\sqrt{2}}) + \frac{\gamma L}{2}\right] \qquad (A.18)$$

$$\rho_3^2 = \sqrt{\frac{2}{u}}\psi(L) = \frac{k_0}{u} \qquad\qquad (A.19)$$

To leading order in $1/k_0 L$ the normalization condition becomes

$$1 = L\frac{k_0^2}{u_{max}} - 2\frac{k_0}{u_{max}}(\sqrt{2}-1). \qquad\qquad (A.20)$$

Evidently, the number of trapped atoms in a single level of the potential (which enters the parameter u_{max}) is restricted since to the given order one has

$$n_{max} = \frac{N_{max}}{L} = \frac{1}{4\pi a_{aa}}\left[\frac{k_0^2}{2} - \frac{k_0}{L}(\sqrt{2}-1)\right]. \qquad\qquad (A.21)$$

The first term, which is the dominant one in the limit considered, is seen to be identical with the result obtained using the Thomas-Fermi approximation, while the second term represents smaller corrections, originating both in the interior and the exterior region.

A.3   Discussion

In Fig. (A.3) we show that the excess number of particles caused by the 1D square well decreases as we increase the bulk density, and is higher for states with smaller number of nodes. The same features are shown by both the 3D square well and the ionic potential analyzed in Secs. 3.3 and 3.4.

The 1D model fails in predicting many of the characteristic features of the polarization potential in 3D. As we have seen in Sec. A.1, states with a definite number of nodes exist in 1D in a range of bulk densities bounded from below and not from above, with the consequence that no state would disappear with increasing density (and that states with unlimited number of nodes are allowed in the high density limit).

The square well in 3D instead gives a complete qualitative description of the full ionic model. In particular, it correctly predicts that pairs of states merge and disappear for increasing density. In addition, the excess number of atoms for the state with highest number of nodes follows the dilute limit prediction, Eq. (3.13).

Appendix B

Moments of the Boltzmann equation

In this Appendix we provide details of the calculation of the matrix, from which the frequencies and damping rates can be extracted.

First we state some useful identities involving the momentum variables p_i and the rescaled position variables $\tilde{r}_i = m\omega_i r_i$ $(i = x, y, z)$:

$$\langle p_x^2 p_x^2 \rangle = 3\langle p_x^2 p_y^2 \rangle, \tag{B.1}$$

together with

$$\langle p_x^2 p_y^2 \rangle = \frac{1}{3} m^2 kT E_{\text{kin}} \tag{B.2}$$

and

$$\langle \tilde{x}^2 p_x^2 \rangle = \frac{1}{3} m^2 kT E_{\text{pot}}. \tag{B.3}$$

From these it follows that

$$\frac{\langle \tilde{x}^2 p_x^2 \rangle}{\langle p_x^2 p_y^2 \rangle} = \frac{E_{\text{pot}}}{E_{\text{kin}}} = \frac{E_{\text{pot}}}{E_{\text{pot}} - 3E_{\text{int}}/2} = \frac{1}{1 - \xi}. \tag{B.4}$$

Similar identities hold for the other components of $\mathbf{p}$ and $\tilde{\mathbf{r}}$. They are valid both in the presence and absence of the mean field in the equilibrium Fermi function f^0.

The following identity holds when the mean field is neglected in the equilibrium Fermi function:

$$mg\langle \tilde{x}^2 n^0 \rangle = mg \int \frac{d^3p}{(2\pi\hbar)^3} \int d^3r \ \tilde{x} n^0 \left(-mkT \frac{\partial f^0}{\partial \tilde{x}} \right)$$

$$= m^2 kT g \int d^3r \left[(n^0)^2 + \tilde{x}\frac{\partial n^0}{\partial \tilde{x}} n^0 \right] = \frac{m^2}{2} kT E_{\text{int}}. \tag{B.5}$$

This implies that

$$\frac{mg\langle \tilde{x}^2 n^0 \rangle}{\langle \tilde{x}^2 p_x^2 \rangle} \simeq \xi. \tag{B.6}$$

In order to obtain the matrix determining the collective modes we insert (4.66) into (4.64) and take moments of (4.64) with $\tilde{x}^2$, resulting in

$$-i\omega[(3a_1+a_2+a_3)\langle\tilde{x}^2\tilde{y}^2\rangle+(c_1+c_2+c_3)\langle\tilde{x}^2p_x^2\rangle]+\omega_x b_1 A_1+\omega_y b_2 A_2+\omega_z b_3 A_3 = 0.$$
(B.7)

Multiplying the equilibrium equation (4.57) by the combination $\tilde{x}^2 y p_y$ and integrating over all phase space, we obtain the equality

$$\langle\tilde{x}^2p_y^2\rangle - \langle\tilde{x}^2\tilde{y}^2\rangle - mg\langle\tilde{x}^2\tilde{y}\frac{\partial n^0}{\partial\tilde{y}}\rangle = 0.$$
(B.8)

Using the identities given above and Eq. (B.8), we find

$$A_1 = \langle\tilde{x}^2p_x^2\rangle - \langle\tilde{x}^2\tilde{x}^2\rangle - mg\langle\tilde{x}^3\frac{\partial n^0}{\partial\tilde{x}}\rangle =$$

$$= <\tilde{x}^2p_x^2> -3<\tilde{x}^2\tilde{y}^2> -3mg<\tilde{y}^2\tilde{x}\frac{\partial n_0}{\partial\tilde{x}}> = -2<\tilde{x}^2p_x^2>.$$
(B.9)

$$A_2 = \langle\tilde{x}^2p_x^2\rangle - \langle\tilde{x}^2\tilde{y}^2\rangle - mg\langle\tilde{x}^2\tilde{y}\frac{\partial n^0}{\partial\tilde{y}}\rangle = 0.$$
(B.10)

The constant A_3 also vanishes for the same reason as A_2. Collisions do not appear in (B.7) since the $\tilde{r}_i^2$ and $\tilde{r}_i p_i$ are collision invariants, i.e. $I[\tilde{r}_i^2] = I[\tilde{r}_i p_i] = 0$. We now divide Eq. (B.7) by $\langle\tilde{x}^2p_x^2\rangle$. The ratio $\langle\tilde{x}^2\tilde{y}^2\rangle/\langle\tilde{x}^2p_x^2\rangle$ has a very weak dependence on temperature[1] and we have checked that it introduces frequency shifts of only second order in ξ in all the modes. To our level of approximation, we can use here $\langle\tilde{x}^2\tilde{y}^2\rangle/\langle\tilde{x}^2p_x^2\rangle \simeq 1$. This yields

$$-i\omega[3a_1 + a_2 + a_3 + c_1 + c_2 + c_3] - 2\omega_x b_1 = 0,$$
(B.11)

that constitutes the first line of our system of coupled equations.

Next we take moments with $\tilde{x}p_x$ and obtain

$$-i\omega b_1\langle\tilde{x}^2p_x^2\rangle + \omega_x[2\langle\tilde{x}^2p_x^2\rangle(a_1 - c_1) + c_1 m^2 kTE_{\text{int}} + B] = 0,$$
(B.12)

where B is given by

$$B = -mg\left\langle\frac{\delta n}{f^0(1-f^0)}\left(f^0 + \tilde{x}\frac{\partial f^0}{\partial\tilde{x}}\right)\right\rangle =$$

$$= -mg\langle\tilde{x}^2 n^0\rangle \sum_{i=x,y,z} a_i - \frac{m^2}{2}kTE_{\text{int}}\sum_{i=x,y,z} c_i.$$
(B.13)

Dividing Eq. (B.12) by $\langle\tilde{x}^2p_x^2\rangle$, we obtain the second line of our linear system,

$$-i\omega b_1 + \omega_x[(2-\xi)(a_1 - c_1) - \xi(a_2 + c_2 + a_3 + c_3)] = 0.$$
(B.14)

_____

[1]Using the non-interacting Fermi distribution to evaluate (B.8), it is easy to show that

$$\frac{\langle\tilde{x}^2\tilde{y}^2\rangle}{\langle\tilde{x}^2p_x^2\rangle} = 1 - \frac{mg\langle\tilde{x}^2\tilde{y}\partial n^0/\partial\tilde{y}\rangle}{\langle\tilde{x}^2p_x^2\rangle} = \begin{cases} 1+3\xi/4 & \text{for } T \ll T_F \\ 1+\xi/2 & \text{for } T \gg T_F. \end{cases}$$

The difference between the two results is small since in our first order treatment we allow only for interaction parameters $\xi \lesssim 0.5$.

Finally, we take moments with p_x^2 and divide by $\langle p_x^2 p_y^2 \rangle$. Neglecting collisions, a procedure similar to the one that led us to (B.11) yields

$$-i\omega \left[\frac{1}{1-\xi}(a_1 + a_2 + a_3) + 3c_1 + c_2 + c_3 \right] + 2\omega_x b_1 = 0. \qquad \text{(B.15)}$$

Unlike $\tilde{r}_i^2$, $\tilde{r}_i p_i$ and p^2, the quantities p_i^2 are not separately collision invariants and the collisional terms, involving quantities like $\langle p_x^2 I[p_y^2] \rangle$, do not vanish here. We note that

$$\langle p_x^2 I[p_y^2] \rangle = \frac{1}{2} \left\langle \left(p_x^2 + p_z^2 \right) I[p_y^2] \right\rangle = -\frac{1}{2} \left\langle p_x^2 I[p_x^2] \right\rangle, \qquad \text{(B.16)}$$

$$\langle p_x^2 I[p_x^2] \rangle = \left\langle \left(p_x^2 - \frac{p^2}{3} \right) I \left[p_x^2 - \frac{p^2}{3} \right] \right\rangle \qquad \text{(B.17)}$$

($\langle p^2 I[\ldots] \rangle = 0$ due to spherical symmetry) and

$$\langle p_x^2 p_y^2 \rangle = \frac{3}{4} \left\langle \left(p_x^2 - \frac{p^2}{3} \right)^2 \right\rangle. \qquad \text{(B.18)}$$

Using the angular symmetry between the $l = 2$ polynomials $p_x p_y$ and $p_x^2 - p^2/3$, Eq. (4.44), we find

$$\frac{\langle p_x^2 I[p_y^2] \rangle}{\langle p_x^2 p_y^2 \rangle} = -\frac{2}{3} \frac{\left\langle (p_x^2 - p^2/3) I \left[p_x^2 - p^2/3 \right] \right\rangle}{\left\langle (p_x^2 - p^2/3)^2 \right\rangle} = -\frac{2}{3} \frac{\langle (p_x p_y) I[p_x p_y] \rangle}{\left\langle (p_x p_y)^2 \right\rangle} = -\frac{2}{3\tau},$$
$$\text{(B.19)}$$

where the average viscous relaxation rate $1/\tau$ has been defined in (4.52). Inserting the collisional terms in (B.15), we arrive at

$$-i\omega \left[\frac{1}{1-\xi}(a_1 + a_2 + a_3) + \left(3 + \frac{4i}{3\omega\tau} \right) c_1 + \left(1 - \frac{2i}{3\omega\tau} \right)(c_2 + c_3) \right] + 2\omega_x b_1 = 0$$
$$\text{(B.20)}$$

that constitutes the third line of our system of coupled equations. The other six equations may be obtained from (B.11), (B.14) and (B.20) by simple permutation of the indices, and the coefficients of $a_x, a_y, \ldots, c_z$ build up the following matrix:

$$
\begin{bmatrix}
3i\omega & 2\omega_x & i\omega & i\omega & 0 & i\omega & i\omega & 0 & i\omega \\
(\xi - 2)\,\omega_x & i\omega & (2-\xi)\,\omega_x & \xi\omega_x & 0 & \xi\omega_x & \xi\omega_x & 0 & \xi\omega_x \\
\frac{i\omega}{1-\xi} & -2\omega_x & 3i\omega - \frac{4}{3\tau} & \frac{i\omega}{1-\xi} & 0 & i\omega + \frac{2}{3\tau} & \frac{i\omega}{1-\xi} & 0 & i\omega + \frac{2}{3\tau} \\
i\omega & 0 & i\omega & 3i\omega & 2\omega_y & i\omega & i\omega & 0 & i\omega \\
\xi\omega_y & 0 & \xi\omega_y & (\xi - 2)\,\omega_y & i\omega & (2-\xi)\,\omega_y & \xi\omega_y & 0 & \xi\omega_y \\
\frac{i\omega}{1-\xi} & 0 & i\omega + \frac{2}{3\tau} & \frac{i\omega}{1-\xi} & -2\omega_y & 3i\omega - \frac{4}{3\tau} & \frac{i\omega}{1-\xi} & 0 & i\omega + \frac{2}{3\tau} \\
i\omega & 0 & i\omega & i\omega & 0 & i\omega & 3i\omega & 2\omega_z & i\omega \\
\xi\omega_z & 0 & \xi\omega_z & \xi\omega_z & 0 & \xi\omega_z & (\xi - 2)\,\omega_z & i\omega & (2-\xi)\,\omega_z \\
\frac{i\omega}{1-\xi} & 0 & i\omega + \frac{2}{3\tau} & \frac{i\omega}{1-\xi} & 0 & i\omega + \frac{2}{3\tau} & \frac{i\omega}{1-\xi} & -2\omega_z & 3i\omega - \frac{4}{3\tau}
\end{bmatrix}
$$

Appendix C

Green's function for a particle in a box

We wish to calculate the Green's function for a free particle of energy $E = \hbar^2 k^2/2\mu$, imposing periodic boundary conditions in a box of side L. The Green's function $g_0(\mathbf{r})$ satisfies the equation

$$\frac{\hbar^2}{2\mu} \left(\nabla^2 + k^2 \right) g_0^{\text{Box}}(\mathbf{r}) = \delta(\mathbf{r}), \tag{C.1}$$

that can be inverted to obtain

$$g_0^{\text{Box}}(\mathbf{r}) = \frac{2\mu}{\hbar^2 L^3} \sum_{\mathbf{q}} \frac{e^{i\mathbf{q}\cdot\mathbf{r}}}{k^2 - \mathbf{q}^2}. \tag{C.2}$$

The periodic boundary conditions impose $\mathbf{q} = 2\pi\mathbf{n}/L$, with $\mathbf{n} \in \mathbb{Z}^{\mathbf{3}}$ (a triplet of integers). The sum must be evaluated numerically, and the convergence is very slow, since $\sum_{\mathbf{q}} \mathbf{q}^{-2} \sim \int \mathrm{d}q\, O(1)$. To accelerate the calculation, we add and subtract the quantity $X_\lambda = \sum_{\mathbf{q}} \exp(i\mathbf{q}\cdot\mathbf{r})/(\lambda^2 + \mathbf{q}^2)$, where λ is an arbitrary quantity with units of momentum, obtaining

$$g_0^{\text{Box}}(\mathbf{r}) \frac{\hbar^2 L^3}{2\mu} = -X_\lambda + \left(\lambda^2 + k^2 \right) \sum_{\mathbf{q}} \frac{e^{i\mathbf{q}\cdot\mathbf{r}}}{\left(k^2 - \mathbf{q}^2 \right)\left(\lambda^2 + \mathbf{q}^2 \right)}. \tag{C.3}$$

The interest of this procedure lies in the fact that X_λ can be rewritten as a series of exponentially decreasing real terms[1], and the remaining series converges faster than the original form, since $\sum_{\mathbf{q}} \mathbf{q}^{-4} \sim \int \mathrm{d}q\, O\left(q^{-2}\right)$: truncating the complex

---

[1] We use here the Poisson's formula,

$$\sum_{\mathbf{n}} f(\mathbf{n}) = \sum_{\mathbf{n}} \hat{f}(2\pi\mathbf{n})$$

where $\mathbf{n} \in \mathbb{Z}^{\mathbf{3}}$ and $\hat{f}(\mathbf{p}) = \int_{\mathbb{R}^3} \mathrm{d}\mathbf{r}\, e^{-i\mathbf{p}\cdot\mathbf{q}} f(\mathbf{q})$. The Fourier transform of $f(\mathbf{q}) = \exp(i\mathbf{q}\cdot\mathbf{r})/(\mathbf{q}^2 + \lambda^2)$ can be calculated analytically by the methods of residues, and we finally find

$$X_\lambda = \sum_{\mathbf{q}} \frac{e^{i\mathbf{q}\cdot\mathbf{r}}}{\lambda^2 + \mathbf{q}^2} = \frac{L^3}{4\pi} \sum_{\mathbf{n}} \frac{e^{-\lambda\|\mathbf{r}-L\mathbf{n}\|}}{\|\mathbf{r}-L\mathbf{n}\|},$$

$\|\mathbf{v}\|$ being the Cartesian norm of the vector $\mathbf{v}$.

series to $N_{\max}$ terms, the error is $\sim O(N_{\max}^{-1})$. The procedure can be iterated one more time, yielding

$$
g_0^{\text{Box}}(\mathbf{r}) = -\frac{\mu}{2\pi\hbar^2} \sum_{\mathbf{n}} \mathrm{e}^{-\lambda\|\mathbf{r}-L\mathbf{n}\|} \left[\frac{1}{\|\mathbf{r}-L\mathbf{n}\|} + \frac{\lambda^2+k^2}{2\lambda} \right]
$$
$$
+ \frac{2\mu\left(\lambda^2+k^2\right)^2}{\hbar^2 L^3} \sum_{\mathbf{q}} \frac{\mathrm{e}^{i\mathbf{q}\cdot\mathbf{r}}}{\left(k^2-\mathbf{q}^2\right)\left(\lambda^2+\mathbf{q}^2\right)^2}. \quad (\text{C.4})
$$

The error due to the truncation of the last term on the right hand side is in this way reduced to $\sim O(N_{\max}^{-3})$, and the calculation of g_0^{Box} can now be performed very efficiently. When $r \to 0$, the term with $\mathbf{n} = 0$ contains the expected $1/r$ divergence, and the regular part of the Green's function reads

$$
g_{0,\text{reg}}^{\text{Box}}(\mathbf{r}) = -\frac{\mu}{2\pi\hbar^2} \left\{ -\lambda + \frac{\lambda^2+k^2}{2\lambda} + \sum_{\mathbf{n}\in\mathbb{Z}^{3*}} \mathrm{e}^{-\lambda L\|\mathbf{n}\|} \left[\frac{1}{L\|\mathbf{n}\|} + \frac{\lambda^2+k^2}{2\lambda} \right] \right\}
$$
$$
+ \frac{2\mu\left(\lambda^2+k^2\right)^2}{\hbar^2 L^3} \sum_{\mathbf{q}} \frac{1}{\left(k^2-\mathbf{q}^2\right)\left(\lambda^2+\mathbf{q}^2\right)^2}, \quad (\text{C.5})
$$

where $\mathbb{Z}^{3*} = \mathbb{Z}^3 - \{0,0,0\}$. The final result is of course independent of λ.

Appendix D

Integral equation for ψ_{reg}

The Feynman propagator K associated with the non-interacting Hamiltonian H_0 [86],

$$K_t(\mathbf{r}_A, \mathbf{r}_B; \boldsymbol{\rho}_A, \boldsymbol{\rho}_B) = \left\langle \mathbf{r}_A, \mathbf{r}_B \left| e^{-iH_0 t/\hbar} \right| \boldsymbol{\rho}_A, \boldsymbol{\rho}_B \right\rangle \qquad \text{(D.1)}$$

can be factorized as the product of the two factors, $K_t = K_t^A K_t^B$, the first term describing a free particle,

$$K_t^A(\mathbf{r}_A; \boldsymbol{\rho}_A) = e^{-i\pi 3/4} \left(\frac{m_A}{2\pi\hbar t} \right)^{3/2} \exp\left(\frac{im_A}{2\hbar} \frac{|\mathbf{r}_A - \boldsymbol{\rho}_A|^2}{t} \right) \qquad \text{(D.2)}$$

and the second one a particle in a 3D harmonic oscillator,

$$K_t^B(\mathbf{r}_B; \boldsymbol{\rho}_B) = \phi(t) e^{-i\pi 3/4} \left(\frac{m_B \omega}{2\pi\hbar |\sin(\omega t)|} \right)^{3/2} \\ \exp\left(\frac{im_B \omega}{\hbar} \left[\frac{r_B^2 + \rho_B^2}{2\tan(\omega t)} - \frac{\mathbf{r}_B \cdot \boldsymbol{\rho}_B}{\sin(\omega t)} \right] \right) \qquad \text{(D.3)}$$

where $\phi(t) = \exp(i\pi n/2)$ for $n\pi < \omega t < (n+1)\pi$. With the boundary condition $K_t = 0$ for $t < 0$, G_E is obtained as the Fourier transform of K,

$$G_E = -\frac{i}{\hbar} \int_0^\infty dt \, e^{i(E+i0^+)t/\hbar} K_t. \qquad \text{(D.4)}$$

For simplicity, we introduce dimensionless variables by expressing quantities in harmonic oscillator units and, even though the derivation has been carried out for a generic mass ratio, restrict ourselves here to the special case $m_A = m_B = m$.

In order to find the equation satisfied by ψ_{reg}, we rewrite Eq. (5.28) as

$$\psi(\mathbf{r}_A, \mathbf{r}_B) = \psi_0(\mathbf{r}_A, \mathbf{r}_B) + g\psi_{\text{reg}}(R) \int d\boldsymbol{\rho} \, G_E(\mathbf{r}_A, \mathbf{r}_B; \boldsymbol{\rho}, \boldsymbol{\rho}) \\ + g \int d\boldsymbol{\rho} \, G_E(\mathbf{r}_A, \mathbf{r}_B; \boldsymbol{\rho}, \boldsymbol{\rho}) \left[\psi_{\text{reg}}(\rho) - \psi_{\text{reg}}(R) \right] \qquad \text{(D.5)}$$

and let the two particles approach each other. We introduce here the center-of-mass and relative coordinates $\mathbf{R} = (\mathbf{r}_A + \mathbf{r}_B)/2$ and $\mathbf{r} = \mathbf{r}_A - \mathbf{r}_B$. Let us turn

our attention to the first integral appearing in Eq. (D.5):

$$U \equiv \int d\boldsymbol{\rho}\, G_E \left(\mathbf{R} + \frac{\mathbf{r}}{2}, \mathbf{R} - \frac{\mathbf{r}}{2}; \boldsymbol{\rho}, \boldsymbol{\rho} \right). \qquad (D.6)$$

Performing the Gaussian integration over $\boldsymbol{\rho}$ [87] one finds

$$U = \frac{e^{i\pi 3/4}}{(2\pi)^{3/2}} \int_0^\infty dt\, \frac{\tilde{\phi}(t) e^{i(Et+W)}}{|\sin(t) + t\cos(t)|^{3/2}}, \qquad (D.7)$$

where

$$W = \frac{|\mathbf{R} + \frac{\mathbf{r}}{2}|^2}{2t} + \frac{\left|\mathbf{R} - \frac{\mathbf{r}}{2}\right|^2}{2\tan(t)} - \frac{1}{x} \left| \frac{\mathbf{R} + \frac{\mathbf{r}}{2}}{2t} + \frac{\mathbf{R} - \frac{\mathbf{r}}{2}}{2\sin(t)} \right|^2. \qquad (D.8)$$

We have here introduced the shorthand notation $x(t) = [1/t + 1/\tan(t)]/2$ and the phase factor $\tilde{\phi}(t)$, which equals $\exp(i\pi n/2)$ for $t_n < t < t_{n+1}$, where $t_0 = 0$ and $t_1 = 2.029$, $t_2 = 4.913$, $\ldots$ are the consecutive solutions of $x(t) = 0$. The latter expression, Eq. (D.7), diverges as $1/r$ for $r \to 0$ in the neighborhood of $t = 0$:

$$\begin{aligned}
\frac{(2\pi)^{3/2}}{e^{i\pi 3/4}} U &= \int_0^\delta dt\, \frac{e^{ir^2/4t}}{(2t)^{3/2}} + \int_\delta^\infty dt \ldots \\
&= \int_0^\infty dt\, \frac{e^{ir^2/4t}}{(2t)^{3/2}} + \int_\delta^\infty dt \left(-\frac{1}{(2t)^{3/2}} + \ldots \right) \\
&= \frac{1}{r}\sqrt{\frac{\pi}{2}} e^{i\pi/4} + \int_\delta^\infty dt \left(-\frac{1}{(2t)^{3/2}} + \ldots \right). \qquad (D.9)
\end{aligned}$$

We finally find

$$g\psi_{\mathrm{reg}}(R) \int d\boldsymbol{\rho}\, G_E \left(\mathbf{R} + \frac{\mathbf{r}}{2}, \mathbf{R} - \frac{\mathbf{r}}{2}; \boldsymbol{\rho}, \boldsymbol{\rho} \right) \stackrel{r \to 0}{=} \psi_{\mathrm{reg}}(R) \left(gF_1(R) - \frac{a}{r} \right) + O(1) \qquad (D.10)$$

that separates out the expected $1/r$ divergent contribution and defines

$$F_1(R) = \frac{e^{i\pi 3/4}}{(2\pi)^{3/2}} \int_0^\infty \mathrm{d}t \left(\frac{\tilde{\phi}(t) e^{i(Et+W_0)}}{|\sin(t) + t\cos(t)|^{3/2}} - \frac{1}{(2t)^{3/2}} \right) \qquad (D.11)$$

with $W_0 = R^2 \left(\cos(t) - t\sin(t)/2 - 1 \right) / \left(\sin(t) + t\cos(t) \right)$. The term $(2t)^{-3/2}$ regularizes F_1 in the neighborhood of $t = 0$, and we have taken the limit $\delta \to 0$.

Let us now consider the remaining term appearing in Eq. (D.5): when $\mathbf{r} \to 0$ and $\mathbf{u} = \mathbf{R} - \boldsymbol{\rho} \to 0$, the Green's function G_E diverges as $|\mathbf{u}|^{-4}$, or equivalently as $\left(|\mathbf{r}_A - \boldsymbol{\rho}_A|^2 + |\mathbf{r}_B - \boldsymbol{\rho}_B|^2 \right)^{-2}$, but the second integral in Eq. (D.5) is convergent in $\mathbf{u} \sim 0$:

$$\int d\boldsymbol{\rho}\, G_E \left(\mathbf{R} + \frac{\mathbf{r}}{2}, \mathbf{R} - \frac{\mathbf{r}}{2}; \boldsymbol{\rho}, \boldsymbol{\rho} \right) \left[\psi_{\mathrm{reg}}(\boldsymbol{\rho}) - \psi_{\mathrm{reg}}(R) \right]$$

$$\stackrel{\mathbf{r} \to 0,\, \mathbf{u} \to 0}{=} \int \frac{d\mathbf{u}}{|\mathbf{u}|^4} \left[\mathbf{u} \left. \frac{\partial \psi_{reg}}{\partial \mathbf{u}} \right|_{\mathbf{u}=\mathbf{0}} + O\left(|\mathbf{u}|^2 \right) \right] \qquad (D.12)$$

(the first order term vanishes due to spherical symmetry). In this term therefore no divergence arises and we may set $r = 0$. The angular integrations can be performed analytically and we obtain:

$$\int d\boldsymbol{\rho}\, G_E\left(R, R; \boldsymbol{\rho}, \boldsymbol{\rho}\right)\left[\psi_{\mathrm{reg}}(\rho) - \psi_{\mathrm{reg}}(R)\right]$$

$$= \frac{1}{R}\int_0^\infty d\rho \left[\tilde{\psi}_{\mathrm{reg}}(\rho) - \frac{\rho}{R}\tilde{\psi}_{\mathrm{reg}}(R)\right] F_2(R, \rho) \quad \text{(D.13)}$$

with

$$F_2(R, \rho) = \int_0^\infty dt\, \frac{\phi(t)e^{i[Et+(R^2+\rho^2)x]}}{(t|\sin(t)|)^{3/2}}\frac{\sin(2y\rho R)}{(2\pi)^2 y}, \quad \text{(D.14)}$$

which is symmetric under the exchange of ρ and R. We have here introduced the radial wave function $\tilde{\psi}(R) = R\psi(R)$ and the function $y(t) = [1/t + 1/\sin(t)]/2$.

Writing

$$\psi\left(\mathbf{r}_A, \mathbf{r}_B\right) \overset{r\to 0}{=} \psi_{\mathrm{reg}}(R)\left(1 - \frac{a}{r}\right) + O(1), \quad \text{(D.15)}$$

we can cancel the divergent contribution on both sides of Eq. (D.5), and the remaining terms constitute the implicit integral equation

$$\tilde{\psi}_{\mathrm{reg}}(R) = \tilde{\psi}_0(R, R) + gF_1(R)\tilde{\psi}_{\mathrm{reg}}(R) + g\int d\rho\, F_2(R, \rho)\left[\tilde{\psi}_{\mathrm{reg}}(\rho) - \frac{\rho}{R}\tilde{\psi}_{\mathrm{reg}}(R)\right]$$
$$\text{(D.16)}$$

that needs to be solved numerically in order to determine ψ_{reg}. The latter equation can be written in a symbolic, more compact form as

$$\tilde{\psi}_{\mathrm{reg}} = \frac{I}{I - g\hat{O}}\tilde{\psi}_0 \quad \text{(D.17)}$$

where $\hat{O}$ is a symmetric integral operator, which is real in the limit $k \to 0$ [88].

Bibliography

[1] M. H. Anderson, J. R. Ensher, M. R. Matthews, C. E. Wieman, and E. A. Cornell, Science **269**, 198 (1995).

[2] K. B. Davis, M. O. Mewes, M. R. Andrews, N. J. van Druten, D. S. Durfee, D. M. Kurn, and W. Ketterle, Phys. Rev. Lett. **75**, 3969 (1995).

[3] C. C. Bradley, C. A. Sackett, J. J. Tollett, and R. G. Hulet, Phys. Rev. Lett. **75**, 1687 (1995); C. C. Bradley, C. A. Sackett, and R. G. Hulet, Phys. Rev. Lett. **78**, 985 (1997).

[4] C. J. Pethick and H. Smith, *Bose–Einstein Condensation in Dilute Gases* (Cambridge University Press, Cambridge 2002).

[5] L. Pitaevskii and S. Stringari, *Bose–Einstein Condensation* (Clarendon Press, Oxford, 2003).

[6] D. Ciampini, M. Anderlini, J. H. Müller, F. Fuso, O. Morsch, J. W. Thomsen, and E. Arimondo, Phys. Rev. A **66**, 043409 (2002).

[7] E. Arimondo, private communication.

[8] R. Côté, V. Kharchenko, and M. D. Lukin, Phys. Rev. Lett. **89**, 093001 (2002).

[9] P. Massignan, C. J. Pethick, and H. Smith, Phys. Rev. A **71**, 023606 (2005).

[10] M. Greiner, C. A. Regal, and D. S. Jin, Nature **426**, 537 (2003); M. W. Zwierlein *et al.*, Phys. Rev. Lett. **91**, 250401 (2003); S. Jochim *et al.*, Science **302**, 2101 (2003); T. Bourdel *et al.*, Phys. Rev. Lett. **93**, 050401 (2004).

[11] C. A. Regal, M. Greiner, and D. S. Jin, Phys. Rev. Lett. **92**, 040403 (2004); M. W. Zwierlein *et al.*, Phys. Rev. Lett. **92**, 120403 (2004).

[12] C. Chin, M. Bartenstein, A. Altmeyer, S. Riedl, S. Jochim, J. Hecker Denschlag, R. Grimm, Science **305**, 1128 (2004).

[13] M. W. Zwierlein, J. R. Abo-Shaeer, A. Schirotzek, C. H. Schunck, and W. Ketterle, Nature **435**, 1047 (2005).

[14] For an account of the early history of the topic, see M. Randeria in *Bose-Einstein Condensation*, edited by A. Griffin, D. Snoke, and S. Stringari (Cambridge University Press, Cambridge 1995).

[15] M. A. Baranov and D. S. Petrov, Phys. Rev. A **62**, 041601 (2000).

[16] G. M. Bruun and B. R. Mottelson, Phys. Rev. Lett. **87**, 270403 (2001).

[17] G. M. Bruun and C. W. Clark, Phys. Rev. Lett. **83**, 5415 (1999).

[18] J. Kinast, S. L. Hemmer, M. E. Gehm, A. Turlapov, and J. E. Thomas, Phys. Rev. Lett. **92**, 150402 (2004).

[19] M. Bartenstein, A. Altmeyer, S. Riedl, S. Jochim, C. Chin, J. Hecker Denschlag, and R. Grimm, Phys. Rev. Lett. **92**, 203201 (2004).

[20] J. Kinast, A. Turlapov, and J. E. Thomas, Phys. Rev. A **70**, 051401(R) (2004).

[21] J. Kinast, A. Turlapov, and J. E. Thomas, Phys. Rev. Lett. **94**, 170404 (2005).

[22] P. Massignan, G. M. Bruun, and H. Smith, Phys. Rev. A **71**, 033607 (2005).

[23] M. Greiner, O. Mandel, T. Esslinger, T. W. Hänsch, and I. Bloch, Nature **415**, 39 (2002).

[24] G. Montambaux and E. Akkermans, *Physique mésoscopique des électrons et des photons* (EDP Sciences, 2004).

[25] P. A. Lee and T. V. Ramakrishnan, Rev. Mod. Phys. **57**, 287 (1985).

[26] B. Kramer and A. MacKinnon, Rep. Prog. Phys. **56**, 1469 (1993).

[27] P. W. Anderson, Phys. Rev. **109**, 1492 (1958).

[28] D. S. Wiersma, P. Bartolini, A. Lagendijk, and R. Righini, Nature **390**, 671 (1997).

[29] D. Boiron, C. Mennerat-Robilliard, J.-M. Fournier, L. Guidoni, C. Salomon, and G. Grynberg, Eur. Phys. J. D **7**, 373 (1999).

[30] J. E. Lye, L. Fallani, M. Modugno, D. Wiersma, C. Fort, and M. Inguscio, Phys. Rev. Lett. **95**, 070401 (2005).

[31] D. Clément, A. F. Varon, M. Hugbart, J. Retter, P. Bouyer, L. Sanchez-Palencia, D. M. Gangardt, G. V. Shlyapnikov, and A. Aspect, Phys. Rev. Lett. **95**, 170409 (2005).

[32] C. Fort, L. Fallani, V. Guarrera, J. E. Lye, M. Modugno, D. S. Wiersma, and M. Inguscio, Phys. Rev. Lett. **95**, 170410 (2005).

[33] T. Schulte, S. Drenkelforth, J. Kruse, W. Ertmer, J. Arlt, K. Sacha, J. Zakrzewski, and M. Lewenstein, Phys. Rev. Lett. **95**, 170411 (2005).

[34] U. Gavish and Y. Castin, Phys. Rev. Lett. **95**, 020401 (2005).

[35] M. Rusek, A. Orlowski, Phys. Rev. E **51**, R2763 (1995).

[36] Emmanuel Mandonnet, PhD Thesis of Université Paris 6, unpublished (2000).

[37] P. Massignan and Y. Castin, in preparation.

[38] L. D. Landau and E. M. Lifshitz, *Quantum mechanics* (Pergamon, New York, 1977).

[39] L. I. Schiff, *Quantum mechanics. An introduction* (McGraw-Hill, New York, 1968).

[40] R. A. Duine and H. T. C. Stoof, Phys. Rep. **396**, 115 (2004).

[41] V. V. Flambaum, G. F. Gribakin, and C. Harabati, Phys. Rev. A **59**, 1998 (1999).

[42] F. G. Fumi, Philos. Mag. **46**, 1007 (1955); G. D. Mahan, *Many-Particle Physics*, 2nd ed. (Plenum, New York, 1990), p. 253.

[43] R. Roth and H. Feldmeier, Phys. Rev. A **64**, 043603 (2001).

[44] H. Fu, Y. Wang, and B. Gao, Phys. Rev. A **67**, 053612 (2003).

[45] T. F. O'Malley, L. Spruch, and L. Rosenberg, J. of Math. Phys. **2**, 491 (1961).

[46] R. J. Donnelly, *Experimental Superfluidity* (Univ. of Chicago Press, 1967).

[47] J. Bardeen, G. Baym, and D. Pines, Phys. Rev. Lett. **17**, 372 (1966).

[48] J. Bardeen, G. Baym, and D. Pines, Phys. Rev. **156**, 207 (1967).

[49] G. F. Gribakin and V. V. Flambaum, Phys. Rev. A **48**, 546 (1993).

[50] V. Kharchenko and M. D. Lukin, private communication.

[51] R. M. Kalas and D. Blume, cond-mat/0512031.

[52] T. Pfau, private communication.

[53] L. D. Landau and E. M. Lifshitz, *Fluid mechanics* (Pergamon, Oxford, 1959).

[54] F. Dalfovo, S. Giorgini, L. P. Pitaevskii, and S. Stringari, Rev. Mod. Phys. **71**, 463 (1999).

[55] L. Vichi, J. of Low Temp. Phys. **121**, 177 (2000).

[56] P. Pedri, D. Guéry-Odelin, and S. Stringari, Phys. Rev. A **68**, 043608 (2003).

[57] G. M. Kavoulakis, C. J. Pethick, and H. Smith, Phys. Rev. A **57**, 2938 (1997).

[58] G. M. Kavoulakis, C. J. Pethick, and H. Smith, Phys. Rev. Lett. **81**, 4036 (1998).

[59] D. Guéry-Odelin, F. Zambelli, J. Dalibard, and S. Stringari, Phys. Rev. A **60**, 4851 (1999).

[60] U. Al Khawaja, C. J. Pethick, and H. Smith, J. of Low Temp. Phys. **118**, 127 (2000).

[61] G. M. Kavoulakis, C. J. Pethick, and H. Smith, Phys. Rev. A **61**, 053603 (2000).

[62] D. Guéry-Odelin, Phys. Rev. A **66**, 033613 (2002).

[63] H. Smith and H. H. Jensen, *Transport Phenomena* (Oxford University Press, Oxford 1989).

[64] G. M. Bruun and C. J. Pethick, Phys. Rev. Lett. **92**, 140404 (2004).

[65] G. M. Bruun and H. Smith, Phys. Rev. A **72**, 043605 (2005).

[66] B. A. Gelman, E. V. Shuriak, and I. Zahed, Phys. Rev. A **72**, 043601 (2005).

[67] J. E. Thomas, J. Kinast, and A. Turlapov, Phys. Rev. Lett. **95**, 120402 (2005).

[68] J. von Neumann and E. Wigner, Phys. Z. **30**, 465 (1929).

[69] The original von Neumann-Wigner paper [68] contains a superficial algebraic error, that has been corrected in: F. H. Stillinger and D. R. Herrick, Phys. Rev. A **11**, 446 (1975).

[70] K. G. Singh and D. S. Rokhsar, Phys. Rev. B **49**, 9013 (1994); K. O. Rasmussen, D. Cai, A. R. Bishop, and N. Grønbech-Jensen, Europhys. Lett. **47**, 421 (1999); D. K. K. Lee and J. M. F. Gunn, J. Phys. C **2**, 7753 (1990).

[71] S. E. Hamann, D. L. Haycock, G. Klose, P. H. Pax, I. H. Deutsch, and P. S. Jessen, Phys. Rev. Lett. **80**, 4149 (1998).

[72] H. Perrin, A. Kuhn, I. Bouchoule, and C. Salomon, Europhys. Lett. **42**, 395 (1998).

[73] K. Huang and H.-F. Meng, Phys. Rev. Lett. **69**, 644 (1992).

[74] M. Rusek, J. Mostowski, and A. Orlowski, Phys. Rev. A **61**, 022704 (2000).

[75] M. Olshanii, Phys. Rev. Lett. **81**, 938 (1998).

[76] T. Bergeman, M. G. Moore, and M. Olshanii, Phys. Rev. Lett. **91**, 163201 (2003).

[77] V. Peano, M. Thorwart, C. Mora, and R. Egger, New J. Phys. **7**, 192 (2005).

[78] D. S. Petrov, M. Holzmann, and G.V. Shlyapnikov, Phys. Rev. Lett. **84**, 2551 (2000).

[79] P. O. Fedichev, M. J. Bijlsma, and P. Zoller, Phys. Rev. Lett. **92**, 080401 (2004).

[80] H. Moritz, T. Stöferle, K. Günter, M. Köhl, and T. Esslinger, Phys. Rev. Lett. **94**, 210401 (2005).

[81] T. Stöferle, H. Moritz, K. Günter, M. Köhl, and T. Esslinger, cond-mat/0509211.

[82] J. Reichel, private communication.

[83] P. Laurent, P. Lemonde, E. Simon, G. Santarelli, A. Clairon, N. Dimarcq, P. Petit, C. Audoin, and C. Salomon, Eur. Phys. J. D **3**, 201 (1998).

[84] D. S. Petrov, Phys. Rev. A **67**, 010703(R) (2003).

[85] *Handbook of mathematical functions*, edited by M. Abramowitz and I. A. Stegun (Dover Publications inc., New York, 1972).

[86] R. P. Feynman and A. R. Hibbs, *Quantum Mechanics and Path Integrals* (Mc Graw-Hill, 1965), Chap. 4.

[87] $\int_0^\infty d\rho\, \rho^2 \exp\left(ix\rho^2\right) = \sqrt{\pi/16x^3} \exp\left(3i\pi/4\right)$ for $x > 0$. The result for $x < 0$ is the complex conjugate of the latter expression.

[88] If one only aims at calculating strictly zero energy properties (i.e. a_{eff}, and not f_k or r_e), the treatment presented in this Appendix can be drastically simplified setting $\tau = it$ and $E = 0$ in Eqs. (D.2-D.3-D.4): the derivation of $\hat{O}$ proceeds in an analogous way, but the resulting integral equation is much easier to solve since the integrands in both F_1 and F_2 become exponentially damped, real functions.